UNIVERSITY OF CALGARY

Stochastic Actor-Oriented Models of Functional and Structural Human Brain Networks in Aging

by

Emma Garrison

A THESIS
SUBMITTED TO THE FACULTY OF GRADUATE STUDIES
IN PARTIAL FULFILLMENT OF THE REQUIREMENTS FOR THE
DEGREE OF MASTER OF SCIENCE

GRADUATE PROGRAM IN PHYSICS AND ASTRONOMY

CALGARY, ALBERTA
JANUARY, 2026

Abstract

The human brain is a complex and dynamical system that changes throughout the lifetime. Non-invasive imaging techniques, including magnetic resonance imaging (MRI), allow for the measurement of large-scale functional and structural connectivity networks in the brain. Beyond trends, the dynamics across long timescales are still poorly understood. Our research aims to address the question of these long-term dynamics by carefully adapting and applying the stochastic actor-oriented model to brain networks derived from MRI data in an aging population. The resulting models of network change suggest that the brain is promoting modularity, local efficiency, and short-range connectivity during aging with more adaptive functional networks compared to structural networks. Differences between individuals with and without cognitive impairment suggest a disruption in the maintenance of key brain topology in the progression of cognitive impairment with age. These results are modulated by subnetwork and sex differences that contribute further to the emerging picture of long-term dynamics in aging.

Acknowledgements

This thesis is the result of hard fought journey, no small amount of luck, and the support of so many people. I would like to take a couple of moments to thank those who have contributed to the success of this work, though the list will be in no way comprehensive.

I would like to thank my supervisors, Dr. Javier Orlandi and Dr. Roberto Sotero Diaz, for the space to explore this topic and for their guidance throughout. Thank you for demonstrating every day what good mentorship looks like; I know now what I, and all graduate students, deserve.

My colleagues in the Complexity Science Group were teammates, advisors, and inspirations in this work. I am grateful for the routine expansion of my knowledge and curiosity that came from exploring complexity science with you all. Beyond that, I think fondly on the, sometimes grueling, hours we spent improving my research and presentations. I would also like to thank Lazaro Sanchez-Rodriguez and Yasser Iturria-Medina's whole team for providing their implementation of fMRI preprocessing. This was an invaluable help in getting started with those procedures.

This thesis and this degree would not have been possible without the incredible educators who have shaped my academic trajectory in this field - Pam Stryker, Todd White, Dr. Rhea Merck, Dr. Rutvik Desai, and many more. I am the scientist that I am today because of the inspiration that you provided from the earliest days of my education. Thank you for believing in me! I am so proud to show you this work. Special thanks to Mark and Nancy Misage, who inspired me to pursue physics. You were such a highlight of my high school education and I hope you are enjoying your well-deserved retirement. You could say that I am now studying networks of interacting gazelles!

Finally, I would like to thank my friends and family who supported me from all stages of my life. I am so grateful for the visits and calls with my friends who helped me navigate the trials and successes of this journey! To Ciara Chrisholm who always had my back and listened to my rants (even if you did not always know what I was researching), I am so grateful I got to share my office with you! I thank you and your family for making me feel safe and cared for in Calgary. To Anja Rabus, you were my friend when I really needed one and changed the course of this degree for me. I miss you so much and I am thankful to have your

support and friendship from across the world. Thank you for all the discussions, edits, and climbing! To the group that I haphazardly assembled to play board games... You truly turned things around for me. Because of you (and the magpies), I will miss this place. Keep counting cards and killing Lorenzo in my absence!

To my family, who have always been there for me, I am deeply privileged to always have you in my corner. I often mention running ideas and writing by my parents who are always ready for a good scientific discussion. Not many are privileged with such a loving and supportive family. This is for you!

Contents

List of Figures

List of Tables

List of Symbols, Abbreviations, and Nomenclature

Symbol	Defintion
SAOM	Stochastic actor-oriented model
MRI	Magnetic Resonance Imaging
fMRI	Functional Magnetic Resonance Imaging
DTI	Diffusion Tensor Imaging
TE	Time to echo
TR	Time to repeat
$T1$	Recovery of longitudinal magnetization
$T2$	Loss of transverse magnetization
$T2^*$	Loss of transverse magnetization under free induction decay
MCI	Mild Cognitive Impairment
AD	Alzheimer's Disease
ADNI	Alzheimer's Disease Neuroimaging Initiative
λ	The rate function
f	The objective function
ρ	Base rate
θ	The base rate and factor weights vector
GMM	Generalized Method of Moments
N	The number of nodes

Symbol	Defintion
D	Factor Degree
T	Factor Transitive Triads
B	Factor Betweenness
$D2$	Factor Distance 2
$C4$	Factor 4-Cycles
A	Factor Assortativity
PD	Factor Physical Distance
ND	Factor Physical Neighbor Distance
S	Factor Same Subnetwork
ST	Factor Same Subnetwork Transitive Triplet
JT	Factor Jump Subnetwork Transitive Triplet
$S2$	Factor Same Subnetwork Distance 2
$S4$	Factor Same Subnetwork 4-Cycles
PR	Precision
RE	Recall
SP	Specificity
AC	Accuracy
F_β	F-score

Chapter 1

Introduction

1.1 Complex Systems

In observing the world around us, one may notice that many of the systems that shape our world are comprised of complex and dynamic components. Viewing these systems, from the furthest galaxies to the earth to our very own bodies, as complex can provide great insight into their behavior through the interactions and dynamics of their components [Mitchell 2009b, Holovatch 2017, Bar-Yam 2019, Siegenfeld 2020]. These interactions underpin emergent properties that are absent from the elements alone. Interactions can be defined in diverse ways, and these approaches acknowledge that the interactions of elements in a system are interconnected in ways that can be characterized and measured. These interactions may be pairwise or higher-order, physical or relational, small-scale or large-scale, and many more carefully selected definitions that define these relationships [Costa 2007, Mitchell 2009b]. Complexity science also acknowledges the dynamics of complex systems, whether of the interactions themselves or of the larger patterns of changes on the network [Holovatch 2017, Saxena 2020]. Complex systems find complexity in most, if not all, of these places, and the brain is no exception.

1.2 The Brain as a Complex System

In recent years, a significant amount of research has been done using complex approaches to study the brain [Bassett 2006, Hagmann 2007, Lillis 2008, Feldt 2011, Deco 2012, Litwin-Kumar 2012, Smith 2013, Allen 2014, Mazzucato 2015, Vidaurre 2017, Scholtens 2022, Brinkman 2022, Onuchin 2023]. When viewed as a complex system, the brain demonstrates complex dynamics on many physical and temporal scales. Great strides have been made in defining and studying various kinds of brain networks. Specifically, one can

define structural networks based on physical connections and functional networks based on brain activity. Structural and functional networks can be defined on small and large physical scales and studied as they change on short and long timescales.

On small physical scales, structural networks can be defined by the synapses or gap junctions between individual neurons [Scholtens 2022, Onuchin 2023]. Functional networks can be defined by correlations of spiking activity [Lillis 2008, Feldt 2011]. Apart from certain animals (e.g. *C. elegans*), these interactions generally create local rather than whole-brain circuits, and studies of small-scale networks are most often performed on animals or through simulation.

On large physical scales, structural networks can be defined by diffusion MRI tractography and related methods [Hagmann 2007]. Functional networks can be defined by statistical dependencies in time series between brain regions [Bassett 2006, Smith 2013]. These whole-brain networks often sacrifice single-neuron resolution to explore the whole brain. These kinds of studies are able to be performed non-invasively on human populations.

Several studies have explored the dynamics of these networks on short timescales. In small-scale networks, spiking activity reveals metastable dynamics that transition between different states, which have been investigated using modeling approaches. At the cellular level, these dynamics are often explored with recurrent network models of spiking neurons [Deco 2012, Litwin-Kumar 2012, Mazzucato 2015, Brinkman 2022]. The large-scale networks have shown similar state transition dynamics using methods like sliding-window functional connectivity and hidden Markov Models [Allen 2014, Vidaurre 2017, Zuo 2017].

However, the long-term dynamics of these networks are still poorly understood. Many studies have reported trends across larger timescales [Fair 2008, Hagmann 2010, Tomasi 2012, Gu 2014, Chan 2014, Sala-Llonch 2015, Betzel 2019, Deery 2023], and very few studies utilize dynamical approaches to study how these networks change over time [Shappell 2019, Scheinost 2019]. Dynamical approaches are able to go beyond the overall trends of what changes are occurring over time to address questions of underlying patterns in the system. These dynamics can begin to reveal how changes occur rather than just what changes occur over long timescales.

1.3 Network Dynamics

This project is designed to contribute to filling this gap in the literature by utilizing a dynamical approach to studying brain networks over time. There are several methods for studying long-term network dynamics in networks of other complex systems, most especially in social networks. These approaches include longitudinal network models [Duxbury 2023], event-based models [Leifeld 2015, Duxbury 2023], and simulation models

[Welch 2011, Zhang 2019]. Each of these approaches has different advantages, limitations, and assumptions. Understanding these allows for the selection of an approach to apply to brain networks. Longitudinal network models are able to integrate several complex network behaviors and test specific hypotheses, but include strong assumptions and a discrete timescale [Duxbury 2023]. Event-based models are also able to integrate several complex network behaviors and use a continuous timescale, but require knowledge of specific network changes [Leifeld 2015, Duxbury 2023]. Simulation models are highly customizable and explanatory for any kind of network, but are difficult to tune and sensitive to initial assumptions [Welch 2011, Zhang 2019]. All of these approaches attempt to explain complex dynamics on the network. For this work, a longitudinal network approach was selected for its explanatory power, testability, and dataset compatibility. Specifically, the stochastic actor-oriented model (SAOM) was selected [Snijders 2010, Kim 2017]. This model postulates a set of factors that drive change on the network. The goal of this work is to apply the SAOM to brain networks, specifically, functional and structural human brain networks in an aging population.

1.4 Aging

Human brains experience many changes throughout the lifetime. Recent research has brought insight into the changes in brain structure and function in later life [Tomasi 2012, Dai 2014, Brier 2014, Chan 2014, Betzel 2014, Sala-Llonch 2015, Zuo 2017, Soman 2020, Deery 2023, Schulz 2024, Jauny 2024, Ranasinghe 2024, Kalpouzos 2025]. Understanding these changes dynamically is essential as populations in Canada and other peer nations continue to age [Public Health Agency of Canada 2020]. More individuals will experience the effects of age, and more resources will be required for the care of this population. Additionally, 6.3% of adults 65 and older live with cognitive impairment [Canadian Insitute for Health Information 2018]. This disability has a profound impact on the lives of these individuals, and more insight is needed to understand the progression of this disease.

High-level studies of brain networks across the lifespan have revealed several consistent patterns [Betzel 2014, Zuo 2017, Deery 2023]. Structural and functional networks tend to show decreases in modularity and global efficiency with age, reflecting a shift toward less segregated and more integrated network organization [Betzel 2014, Deery 2023]. These changes are interpreted in the context of dedifferentiation theories, which suggest that functional specialization diminishes with age [Chan 2014].

Studies of cognitive impairment have identified consistent patterns of structural and functional network disruption. Networks in individuals with Mild Cognitive Impairment (MCI) often show decreased modularity, reduced global efficiency, and altered hub connectivity compared to their same-aged peers, reflecting a breakdown in the balance between segregation and integration [Dai 2014, Brier 2014, Ranasinghe 2024].

Together, these patterns provide a foundation for understanding long-term network changes and further motivate the application of the SAOM to investigate how these networks age and how diseases like MCI progress dynamically.

This project attempts to fill a gap in our understanding of long-term brain dynamics by applying the stochastic actor-oriented model to functional and structural brain networks. This project will develop models of network change in aging to provide greater insight into aging and cognitive impairment.

1.5 Research Objectives

The goal of this project is to develop a set of longitudinal models of network change in the aging brain. To achieve this goal, the specific objectives are as follows,

1. Develop a data-driven procedure for deriving factors in SAOM and evaluate the procedure on a simulated dataset.

2. Apply the procedure to functional and structural aging brain data to derive models of network change over time.

3. Analyze and compare the resultant longitudinal models to demographic measures of impairment, sex, and age to understand the models in the context of aging and neurodegenerative illness.

Chapter 2

Background

This project, as with most interdisciplinary projects, requires background from a number of sources, including physics, neuroscience, mathematics, and computer science. I have included in this chapter relevant background information while keeping in mind the greater complexities of the subject matter in all categories.

This project is focused on building models of change using brain imaging data. The overall models are highly complex and require careful consideration of the measurements, assumptions, and applicability at each level of complexity. I will begin by discussing the imaging data itself and the physical elements being measured. Second, I will discuss the unique advantages and assumptions of the formation of networks from this imaging data. I will, then, explore the measurements, assumptions, and applicability of the model-building approaches. The models in this project are stochastic models, which require stochastic approaches to various components of the models. Therefore, I will discuss the background of stochastic models generally and the relevant stochastic approaches applied in the models of this project.

2.1 Brain Imaging

Non-invasive imaging techniques have been utilized for decades to better understand the structure and function of the brain. Since these techniques are non-invasive, a larger diversity of populations may be studied. In our research, we utilized functional magnetic resonance imaging (fMRI) and diffusion tensor imaging (DTI) to access information about the function and structure of aging brains. In this background section, I will discuss how these imaging techniques work, their history, and their current use in research in order to answer a basic question—how are these imaging techniques able to retain functional or structural information about the brain? Additionally, this section will underpin many of the actions that are required during data preprocessing (Chapter 3).

2.1.1 Magnetic Resonance Imaging

Magnetic Resonance Imaging (MRI) forms the basis of both fMRI and DTI. The premise of MRI images is that the behavior of molecules differs in various kinds of tissues in the body. Knowing that tissues produce different signals under the electromagnetic conditions of an MRI machine allows for the building of an image from the measured values. Different MRI sequences are used to produce different kinds of images, like those for fMRI and DTI; however, they all contain a few important components. These components occur in various combinations in the different MRI sequences.

MRI begins with the introduction of the main magnetic field (B_0) along the body (z-axis), which influences the magnetic moments of atoms. In B_0, these atoms will have a *net magnetization vector* that is in the direction of the magnetic field, and the procession of these atoms will be at a set frequency. The frequency of these atoms is dependent on the magnetic field and the type of atom, but not on the type of tissue being imaged. This frequency is referred to as the *Larmor frequency*,

$$f_0 = \gamma B_0 \tag{2.1}$$

where γ is the gyromagnetic ratio for the specific atom (in most cases, we will be discussing hydrogen $\gamma = 42.58\ \text{MHz}\,\text{T}^{-1}$).

So far, no signal is produced as there is no transverse magnetization, magnetization perpendicular to B_0. A *radiofrequency pulse* equal in frequency to the Larmor frequency is introduced. This induces resonance; the atoms will flip to contain some transverse component. Radiofrequency pulses in MRI are often titled after the flip angle by which the pulse changes the net magnetization vector. The flip angle is directly dependent on the duration of the pulse. A 90° pulse will induce the maximum transverse magnetization, and other flip angles are often used to save scanning time [Bernstein 2004].

Once a radiofrequency pulse is applied, the process of relaxation can be split into two components—$T1$ relaxation, the recovery of *longitudinal magnetization*, and $T2$ relaxation, the loss of *transverse magnetization*.

$T1$ relaxation, or the recovery of longitudinal magnetization, is highly dependent on the type of tissue to which the atom belongs. $T1$ relaxation occurs under spin-lattice interactions. These are the interactions between the atoms of interest and other materials in the tissue. $T1$ refers to the time that it takes for 63% of the longitudinal magnetization to recover after a 90° radiofrequency pulse. The direct measurement of $T1$ relaxation is not possible as only transverse magnetization is measurable. However, upon a repetition of another 90° pulse, only the recovered longitudinal magnetization will be impacted by this second pulse, and the contrast between various tissues will be measurable. The time to repetition, TR, refers to the time at which the second 90° pulse is applied.

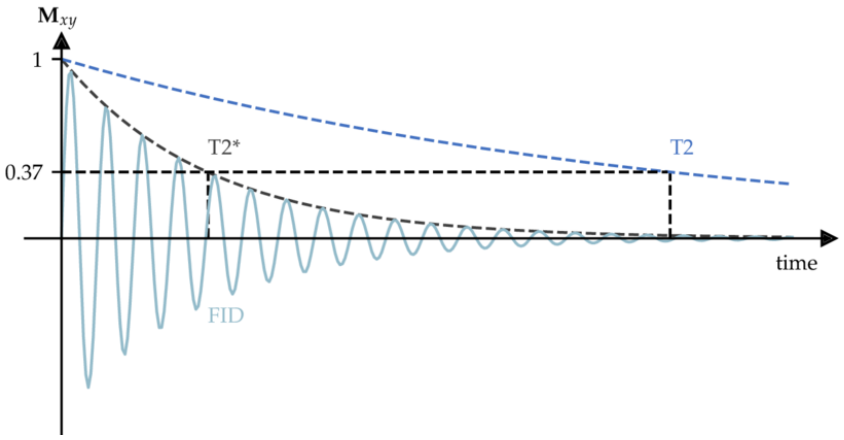

Figure 2.1: **Comparison of $T2$ curves.** In this graph, reproduced from Denck [Denck 2022], the differences between the $T2^*$ decay and the $T2$ decay, demonstrating the more rapid decline of the $T2^*$ curve due to magnetic heterogeneity.

$T2$ relaxation, or the loss of transverse magnetization, is the process by which the atoms fall out of phase with one another. It is also highly dependent on the type of tissue to which the atom belongs and is considered independent of the $T1$ relaxation. There are two different values of $T2$: $T2$ and $T2^*$. $T2^*$ refers to the time that it takes for 63% of the transverse magnetization to be lost after a 90° radiofrequency pulse under free induction decay. This, however, includes the relaxation of transverse magnetization due to spin-spin interactions as well as due to magnetic field heterogeneity. Magnetic field heterogeneity refers to any local distortions in the magnetic field due to the scanner, magnetic materials in the body, or local magnetic fields from nearby atoms. $T2^*$ shows a very rapid decay in the transverse magnetization, which is often unwanted in the creation of MRI images. Figure 2.1 shows the differences between $T2^*$ decay and $T2$ decay [Denck 2022].

$T2^*$ effects can be compensated for to better reflect the $T2$ curve, or the loss of transverse magnetization under spin-spin interactions alone. This is the interaction between the atoms of interest and themselves. Compensation is done through a 180° radiofrequency pulse, which reverses the positions of differing decay rates so that faster decaying atoms are forced to catch up with slower decaying atoms. Thus, at a time after the 180° pulse equal to the time between the 90° and 180° pulses, all the decaying atoms will be in phase once again. This time is referred to as the time to echo or TE, and it is when the signal is measured. This eliminates the effects of magnetic field heterogeneity, which creates those faster and slower decaying atoms.

As previously stated, different MRI sequences will adjust components, like TR and TE, in order to access relevant information. A shorter TR and TE will mean that most of the contrast between tissues is due to the $T1$ curve. This is called a $T1$-weighted image. A longer TR and TE will mean that most of the contrast between regions is due to the $T2$ curve. This is called a $T2$-weighted image.

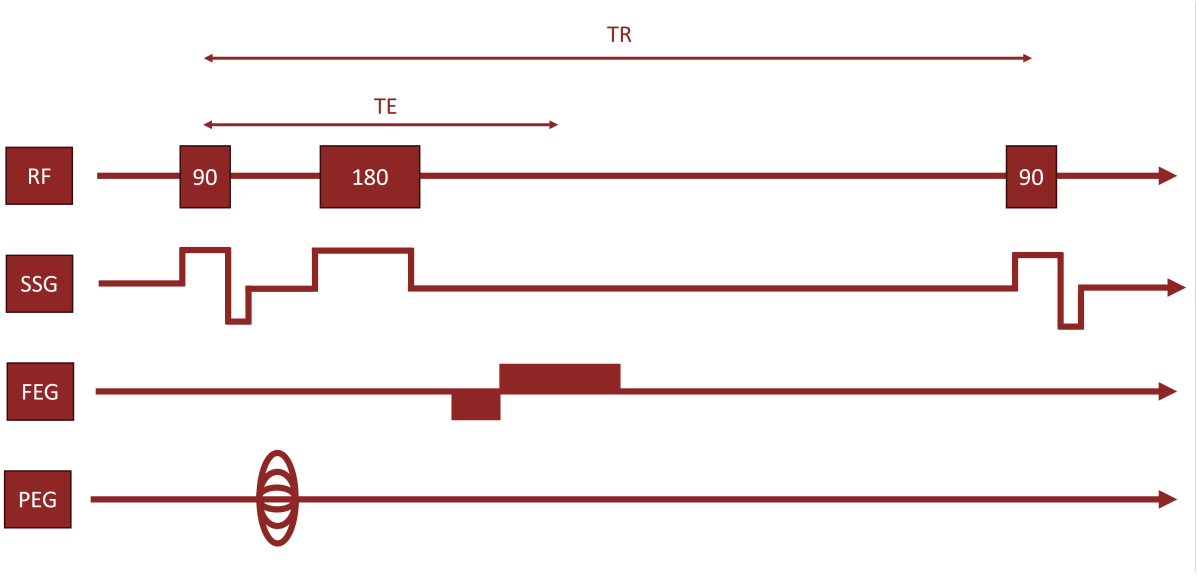

Figure 2.2: **Timing diagram for the spin echo sequence used in MRI.** This diagram shows the radio frequency pulses (RF), the slice selection gradient (SSG), the frequency encoding gradient (FEG), and the phase encoding gradient (PEG). This figure was adapted from those shown in these tutorials [Nel 2023].

When a radiofrequency pulse is applied, the signal measured is the net magnetization vector, meaning that all the spatial information is lost. *Spatial encoding* is done for each of the three spatial axes by introducing gradients at different times in order for the signal to contain unique information about all three axes that may be decoded. The z-axis introduces the slice selection gradient (SSG), the x-axis introduces the frequency encoding gradient (FEG), and the y-axis introduces the phase encoding gradient (PEG); each encodes on a different component of the signal. Figure 2.2 shows the spin echo sequence that is used for anatomical MRI scans that are required for coregistration of the fMRI and DTI images.

The slice selection gradient (SSG) is applied along the z-axis, meaning that instead of all areas of the body along the z-axis experiencing a magnetic field B_0, regions on one end of the axis will experience a higher magnetic field. In applying this gradient, it means that only a certain slice of the z-axis will have a Larmor frequency that matches the radiofrequency pulse. Thus, only that narrow slice will have resonance and produce a signal. As a result, particular slices of the z-axis can be selected by applying a radiofrequency pulse that corresponds with the Larmor frequency of that slice.

The frequency encoding gradient (FEG) is applied along the x-axis during the time surrounding TE, varying the frequency of the signal along that axis. The measured signal collected multiple times around TE is then a summation of different frequency signals; thus, one can apply a Fourier transform to separate which parts of the signal are coming from which column of the slice.

The phase encoding gradient (PEG) is applied along the y-axis between the 90° pulse and the 180° pulse; however, these differing phases cannot be measured in isolation, only in comparison to each other. Thus,

different strength phase encoding gradients are applied upon repeated 90° pulses at TR.

The frequency encoding gradient measures and the phase encoding gradient measures can be combined into an image known as k-space, where a 2-dimensional Fourier transform can be applied in order to decode the gradient values and calculate the signal value for each location (voxel) in the image.

The spatial resolution of an image can be understood from the protocols of spatial encoding. Specifically, the z-axis spatial resolution is determined by the number of slices into which the z-axis is split. The x-axis spatial resolution is determined by the number of measurements taken during the recording at TE. The y-axis spatial resolution is the number of phase alteration measures. Other sequences and protocols are used to obtain different types of information, like those in fMRI and DTI. Understanding these protocols will elucidate how they encode functional and structural information.

2.1.2 Functional Magnetic Resonance Imaging

One may notice that, in the original spin echo sequence, there is no temporal information that is encoded, and the protocols of the spin echo sequence require multiple radiofrequency pulses in order to collect all the spatial information. In order to encode functional information, as is done in fMRI, the sequence of collecting MRI information is altered to obtain temporal information and utilize a convenient reality about physiology and blood cells.

Cells in the body, including neurons, require oxygen in order to perform their various functions. Oxygen is transferred to neurons by red blood cells traveling through a network of arteries and veins. However, the amount of oxygen going to various neurons in the brain is not constant; it fluctuates during different cognitive and behavioral activities. These changes alter the ratio of *oxygenated blood* to *deoxygenated blood*. The first major assumption of fMRI is that changes to the amount of oxygen going to a particular region indicate greater activity in that region. This is a well-established theory with significant evidence from both the understanding of metabolic biology [Davis 1998, Thompson 2018] and correlations with other measurements of brain activity [Uğurbil 2003, Kim 2004]. It is important to note, therefore, that fMRI does not measure brain activity directly and instead relies on the metabolic consequences of brain activity.

When a neuron is more active, the blood vessels near that neuron dilate to allow greater amounts of oxygenated blood to flow, even more than is required for that neuron to fire as often as it does during the activity. Thus, it is found that the ratio of oxygenated blood to deoxygenated blood both upstream and downstream of a neuron increases with increased activity. This allows for measurement of the ratio of oxygenated to deoxygenated blood to remain meaningful even when the spatial resolution is not near the neuronal level.

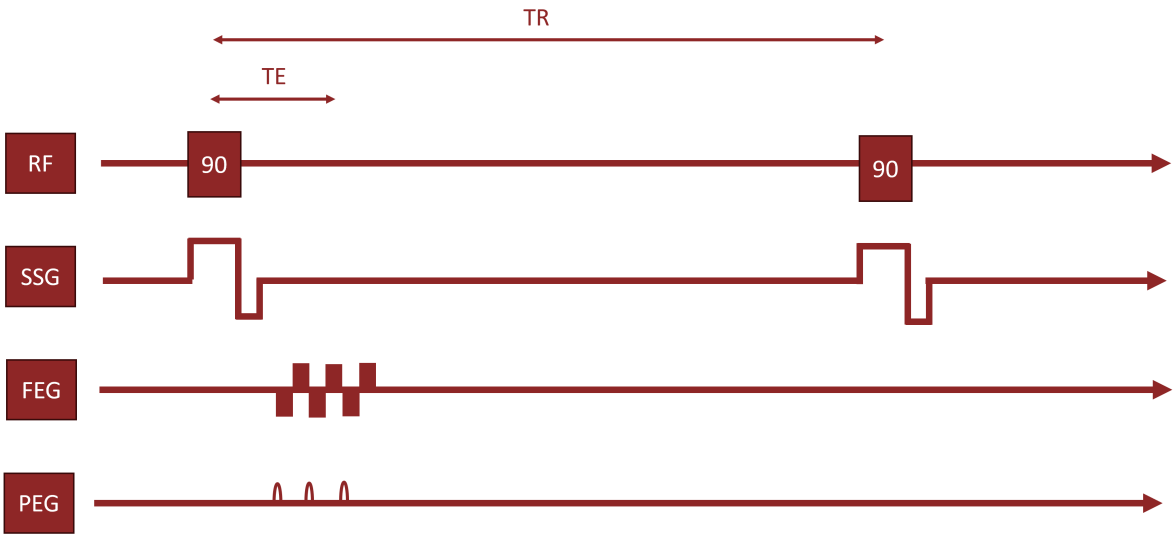

Figure 2.3: **Timing diagram for the echo planar sequence used in fMRI.** The diagram shows the radio frequency pulses (RF), the slice selection gradient (SSG), the frequency encoding gradient (FEG), and the phase encoding gradient (PEG). This figure was adapted from those shown in these tutorials [Nel 2023].

Red blood cells have a molecule called hemoglobin, which binds to oxygen molecules in order to carry oxygen to cells throughout the body. Hemoglobin relies on an atom of iron, which binds to the oxygen. In oxygenated blood, there are oxygen molecules bound to the iron in the hemoglobin, making the entire molecule less paramagnetic than its deoxygenated counterpart. This means that there is a disruption to the magnetic field when there is a higher proportion of deoxygenated blood.

This has major ramifications for the use of MRI to detect activity in the brain. Recall that when discussing the $T2^*$ curve vs. the $T2$ curve, it is seen that the $T2^*$ curve under free induction decay is impacted by local alterations to the magnetic field (Figure 2.1). The local magnetic field distortions in deoxygenated blood are seen in the $T2^*$ decay and allow for the measurement of contrast between moments of higher brain activity, with lower distortions from deoxygenated blood, and moments of lower brain activity, with higher distortions from deoxygenated blood. Thus, the MRI sequence for fMRI is specifically designed to measure during the $T2^*$ decay and eliminate the 180° pulse to re-phase. This allows for a level of temporal resolution not possible in the traditional spin echo sequence, but does sacrifice some of the spatial resolution as there is only a shortened version of the spacial encoding procedures that discriminate the x and y axes.

In Figure 2.3, the sequence for fMRI is presented. This sequence is known as the echo planar sequence. It retains all the required parts of the scan, but on a much faster timescale. The temporal resolution is often worth the losses in spatial resolution in fMRI, especially when there is a regular anatomical image with which the fMRI data can be registered.

The data collected in fMRI is considered functional because it is connected with brain activity rather than just brain structure. Often, these kinds of scans are conducted when a participant is engaged in a task or activity, and the fMRI data indicate which regions are more active during that task or activity. The scans in this project are, instead, conducted in the *resting state* where individuals are not asked to complete any tasks during scanning. The resting state is viewed as a measure of spontaneous brain activity and connectivity in the absence of targeted behavior [Gonzalez-Castillo 2021] and has been used in many studies of functional brain networks [Eguíluz 2005, Bassett 2006].

It is important to note that the temporal resolution is on the scale of a few seconds and cannot be considered instantaneous. This resolution comes both from the fact of measuring a metabolic consequence of brain activity and from the realities of the spatial encoding that, while improved in the echo planar sequence, remain a drag on temporal resolution.

2.1.3 Diffusion Tensor Imaging

The second form of MRI used in this project is diffusion tensor imaging (DTI). This is a measure of structural information about the brain that can be formed into a network. DTI relies on the physical structure of axons and their interaction with water molecules.

The brain is made of neuronal cells, which have a number of components, including the axon, the elongated portion of the neuron that transports signals from one location to another inside the brain. Axons make up a large proportion of the neuron's size and volume [Muzio 2025]. Thus, one can understand the connectivity between regions by viewing the pathways created by the axons, especially in the axon-dense white matter of the brain.

There is a lot of water in the human body, including inside the brain. This water serves many purposes, including acting as a solvent of ions essential for the electrical properties of the brain [Kimelberg 2004]. The water molecules are constantly undergoing small movements and fluctuations known as Brownian motion; however, the molecules are not free to move in any direction. The motion, considered random when unimpeded, can be restricted by non-permeable membranes. In this case, the net movement would not be zero, but would be greater in the direction of the membranes. Axons, coated in fatty myelin sheaths, impede the random motion of water molecules, meaning that water is more likely to move along the axon than across the axon [Aung 2013]. This kind of movement is called *anisotropic*, because it is restricted in direction.

MRI machines are able to detect this restriction in movement using a new form of the echo planar sequence where the 180° pulse is reintroduced. This new sequence introduces more gradients on various directional axes (in order to do tensor analysis, there must be six directions). A gradient is introduced before the 180°

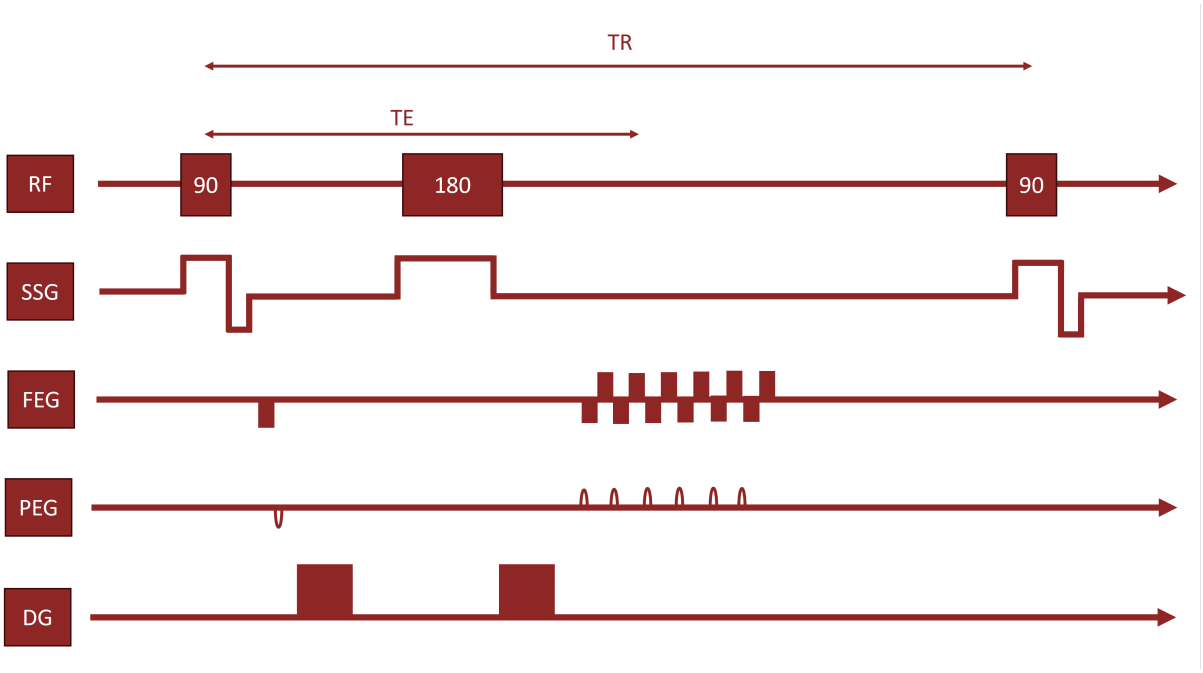

Figure 2.4: **Timing diagram for the echo planar sequence used in DTI.** The diagram shows the radio frequency pulses (RF), the slice selection gradient (SSG), the frequency encoding gradient (FEG), the phase encoding gradient (PEG), and the diffusion gradient (DF). This figure was adapted from those shown in these tutorials [Nel 2023].

pulse, and a second equivalent gradient is introduced after the pulse. The second gradient is considered equal and opposite of the first gradient due to the reversal of the procession after the pulse. These diffusion gradients (DG) are far stronger than those introduced for spatial encoding. Under free induction decay (before the 180° pulse), some molecules will be processing faster than others. If the molecules experience the equal and opposite magnetic field before and after the pulse, they will follow the original $T2$ decay curve. However, if the molecules are free to move, they may not experience the equal and opposite magnetic field before and after due to moving into a different part of the gradient. Thus, molecules that are less restricted in their movement along the given axis will lose their transverse magnetization faster and produce a lower signal. Figure 2.4 shows the echo planar sequence for DTI with a new line labeled DG that shows the timing of the diffusion gradients.

DTI measures structural information as the shape of the axons affects the way in which the water molecules are able to diffuse. It is important to understand that DTI does not image to the scale of single axons, but instead represents the general tracts along which motion is more limited by axons. DTI is a well-established measure of the tract structures in the brain and has been confirmed in other kinds of anatomical analyses [Conturo 1999, Wakana 2004]. The connections between structural and functional connectivity, as well as the ways in which this connectivity changes over the lifetime, remain open areas of research, so the

networks that are formed from fMRI and DTI scans represent a strong dataset for the research conducted here.

2.2 Graph Theory

These networks produced from MRI images are prime candidates for analysis using graph theory. Graph theory is a branch of mathematics that began in the 18th century to study problems of connectivity [Euler 1741]. The field has since expanded to applications across many disciplines [Biggs 1986, Gross 2005].

The object at the core of graph theory is that of a graph, or network, containing nodes, the components of the network, and edges, the connections between those components. The networks that can be studied in graph theory can be weighted, where edges have some continuous scale, or unweighted, where the edges are binarized. The networks can be directed, where the edges have one-way directionality, or undirected, where the edges have no directionality. The pattern of edges can be represented as an *adjacency matrix* of size NxN where N is the number of nodes in the network. The formation of networks in this manner allows for the quantification of the interactions between elements in a system and provides insight into its complex behaviors.

There are a number of measures that are derived from these networks, which demonstrate the insights that may be derived from these graphs. *Degree*, the measure of the connectivity of individual nodes, can highlight highly connected *hubs* and lower connected peripheral nodes. The *clustering coefficient*, the fraction of a node's neighbors that are connected, captures the local connectivity and triangle formation in the network. The *path length*, a measure of the number of steps on the network between two nodes, can provide insight into the efficiency of information transfer in the network. *Betweenness*, the measure of how often a node appears on shortest paths, highlights nodes that are critical for information transfer on a network. *Modularity* and *community structure*, measures of densely connected subnetworks, may highlight similarities or shared functions of certain nodes in the network. The ratio of connectivity between communities and connectivity within communities is referred to as the *integration* vs. *segregation* of the network. Measures such as these contribute to our understanding of overall *topology*, *efficiency*, and *robustness* of networks.

The application of graph theory to neuroscience is a relatively young field and has provided a greater understanding of the complexity of the brain since around the turn of the 21st century [Sporns 2005, Eguíluz 2005]. Beginning with studies of structural connectivity [Sporns 2005], the field quickly expanded to functional connectivity from functional magnetic resonance imaging (fMRI) [Eguíluz 2005, Bassett 2006], electroencephalogram (EEG) [Reijneveld 2007], and magnetencephalogram (MEG) studies [Reijneveld 2007, Stam 2009].

A key insight from these applications includes evidence of small-world topology [Sporns 2005, Bassett 2006, Reijneveld 2007, Stam 2009] where the clustering is high and the average shortest path length is low. These networks are thought to optimize efficiency and local specialization. Another key insight is the understanding of the highly connected hubs that are found in the brain, including the precuneus and posterior cingulate cortex [Hagmann 2007, Buckner 2008]. The final key insight I will highlight here is the consistency of community structure with subnetworks linked to particular brain functions [Meunier 2009, Power 2011, Yeo 2011, Betzel 2013].

The relationship between functional and structural networks has been an area of research throughout the study of brains using graph theory [Sporns 2005, Bassett 2006, Hagmann 2008, Honey 2009, Deco 2011, Hutchison 2013]. Functional and structural networks show highly correlated topology [Hagmann 2008, Honey 2009]; however, functional networks demonstrate greater dynamic flexibility beyond structural constraints [Deco 2011, Hutchison 2013].

Graph theoretical approaches to studying brain networks have been a significant area of research into both healthy and diseased brain processes. Understanding the connectivity in the brain can highlight emergent network-level properties that can more robustly explain cognitive outcomes. In pathology, these graph theoretical approaches highlight network *vulnerabilities* like in hub disruption in Alzheimer's Disease [Buckner 2008], *resilience* like in the alternative pathways used after traumatic brain injury [Caeyenberghs 2017], and *compensation*, like in the functional reorganization in Multiple Sclerosis [Shirani 2022].

Bridging mathematics and neuroscience through graph theory allows for quantitative comparisons across individuals, populations, and disease states. This study applies the principles of graph theory to understand the functional and structural networks in an aging population.

2.3 Stochastic Models

Stochastic models are the types of models that include elements of randomness and uncertainty as features of the models themselves [Taylor 2014, Lanchier 2017]. These are important tools of complexity science and demonstrate promise in filling the gap in the research surrounding the dynamics of brain networks at longer timescales. Stochastic models describe systems where the outcomes are probabilistic rather than deterministic, incorporating real-world elements like randomness, uncertainty, and noise [Taylor 2014, Lanchier 2017]. These models have a unique ability to capture the variability of complex systems and give insight into behaviors that are often obscured by uncertainty. Stochastic models are used in a variety of complex systems, including weather and climate [Franzke 2015], ecology [Marrec 2023], and economics [Madan 2010]. These models are often able to capture the noise of the real world and simulate emergent phenomena [Tay-

lor 2014, Lanchier 2017].

Stochastic models present unique challenges through computation, statistical power, and complexity trade-offs. These models must strike a balance between oversimplification and overfitting in order to best address the questions that are posed [Taylor 2014, Lanchier 2017]. These models are, by their nature, not entirely mechanistic nor do they provide the neat predictions of deterministic models; however, they provide insight into the various levels of complexity, clarity to underlying phenomena, and understanding of emergence in complex and varied real-world systems.

2.3.1 Stochastic Actor-Oriented Model

The stochastic actor-oriented model (SAOM) is a specific stochastic model that draws on longitudinal data to describe the factors that drive change on the network [Snijders 2010]. This model was developed by Tom Snijders in 1996 [Snijders 1996]. He and his colleagues have since developed resources for the implementation of these models on various networks, including the R-based software for Simulation Investigation for Empirical Network Analysis (RSiena) [Lospinoso 2019, Snijders 2024, Snijders 2025]. The original design of the SAOM was to study social networks and the person-driven mechanisms of changes to that network that produce emergent social phenomena over time. These models have been applied widely not only to various interpersonal social networks [Stadtfeld 2015, Quintane 2013, Lewis 2012], but also animal [Fisher 2017], financial [Xing 2023], and macro social networks [Mohrenberg 2017]. It is evident from these applications that the SAOM is able to be applied to many kinds of networks with careful consideration of the interpretation.

The factors in the model are often pulled directly from graph theoretical measures such as degree and betweenness to incorporate network interaction into the mechanism of network change [Snijders 2010]. By quantifying node-level mechanisms that impact network evolution, the SAOM is able to connect node-level decisions with emergent phenomena.

The next two sections will discuss the theoretical principles of the SAOM, including the continuous-time Markov chain, which forms the basis for time handling in these models, and the stochastic approximation methods, which are utilized to estimate and evaluate parameters in the model.

2.4 Continuous-Time Markov Chain

The models utilized in this project conduct time handling based on the continuous-time Markov chain. A Markov chain is a stochastic model that describes the probability of various states and the transitions between them. Fundamental to the Markov chain is the notion that probabilities only depend on the current state and not on any previous states. For example, if I begin in *state a* then transition into *state b*, the

next transition is affected only by being in *state b* with no memory of ever having been in *state a*. This memorylessness is known as the *Markov property*.

The Markov chain can be represented as a matrix (A) of probability values that describe the likelihood of transitioning to one state given the current state . The row represents the current state, while the column represents the potential next state. The diagonal values of this matrix are meaningful in that they describe the probability of remaining in the current state and not making a transition.

This can then be applied across multiple time steps where the probability of transitioning from *state a* to *state b* can be represented as,

$$Pr(X_b|X_a) = A_{ab} \tag{2.2}$$

The subsequent transition to say *state c* is ignorant of the original state (a). Thus, that probability is only dependent on the current state (b). If we would like to write the probability of getting from *state a* to *state c* in two time steps, we need to consider all the ways that it could get there (in an example with just 3 states this would be $a \to a \to c$, $a \to b \to c$, $a \to c \to c$). This can be written as,

$$\sum_n Pr(X_n|X_a)Pr(X_c|X_n) = \sum_n A_{an}A_{nc} \tag{2.3}$$

To generalize, it can be shown that transitioning from any state to any other state in two time steps can be represented by squaring the original matrix. This can be even further generalized to show that the original matrix A raised to a power s is the set of probabilities of transitioning between states in s time steps.

$$P(s) = A^s \tag{2.4}$$

However, this representation is limited to discrete time steps rather than a continuous timescale. Thus, it is necessary to adjust our understanding of this concept. The following probability relationship can be derived from the conclusions drawn about the discrete-time Markov chain for changing the number of time steps.

$$P(m+n) = A^m A^n = P(m)P(n) \tag{2.5}$$

The relationship between subsequent probabilities ($P(m)P(n)$) can be applied to the definition of a derivative, and, with some knowledge of differential equations, we say something about the probabilities in the continuous-time regime.

$$\frac{dP(t)}{dt} = \lim_{\delta t \to 0} P(t)\frac{P(\delta t) - I}{\delta t} \tag{2.6}$$

where I is the identity matrix.

$$\frac{dP(t)}{dt} = P(t)Q \tag{2.7}$$

$$P(t) = e^{Qt} \tag{2.8}$$

This is the probability of particular transitions after some time t has elapsed.

The question remains — what does the value Q really represent and how might it be defined within the model? From Equation 2.6,

$$Q = \lim_{\delta t \to 0} \frac{P(\delta t) - I}{\delta t} \tag{2.9}$$

This equation indicates that Q is the rate of transitions between various states. If λ_{ab} is the rate of transition between *state a* and *state b*, the Q rate matrix (with 3 states) would be,

$$Q = \begin{bmatrix} -\lambda_{ab} - \lambda_{ac} & \lambda_{ab} & \lambda_{ac} \\ \lambda_{ba} & -\lambda_{ba} - \lambda_{bc} & \lambda_{bc} \\ \lambda_{ca} & \lambda_{cb} & -\lambda_{ca} - \lambda_{cb} \end{bmatrix} \tag{2.10}$$

With this understanding, the continuous-time Markov chain can be split into two equations, which both follow the Markov property. The first is the *holding-time distribution*, and the second is the *jump-chain probability*. These two equations together describe the non-uniform time between changes in state and the probability of particular transitions.

The holding-time distribution can be derived from Equation 2.8. Instead of viewing the decision as the transitions from any state to any other state, the holding-time distribution describes the probability of the binary choice between making or not making any transition. This utilizes the diagonal values of the matrix e^{Qt} in the probability equation 2.8, which indicate the probabilities of not making a transition, after some time t, given a current state. Thus, the probability of making any transition at any point in time span, t, given a current state (in this case *state a*) would be,

$$P_a(t) = 1 - e^{Q_{aa}t} = 1 - e^{(-\lambda_{ab} - \lambda_{ac})t} \tag{2.11}$$

This is the cumulative distribution function of the exponential distribution with a mean of $1/(\lambda_{ab} + \lambda_{ac})$. All this means that the time between transitions follows an exponential distribution, a memoryless distribution.

The jump-chain probability (J) can be derived conceptually from the matrix Q. This is the probability of making a particular transition (in this case *state a* to *state b*) at some instantaneous time, t. This can be

defined as the conditional probability of being in *state b* at time $t + \delta t$ given not being in *state a* at time $t + \delta t$ and being in *state a* at time t as δt goes to zero.

$$J_{ab} = \lim_{\delta t \to 0} Pr(X_{t+\delta t} = b | X_{t+\delta t} \neq a, X_t = a) \tag{2.12}$$

This can be rewritten as,

$$J_{ab} = \lim_{\delta t \to 0} \frac{Pr(X_{t+\delta t} = b, X_{t+\delta t} \neq a | X_t = a)}{Pr(X_{t+\delta t} \neq a | X_t = a)} \tag{2.13}$$

This can be interpreted as the rate of going from *state a* to *state b* divided by the rate of changing from *state a* to anything which can be pulled directly from the matrix Q. Thus,

$$J_{ab} = \frac{\lambda_{ab}}{\lambda_{ab} + \lambda_{ac}} \tag{2.14}$$

This is sometimes called the embedded Markov chain, which behaves similarly to a discrete-time Markov chain, which is, of course, memoryless. The Markov property of memorylessness is a common approach for simplifying highly complex systems for modeling [Kampen 1992, Levin 2009, Gardiner 2010]. The continuous-time Markov chain is the basis for the time handling in the SAOM.

2.5 Stochastic Approximation

In the implementation of the SAOM, the weights of the various factors are estimated through stochastic approximation—specifically, the method involves the generalized method of moments and the Robbins-Monro algorithm. The adaptation utilized in the SAOM is already implemented in Rsiena; I will lay out the theoretical and computing principles here to better connect these concepts with the goals and limitations of the derived models.

2.5.1 Generalized Method of Moments

The generalized method of moments (GMM) is a method for estimating parameters. It is used in the estimation of the SAOM factor weights. The GMM is based on the method of moments, which postulates that, if a population has a mean of μ, then a sample of that population with size n can be used to approximate that mean $\hat{\mu} = \frac{1}{n}\sum_i^n X_i \approx \mu$. Similarly, other moments like the variance can be calculated to estimate the population value for sufficiently large sample sizes ($\hat{\sigma}^2 = \frac{1}{n}\sum_i^n (X_i - \hat{\mu})^2 \approx \sigma^2$). However, if a greater number of statistical criteria (moments) are included compared to the number of parameters for which we are solving, there is no exact solution. The GMM simultaneously minimizes the divergence of these criteria.

The goal is to estimate the parameters, $\hat{\theta}$, based on a sample by minimizing the criteria in a function g. The function g of true parameters θ^* can be defined where,

$$E[g(\theta^*)] = 0 \tag{2.15}$$

The function g contains the moment criteria to be minimized. This expectation generally cannot be measured directly, so a sample, X, of n values can yield a sample mean, $\bar{g}$,

$$\bar{g}(\theta) = \frac{1}{n}\sum_{i}^{n} g(X_i, \theta) \tag{2.16}$$

The estimation of parameters, $\hat{\theta}$, generalizes the minimization condition of the method of moments, the deviation of $\bar{g}$ from zero. This yields,

$$\hat{\theta} = \underset{\theta}{\operatorname{argmin}}(Q(\theta)) \tag{2.17}$$

$$Q(\theta) = \left|\left|(\bar{g}(\theta) - 0)^2\right|\right|_W = \bar{g}(\theta)^\top W \bar{g}(\theta) \tag{2.18}$$

where W is the optimal weighting matrix for the quadratic form (weighting of particular criteria over others).

Further manipulation of these equations and the introduction of some statistical principles can yield the covariance matrix $\Sigma_{\hat{\theta}}$ and the standard errors $SE(\hat{\theta})$ of the estimated parameters. This is done by applying the first-order condition and the central limit theorem to describe the asymptotic behavior of the $\hat{\theta}$ distribution. The first-order condition states,

$$\frac{\partial Q(\theta)}{\partial \theta} = 0 \tag{2.19}$$

In this case,

$$\frac{\partial Q(\theta)}{\partial \theta} = 2D_\theta^\top W \bar{g}(\theta) = 0 \tag{2.20}$$

where,

$$D_\theta = \frac{\partial \bar{g}(\theta)}{\partial \theta} \tag{2.21}$$

Because the value of $\hat{\theta}$ should converge around the true parameter values θ^*. We can perform a Taylor series expansion of $\bar{g}(\hat{\theta})$ about the true parameter values θ^*.

$$\bar{g}(\hat{\theta}) \approx \bar{g}(\theta^*) + D_{\hat{\theta}}(\hat{\theta} - \theta^*) \tag{2.22}$$

Some algebraic rearranging and combining of Equations 2.20 and 2.22 yields,

$$(\hat{\theta} - \theta^*) \approx (D_{\hat{\theta}}^\top W D_{\hat{\theta}})^{-1} D_{\hat{\theta}}^\top W \bar{g}(\theta^*) \tag{2.23}$$

Now the central limit theorem can be applied to two different distributions to describe the asymptotic behavior of the $\hat{\theta}$ distribution. First, the distribution of $\bar{g}(\theta^*)$ should converge to a normal distribution with an expectation value of zero and a variance of $\Sigma_{\theta^*} = E[g(\theta^*)g(\theta^*)^\top]$.

$$\sqrt{n}(\bar{g}(\theta^*)) \xrightarrow{d} \mathcal{N}(0, \Sigma_{\theta^*}) \tag{2.24}$$

Second, the distribution of our estimation of the parameters $(\hat{\theta} - \theta^*)$ should also converge to a normal distribution with an expectation value of zero and a variance of $\Sigma_{\hat{\theta}-\theta^*}$,

$$\sqrt{n}(\hat{\theta} - \theta^*) \xrightarrow{d} \mathcal{N}(0, \Sigma_{\hat{\theta}-\theta^*}) \tag{2.25}$$

$$\Sigma_{\hat{\theta}-\theta^*} = (D_{\hat{\theta}}^\top W D_{\hat{\theta}})^{-1} D_{\hat{\theta}}^\top W \Sigma_{\theta^*} W D_{\hat{\theta}} (D_{\hat{\theta}}^\top W D_{\hat{\theta}})^{-1} \tag{2.26}$$

$\Sigma_{\hat{\theta}-\theta^*}$ is calculated from Equation 2.23 and the central limit theorem. In practice, however, the value of Σ_{θ^*} cannot be measured directly, so we use the sample value of $\widehat{\Sigma_{\hat{\theta}}}$, which is,

$$\widehat{\Sigma_{\hat{\theta}}} = \frac{1}{n} \sum g(X_i, \hat{\theta}) g(X_i, \hat{\theta}) \tag{2.27}$$

That value is then used in the calculation of $\Sigma_{\hat{\theta}}$,

$$\Sigma_{\hat{\theta}} = (D_{\hat{\theta}}^\top W D_{\hat{\theta}})^{-1} D_{\hat{\theta}}^\top W \widehat{\Sigma_{\hat{\theta}}} W D_{\hat{\theta}} (D_{\hat{\theta}}^\top W D_{\hat{\theta}})^{-1} \tag{2.28}$$

From there, it is easy to determine the standard errors of the estimated parameters as the square root of the covariance matrix.

$$SE(\hat{\theta}) = \sqrt{\Sigma_{\hat{\theta}}} \tag{2.29}$$

The GMM forms the statistical basis of the estimation of the parameters in the SAOM. In the next section, we will discuss the algorithmic basis for the estimation procedure.

2.5.2 Robbins-Monro Algorithm

The algorithm that utilizes the GMM to estimate the parameters is the Robbins-Monro algorithm. Understanding this algorithm is essential for understanding the features, challenges, and assumptions of the models proposed in this project. Stochastic approximation techniques are a set of often-utilized approaches to optimization and root estimation problems and are especially useful for noisy data. Stochastic approximation is not exclusive to stochastic models like the SAOM; however, in these models, there is Markovian noise in addition to the noise from the dataset [Borkar 2006]. This additional noise reaffirms the necessity of a stochastic approximation approach and presents its own unique challenges.

The algorithm estimates the root ($\theta^* \in \mathbb{R}$) of a noisy function $M(\theta) = \alpha$. One could take measurements of the noisy function at various steps n to produce the random variable $Z_n \sim Z(\theta_n)$ and update the value theta to be closer to θ^*,

$$\theta_{n+1} = \theta_n + a_n(Z_n - \alpha) \tag{2.30}$$

The value a_n is the step size of the procedure and generally is reduced over the course of the estimation as the value of θ approaches θ^* [Robbins 1951].

Further updates were incorporated into the algorithm in subsequent papers. Specific to the estimation in the SAOM, the current equation does not specifically accommodate multivariate approximation and could still be optimized with the inclusion of Newton-like methods into the equation.

To generalize to multivariate parameters, the Robbins-Monro equation remains the same; however, θ, Z_n, and α all become vectors of length equal to the number of parameters to be estimated.

Further optimization can come from the inclusion of some Newton-like methods. Newton Methods for estimation utilize the derivative as the updating mechanism for estimation ($\theta_{n+1} = \theta_n - f(\theta_n)/f'(\theta_n)$) Including some derivative component in the update term improves the convergence speed and efficiency by rescaling the updates according to second-order information [Blum 1954].

In the multivariate condition, this derivative component is the Jacobian, which not only provides information on the scaling of the individual parameters but additional information on the interactions between parameters. This is very important for convergence when the parameters are not independent from one another and do not share a scale. If the Jacobian is held constant through the estimation, as is the case in SAOM, the algorithm equation is,

$$\theta_{n+1} = \theta_n - a_n D_{\theta_0}^{-1}(Z_n - \alpha) \tag{2.31}$$

Since the Jacobian is not calculated for each updating step, this algorithm is considered to be a Quasi-Newton method. This updated algorithm provides the basis for the factor estimation in the SAOM.

Interdisciplinary work requires one to synthesize information from many fields and track the impact across the scientific process. This survey of the relevant background information will inform the methods and results discussed in the rest of this thesis.

Chapter 3

Methods: Dataset and Network Construction

The next three chapters will walk through the methodology applied in this project. First, I will describe the dataset acquisition. Then, I will walk through the framework of the stochastic actor-oriented model. Finally, I will describe the novel procedures for deriving the models from the dataset. As suggested, this chapter will focus on data acquisition by introducing the dataset and describing the preprocessing and network formation for that dataset. We were not involved in the collection of this data from participants, but conducted all the necessary preprocessing to study it.

3.1 Dataset

Data used in the preparation of this project were obtained from the Alzheimer's Disease Neuroimaging Initiative (ADNI) database (`adni.loni.usc.edu`) [Petersen 2009]. The ADNI was launched in 2003 as a public-private partnership, led by Principal Investigator Michael W. Weiner, MD. The primary goal of ADNI has been to test whether serial magnetic resonance imaging (MRI), positron emission tomography (PET), other biological markers, and clinical and neuropsychological assessment can be combined to measure the progression of mild cognitive impairment (MCI) and early Alzheimer's disease (AD). This work pulled data from phase 3 of the ADNI database (ADNI3) and screened specifically for participants with resting-state fMRI scans from multiple time points. There are 260 total participants in this dataset. Participants range in age from 56-92 years old at the age of scanning. Figure 3.1 shows the distributions of diagnosis and sex in the dataset. The majority of the diagnosed group has some form of MCI and not AD. Therefore, it is

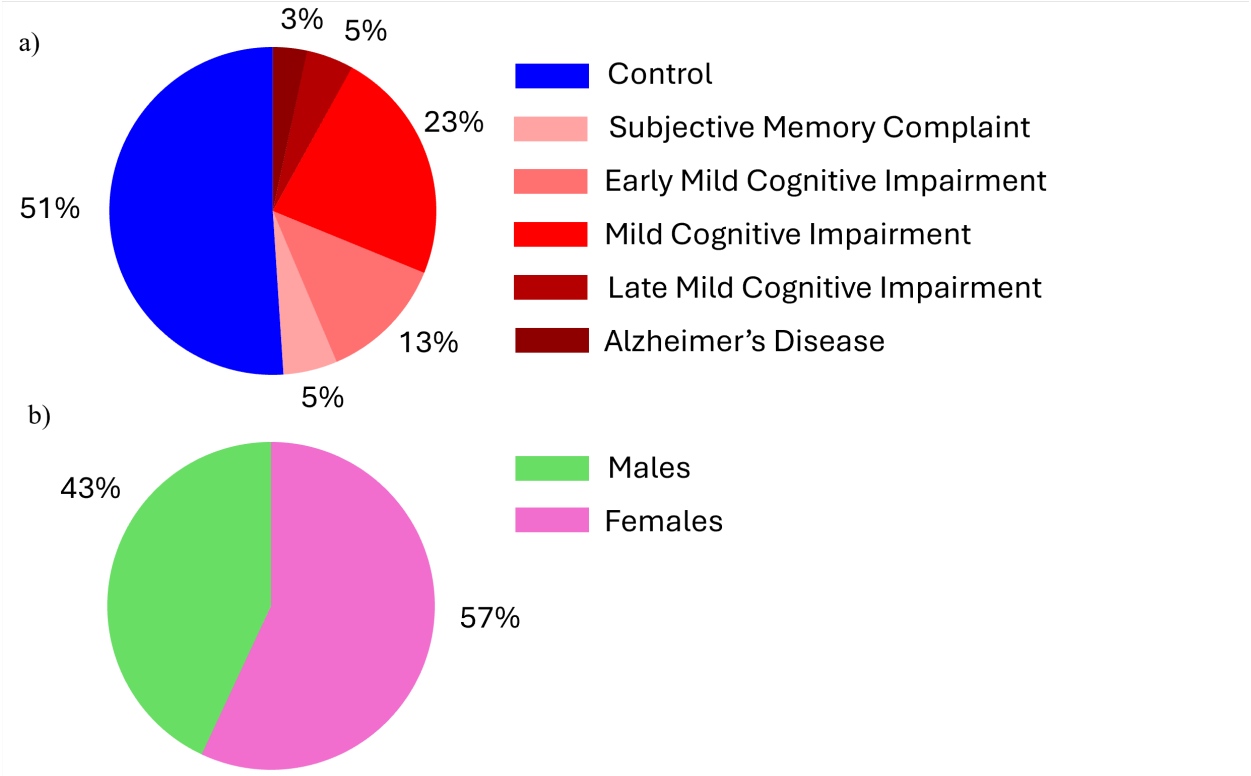

Figure 3.1: **Demographic distributions.** This graph shows the breakdown of the participants in the dataset based on diagnosis (a) and sex (b).

important to put most of the results of this study in the context on MCI.

It is important to note that throughout this work, we will be talking less about individual participants and more about time windows, i.e., pairs of consecutive scans. Participants all have at least one time window for fMRI. There are 421 fMRI time windows and 329 DTI time windows.

In order to create networks, the data from the scans had to be registered to an *atlas* of voxels belonging to specific brain regions. We selected Schaefer 2018 parcellation as the atlas for both the structural and functional images [Schaefer 2018]. The version of this atlas we selected has 100 regions and seven functional subnetworks. We chose to keep the atlas consistent across both types of images so they would remain fundamentally comparable. It is important to note that the Schaefer atlas is a functional atlas determined from clustering the resting-state fMRI scans of 1489 healthy adults [Schaefer 2018]. The labels for seven functional subnetworks that the atlas contains are canonical functional networks from Yeo et al. 2011 [Yeo 2011]. One label is ascribed to each node in the network. Nodes can only be a part of one subnetwork, and these subnetwork labels are fixed for all participants and time points. Figure 3.2 shows the subnetwork structure from the atlas. The seven subnetworks are the Visual Network (VN), the Dorsal Attention Network (DAN), the Salience Ventral Attention Network (SN), the Somatomotor Network (SMN), the Limbic Network

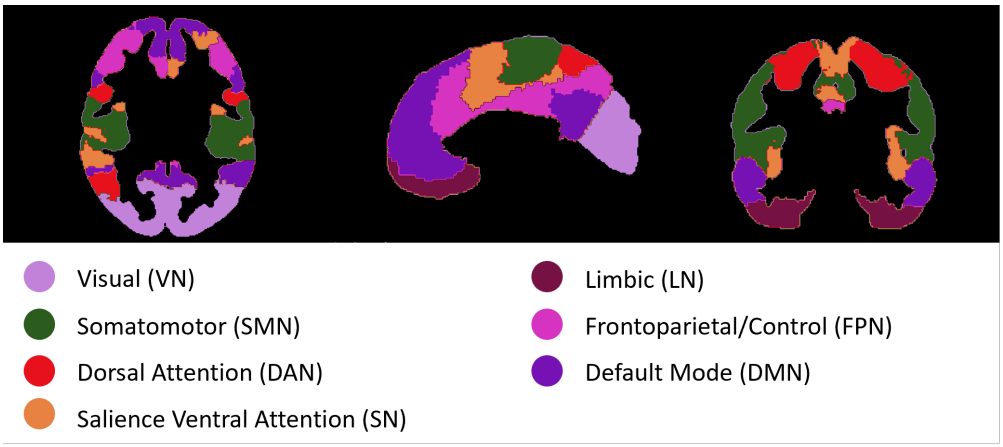

Figure 3.2: **Atlas subnetworks.** This shows axial, sagittal, and coronal slices of the Yeo et al. canonical subnetworks [Yeo 2011] on the Schaefer atlas [Schaefer 2018] for a sample participant.

(LN)[1], the Frontoparietal Networks (FPN) (sometimes called the Control Network), and the Default Mode Network (DMN). The next few sections will go over the preprocessing steps required to get the data in a usable form for network analysis.

3.2 Preprocessing and Network Formation

Preprocessing is an important step in using any MRI information. It takes the raw images and signals and corrects for known confounding variables and biases. This process involves spatial and temporal alignment, coregistration and atlasing, feature extraction, and signal filtering. The preprocessing steps in fMRI and DTI are distinct. In the next five sections, I will discuss these steps and their impact on the final signal, as well as describe how networks are formed from the preprocessed signal.

3.2.1 Anatomical MRI Preprocessing

The preprocessing of both fMRI and DTI images relies on high-resolution anatomical scans taken on the same day as the other scans to aid in the coregistration of the images. Recall that, in order to detect temporal information, of either oxygenated blood or water molecules, the echo planar sequence compromises on some of the spatial resolution. However, pairing these lower-resolution images with high-resolution anatomical scans provides greater spatial detail to the signals. The T1-weighted image is chosen for this anatomical image because of its strong contrast between grey and white matter in the brain.

These anatomical scans, as well as the fMRI images, were preprocessed with a procedure using the

[1]Throughout these analyses, the Limbic Network is consistently missing. This is due to this subnetwork only containing five nodes.

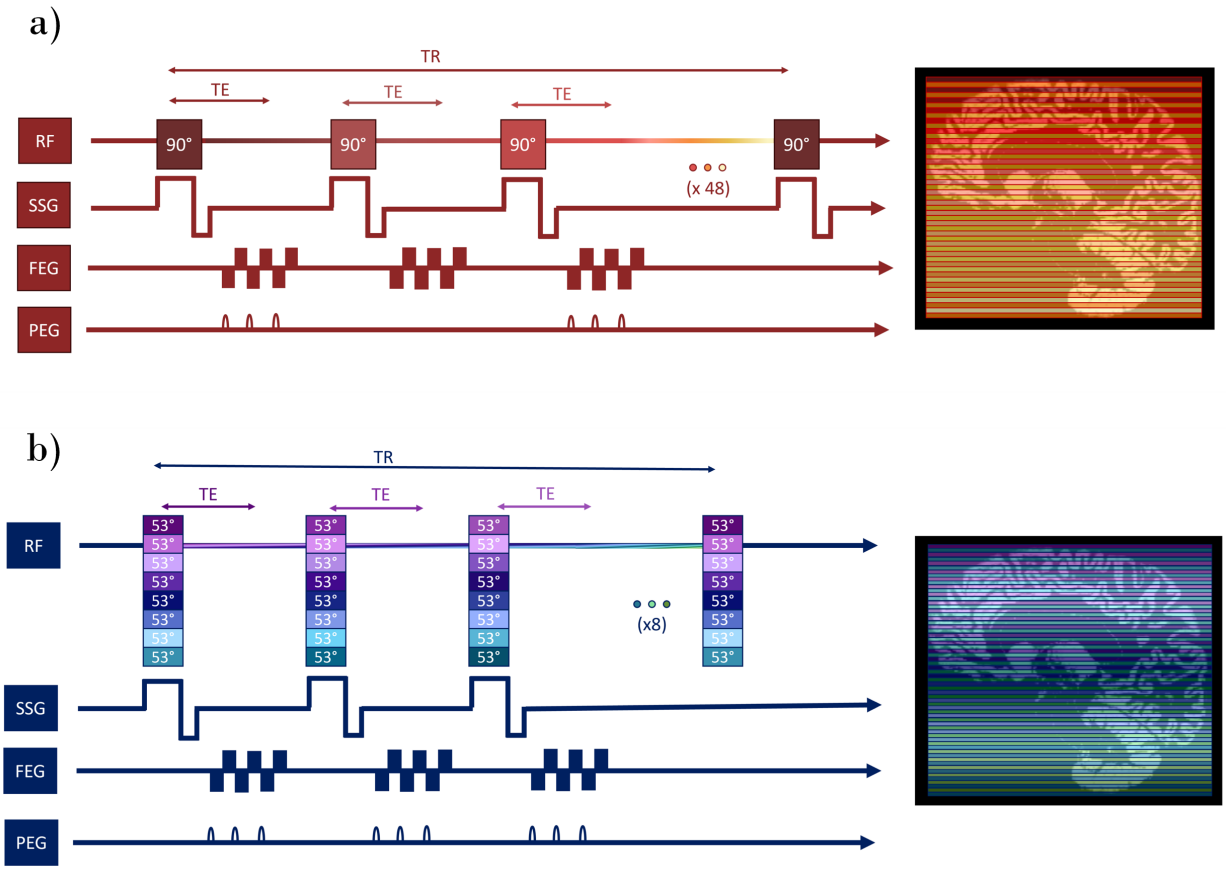

Figure 3.3: **Basic and multiband timing diagram.** Figure (a) shows the echo planar sequence for the basic fMRI scans from the dataset. Each 90° pulse represented on the radiofrequency pulse (RF) line is for a different slice of the total brain volume. For these scans, there are a total of 48 slices making up one volume, and the TR to scan the whole brain is 3000 ms. Figure (b) shows the echo planar sequence for the multiband fMRI scans from the dataset. Each 53° pulse represented on the radiofrequency pulse (RF) line is for a different slice of the total brain volume. For these scans, there are a total of 64 slices scanned with a multiband factor of 8, and the TR is 600 ms.

Statistical Parametric Mapping (SPM) software package (specifically SPM12) [Ashburner 2021]. The first step is to align the scan with a standard Tissue Probability Map (TPM), which is derived from a large number of brain images [Ashburner 2021]. This map is in a standard coordinate system used for brain mapping from the Montreal Neurological Institute (MNI). To align to the TPM, a series of affine translations prioritizing preserving rigid-body properties is conducted. This alignment process extracts the brain, removing unnecessary structures like the skull and neck. The scan is then processed to identify the grey and white matter probabilities for each voxel. Since the scan is now in MNI space and the grey matter has been identified, it can be mapped to the atlas, which is in the same coordinate system.

3.2.2 fMRI Preprocessing

The fMRI preprocessing involves several steps to correct and map the spatial and temporal information included in the scan. The first step requires the separation of each scan of the whole brain in the time series (these are often called volumes). Recall from Chapter 2 that the whole brain cannot be scanned all at once; for each volume in the time series, several slices of the brain along the z-axis are collected in sequence. This can be done in two different ways—the *basic scan* and the *multiband scan*. This dataset contains both types of scans, and they must be handled slightly differently.

Both types of scans use the echo planar sequence discussed in Chapter 2 (Figure 2.3). The protocols for the images in this dataset scan the whole brain in one period of TR. Figure 3.3a shows the basic scan, where only one slice is measured at a time, and Figure 3.3b shows the multiband scan, where eight slices are measured simultaneously. These sequences demonstrate the increased spatial and temporal resolution of the multiband scans. The basic scan has a $TR = 3000$ ms while the multiband scan has a $TR = 600$ ms. Thus, it is clear that the multiband scan has greater temporal resolution due to its shorter time to scan reducing the time between successive points in the time series. The multiband scan also has greater spatial resolution because the brain volume is split into 64 slices rather than 48 slices. Finally, and important to our discussion of preprocessing, the multiband scan has a longer timeseries as both scan are 10 minutes in total length and the greater spatial resolution does not detract from the temporal resolution gains from parallelization. Understanding these types of scans is important for understanding the rest of the preprocessing that was conducted.

After separating out the series of frames, a motion correction is conducted where each frame is matched to the orientation of the first frame (Figure 3.4a). Translational and rotational adjustments are made to align the frames through SPM's spatial reslicing (`spm_reslice`) [Ashburner 2021]. The next step is the slice timing correction which utilizes the pattern of the slices being scanned during one TR period (Figure 3.3a)

to adjust the timing of each slice to accurately reflect the difference when the TR period becomes a single time point in the time series[2] using SPM's slice-timing correction (`spm_slice_timing`) [Ashburner 2021] as seen in Figure 3.4b.

Following those two corrections, all frames of the image are coregistered with the anatomical $T1$ image. As previously stated, this allows for some gains in the spatial resolution that are lost through the echo planar sequence's time saving techniques. Coregistration requires the resampling of the T1-weighted image using SPM's B-spline interpolation functions (`spm_bsplins` and `spm_bsplinc`) [Ashburner 2021]. Then, using SPM's normalized mutual information coregistration (`spm.spatial.coreg.estwrite`) [Ashburner 2021], the image is registered with the anatomical image (Figure 3.4c), following the same techniques as the motion correction.

Next, the signal for each voxel is corrected from global trends in the data through the Linear Model of the Global Signal (LMGS) method using a tool from Paul Macey (`cspm_lmgs`) [Macey 2004]. This correction is not about small signal fluctuations, which are informative, but about long-term trends across the entire time series and affecting all voxels. In Figure 3.4d, we can see the global signal (in blue) and the global signal after the voxels are adjusted for that global trend (in red).

The resulting signals are then mapped to the selected atlas, and the signal for each region is calculated. This signal is calculated through a grey matter weighted average signal,

$$S_r(t) = \frac{\sum_{v \in r} GM_v(t) \cdot VS_v(t)}{\sum_{v \in r} GM_v(t)} \tag{3.1}$$

where $GM_v(t)$ is the grey-matter probability for the voxel v at time point t and $VS_v(t)$ is the voxel signal for voxel v at time t. These sums are calculated over all voxels in region r. This leaves a calculated time series for each of the 100 regions in the atlas. The grey matter weighting is to ensure, even beyond coregistration, that the signal is calculated for grey matter regions of the brain and not for other regions like white matter or skull [Carbonell 2011]. This grey matter probability is pulled from the T1-weighted anatomical image.

The last step in the preprocessing before we can start building the networks is to filter the frequencies using a band pass filter using the Signal Processing Toolbox MATLAB function `bandpass` [The MathWorks, Inc. 2023]. This applies both a low- and high-pass filter on the signal. The high-pass filter removes frequencies that are below 0.01 Hz, which is done to remove fluctuations in the equipment or slow, unrelated physiological processes. In this way, it extends the filtering conducted by the detrending. The low-pass filter removes frequencies that are above 0.08 Hz. This filter removes known confounding frequencies like breathing and

[2]There is some debate on the efficacy of this preprocessing step, especially when it comes to multiband scans which already have a shortened TR [Sladky 2011, Wu 2011, Parker 2019]. Additionally, when this preprocessing was conducted, the pattern of slice scanning for the basic scan was inaccurately entered as sequential rather than interwoven. This issue does not appear to have significantly impacted the resulting networks.

heartrate, which may conflict with the brain signals that we want to measure. Frequency filtering utilizes the known frequency ranges of brain activity to filter out frequencies that are unlikely to represent the actual brain signal [Nieto-Castanon 2020]. The signal before and after filtering for 5 example regions is shown in Figure 3.4f.

3.2.3 fMRI Network Formation

Once the fMRI signal has been preprocessed, the resulting data is a time series for each of the 100 regions in the atlas. In order to form a network from this information, the time series are correlated using the Pearson correlation and creating a correlation matrix. Recall that the basic and mutiband scans have different lengths of time series. In both of these cases, the entire time series was correlated. As the time series for each region in one scan is the same length, correlation is possible; the difference is between scans.

The types of models used in this project require binarized networks due to their mechanism of building or dissolving connections. Thus, some threshold of binarization, grounded in literature balancing over and under connectivity and the preservation of key network structures [Borchardt 2016, Garrison 2015], must be selected for these networks. We selected a threshold that produces networks with a 20% density [Borchardt 2016, Garrison 2015]. This was done regardless of the positive or negative weight of the value, meaning that negative weights were removed. There is some debate on this topic in the literature [Liu 2017, Murphy 2017], but we determined that for this initial study of this model-building methodology, ignoring negative weights was a reasonable choice. Figure 3.4g shows the matrices for one example scan.

Once the matrix is binarized, a network can be formed. The nodes in this network represent brain regions, and the edges in this network represent the strongest 20% of connections. There are 100 nodes ($N = 100$) and about 990 edges ($M \approx 990$). These networks are undirected and unweighted. Figure 3.4h shows an example of the network as represented on a standard brain. The next few sections will discuss the preprocessing and network formation of the structural (DTI) images.

3.2.4 DTI Preprocessing

The DTI preprocessing procedure is a similar procedure to the fMRI preprocessing procedure, with a few unique steps. DTI preprocessing was conducted using FMRIB Software Library (FSL) [Woolrich 2009, Smith 2004] and MRtrix3 [Tournier 2019]. The steps follow closely the tutorial from Andy Jahn [Jahn 2022].

The first step in DTI preprocessing is noise correction using Marchenko-Pastur PCA through the MRtrix3 denoise function (`dwidenoise`) [Tournier 2019] and a Gibbs artifact correction through the MRtrix3 degibbs function (`mrdegibbs`) [Tournier 2019]. The first row of Figure 3.5a is a frame from the original images,

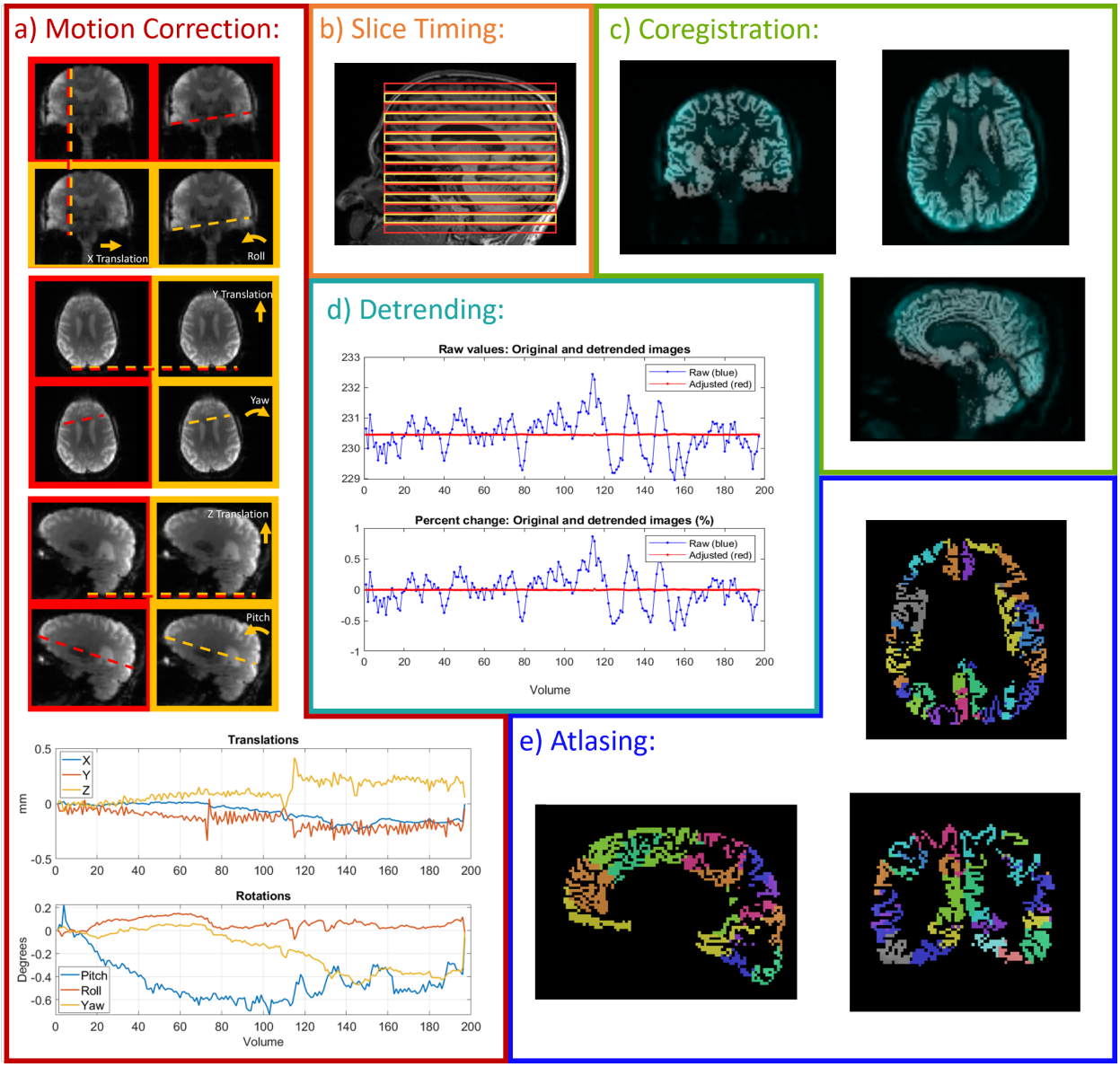

Caption for this image is on the following page.

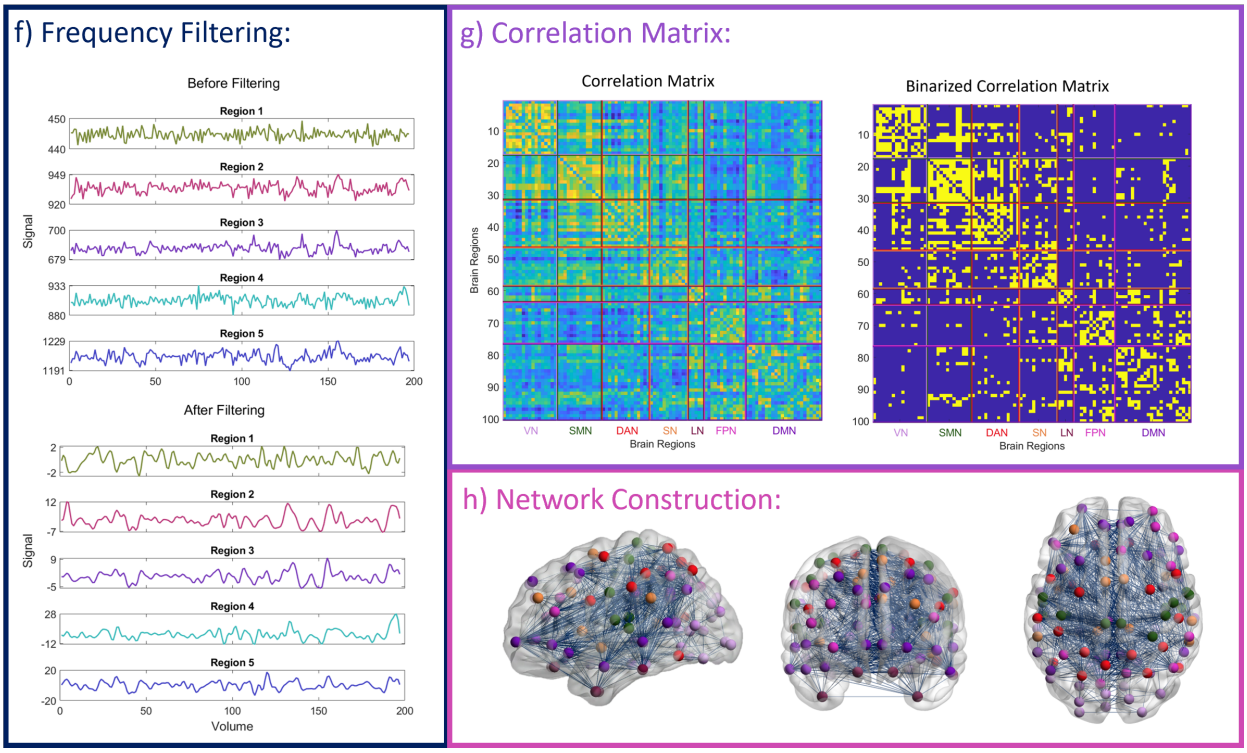

Figure 3.4: **fMRI preprocessing.** This schematic shows the preprocessing steps for the fMRI data. The images and graphs were produced from a single participant and a single scan in the dataset as an example. This was a basic (not multiband) scan. Figure (a) shows the motion correction, including sample images and the graphs on the types of motion correction done for each volume in the time series. Figure (b) demonstrates the slice timing correction pattern. Figure (c) shows the coregistration of the first fMRI volume with the original T1-weighted image. Figure (d) shows the detrending correction as produced by the detrending function. Figure (e) shows the atlas applied to this specific brain. Figure (f) shows five sample regions before and after frequency filtering. Figure (g) is the original correlation matrix (left) and the binarized correlation matrix (right). The scale for the original matrix is from -1 to 1. These matrices are symmetric with size 100x100. The labels on the x-axis show the canonical subnetworks. Figure (h) shows the full binarized brain network for this participant, with the colors on the nodes representing the different subnetworks. Figure (h) was produced with BrainNet Viewer [Xia 2013].

and the second row shows the same frame after the correction. Gibbs artifacts are a consequence of the Fourier transform from the signal collection around TE. In high-contrast areas, the number of phase-encoding gradients can create ring-like artifacts in the image [Veraart 2016]. No particular Gibbs artifacts were found in this scan, though these effects may be visually subtle. The Gibbs correction is not included in fMRI preprocessing because of the lower spatial resolution and the dominance of other kinds of noise [Veraart 2016, Power 2015]. The second step in the DTI preprocessing is a motion correction that aligns all frames with the first frame of the scan (Figure 3.5b). Recall that DTI, similar to fMRI, has a temporal component in order to track the motion of water in the brain; thus, a motion correction is a necessary step. The motion correction follows the same kinds of translations to align all frames with the first frame as with fMRI; however, this time FSl's eddy tool was utilized (`dwifslpreproc`) [Woolrich 2009, Smith 2004]. The next step in the preprocessing procedure is a correction for bias (Figure 3.5c), which corrects for machinery inhomogeneities. The MRtrix3 function `dwibiascorrect` performs a B1 field inhomogeneity correction using the N4 algorithm provided by Advanced Normalizations Tools (ANTs) [Avants 2011, Tournier 2019].

The next step is to estimate the fiber directions from the diffusion information using a process called constrained spherical deconvolution. This begins with estimations of the white matter, grey matter, and cerebrospinal fluid response functions using MRtrix3's response function estimation tool with the Dhollander method (`dwi2response dhollander`) [Dhollander 2016, Tournier 2019]. This is followed by the deconvolution using MRtrix3's fibre orientation distribution function (`dwi2fod msmt_csd`) [Jeurissen 2014, Tournier 2019]. A sample of the fiber orientation distribution is shown in Figure 3.5d. This is the step that collapses the information from all the frames of the DTI scan into a voxel-wise representation of the diffusion information.

The next step in this process is to coregister with the $T1$-weighted anatomical image (Figure 3.5e). This procedure is run with the raw anatomical image to apply the specific tissue boundary extraction to distinguish the types of brain tissue using FSL tools (`5ttgen fsl`) and to coregister with the anatomical image using FSL's function `flirt` to perform the rigid-body alignment and nearest-neighbor interpolation [Woolrich 2009, Smith 2004]. With the fiber orientation distribution and the known white and grey matter tissue, it is possible to determine the streamlines across the axon-dense white matter of the brain from grey matter regions to grey matter regions. This was conducted through anatomically-constrained tractography and refined to prevent overfitting through MRtrix3's streamlines generation and refinement tools (`tckgen`, `tckedit`, and `tckshift2`) [Smith 2012, Tournier 2019]. One participant's example streamlines are shown in Figure 3.5f.

The final step in the DTI preprocessing procedure before network formation is applying the atlas to the streamlines image and to calculate the connectome using the MRtrix3's connectome generation tool

(`tck2connectome`) [Tournier 2019]. As stated, we used the same atlas for the structural data as we did for the functional data [Schaefer 2018].

3.2.5 DTI Network Formation

As a result of the preprocessing procedure, the number of streamlines between the 100 regions of the atlas can be determined. This gives us the first connectome matrix in Figure 3.5h. In the same way as the functional correlation matrix, a 20% density threshold was then applied to the original connectome to create a binarized connectome. This is the second matrix in image 3.5h. These binarized connectomes represent the structural networks utilized in this project, and one example network is show in Figure 3.5i using the BrainNet Viewer software [Xia 2013]. The structural networks created from the DTI images are undirected and unweighted with 100 nodes ($N = 100$) and about 990 connections ($M \approx 990$). These were designed to be comparable to the fMRI networks.

3.3 Conclusion

This chapter walked through the dataset acquisition and preprocessing to create the functional and structural networks that are utilized in this project. Drawing from fMRI and DTI networks in the ADNI dataset, consecutive networks are paired to create the longitudinal time windows that will be used to investigate the stochastic actor-oriented models (SAOMs) of aging brain networks. The next two chapters will cover the SAOM framework and the model derivation procedure.

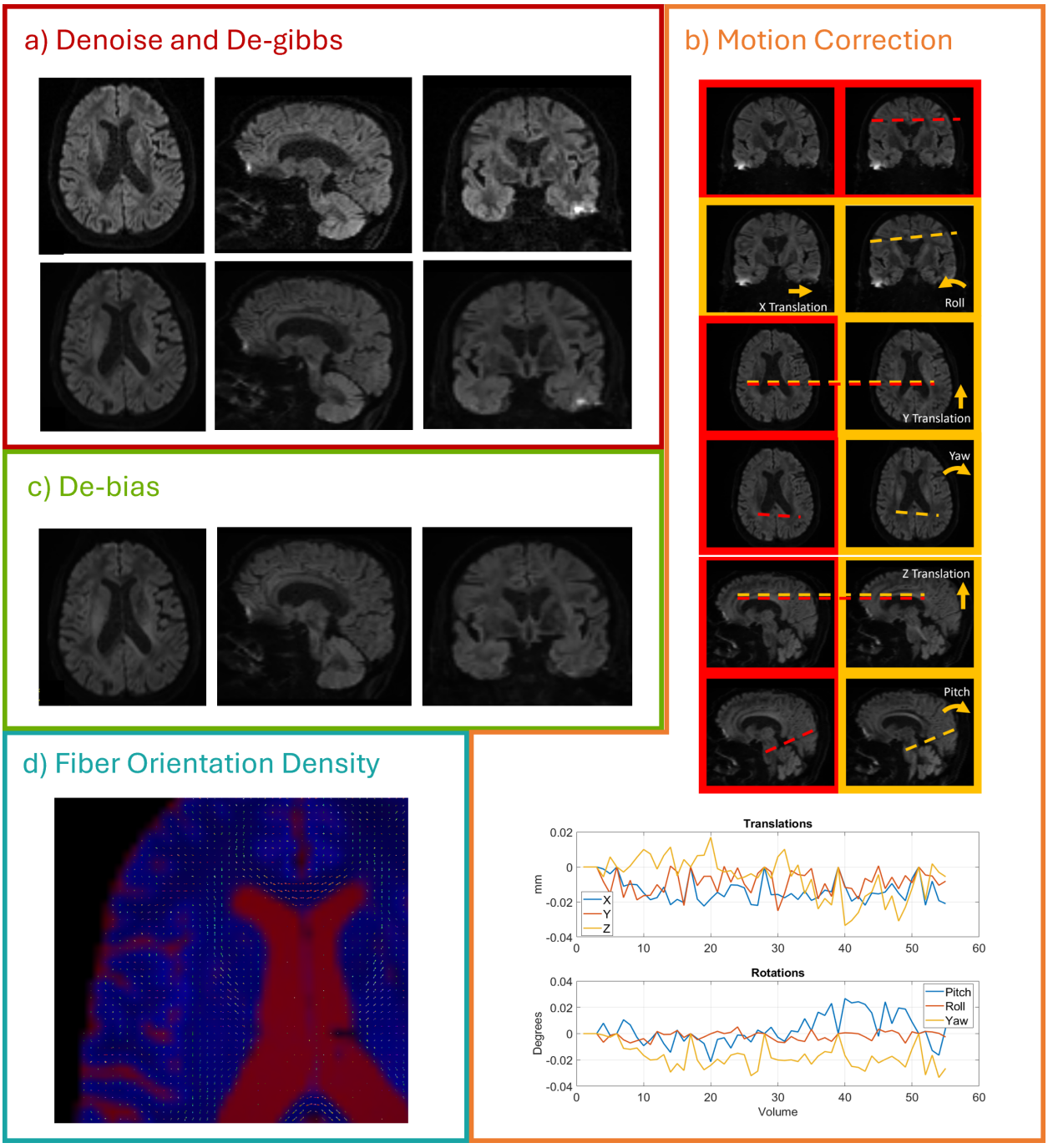

Caption for this image is on the following page.

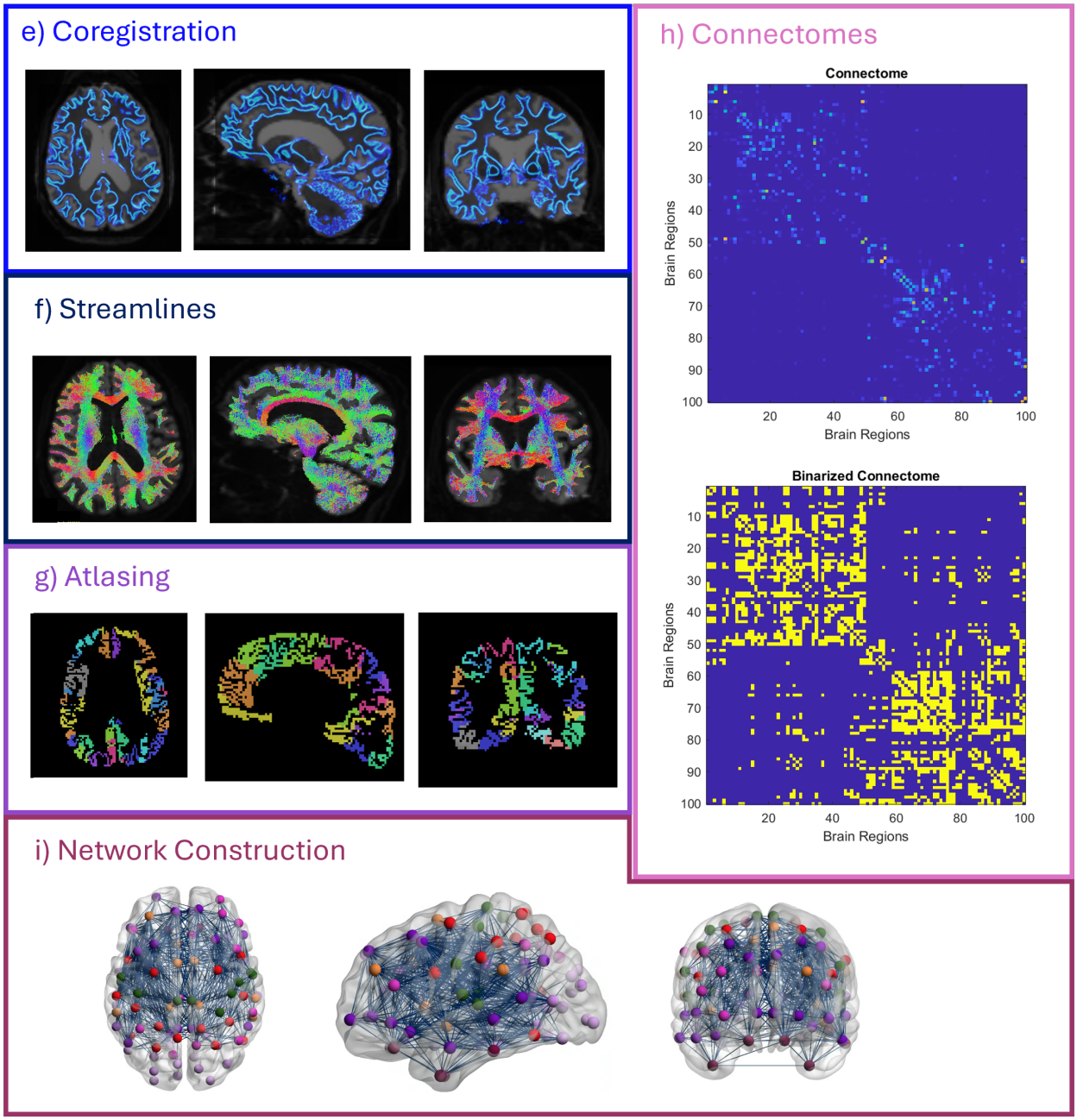

Figure 3.5: **DTI preprocessing.** This schematic shows the preprocessing steps for the DTI data. The images and graphs were produced from a single participant and a single scan from the dataset as an example. Figure (a) shows the correction for noise and Gibbs artifacts across volume points (only one volume is shown). Figure (b) shows the motion correction. Figure (c) shows the correction for bias. Figure (d) shows a single zoomed-in image where the fiber orientation is found for each voxel in the image. The small marks show the direction detected for that voxel. Figure (e) shows the coregistration with the T1-weighted anatomical image. Figure (f) shows the streamlines as found through the tractography algorithm. Figure (g) maps the scan to the selected atlas. Figure (h) is the original connectome matrix (top) and the binarized connectome matrix (bottom). The scale for the original matrix is from 0 to 13. These matrices are symmetric with size 100x100. The first 50 regions are located in the right hemisphere, and the second 50 regions are located in the left hemisphere. Figure (i) shows the full binarized brain network for this participant, with the colors on the nodes representing the different subnetworks. Figure (i) was created using BrainNet Viewer [Xia 2013].

Chapter 4

Methods: Stochastic Actor-Oriented Model

This project, endeavoring to answer the question of how brain networks change over time, requires a framework of these dynamics. We have chosen to apply the stochastic actor-oriented model (SAOM), which was originally designed for describing how social networks change over time. In the application of this model, we chose to utilize the existing infrastructure, specifically, the R-based Simulation Investigation for Empirical Network Analysis (RSiena) designed for the implementation of the SAOM. This choice provides the tools of implementation and handles many challenges to that implementation. However, it also limits the specificity of the application to brain networks and places specific and important limitations on the results. Future work will likely require expanding the use of RSiena or creating an alternate implementation of the model framework.

This project will apply the methods from the next two chapters to the functional networks, the structural networks, and the functional and structural subnetworks individually. Thus, the result will not be a single model of network change but a group of models that can be analyzed for their interplay and significance to questions about aging and dementia.

This chapter will go over first the framework of the model and then the definitions of potential factors in the model. Much of the information about the internal procedures of Rsiena is pulled from the Rsiena Manual [Snijders 2024]. However, the mathematical definitions and general nomenclature utilized here will differ from other implementations of the SAOM due to this specific application.

4.1 Model Framework

The stochastic actor-oriented model (SAOM) is a model of network change across longitudinal time points. The model has several options and features that can be selected as they apply to various types of networks. I will mostly limit my discussions here to those features that are relevant to our work in this area and our unique application of the model. Thus, this section should not be taken as a comprehensive guide on the SAOM.

The SAOM, as we are utilizing it, has two main functions that describe change on networks. The first is the *rate function* and the second is the *objective function*[1]. The rate function controls the rate at which the network (and individual nodes) change, while the objective function controls the probability of particular changes from the perspective of individual nodes.

These two functions work together to determine the pattern of changes between time point one (t_1) and time point two (t_2) by splitting the time into mini time steps of a length pulled from an exponential distribution. In each mini time step, one node is selected to have the opportunity to change. Then, the objective function provides the probability of that node making particular changes based on particular model factors. A change to a connection of this node is made based on this probability, and the process is repeated until t_2 is reached.

This chapter will go into more detail about how the model works when it has its factors and factor weights, while the following chapter will describe how the factors and factor weights are derived from data. The goal, in this project, is to develop and analyze models of network change for functional and structural brain networks in aging. These models will be of the framework of the SAOM, which is why it is important to understand the model framework. In future chapters, I will refer to "models" as those equations developed from data, rather than model referring to the overall framework (despite the SAOM framework having model in its name).

4.1.1 Rate Function

Time handling in the stochastic actor-oriented model is based on the continuous-time Markov chain and mini time steps during which one node has the opportunity to change. In Chapter 2, we discussed the continuous-time Markov chain and how it can describe the probability of transition between various states in continuous time. Here, we will discuss how this is applied to the SAOM.

Recall that the continuous-time Markov chain describes a memoryless process of transitioning between various states in continuous time. It may be split into the holding-time distribution (Equation 2.11) and the

[1]The objective function, in the literature, is sometimes called the evaluation function.

jump-chain probability (Equation 2.14) describing the distribution of time between changes of state and the probabilities of particular changes in state, respectively. In this model, the various states referred to by the continuous-time Markov chain are the nodes given the opportunity to change at a particular time and not the chages that are made by those nodes. In the rate function, states are nodes.

The SAOM keeps the probability of transitioning to particular states independent of the previous state. In other words, the next node to be selected is not impacted by the previous node that was selected. This means that the node that was most recently selected may be selected again as a distinct procedure from the time that you hold with that node (stay in that state).

This may be conceptually distinct from the traditional continuous-time Markov chain, but it can be incorporated mathematically fairly simply. Equation 2.11, the cumulative holding-time distribution, shows the exponent to have a coefficient that is the negative sum of the rates for all the states it is possible to transition to when in *state a* ($-\lambda_{ab} - \lambda_{ac}$, for a system with 3 states). Since it is possible to transition from *state a* to *state a*, this would instead be the negative sum of the rates for all possible states (nodes).

$$P(t) = 1 - \exp(-t \sum_{i}^{N} \lambda_i) \tag{4.1}$$

where N is the number of nodes in the network and λ_i is the rate function for node i.

Similarly, the denominator for the jump-chain probability, Equation 2.14, is the sum of the rates for all the states it is possible to transition to when in *state a*, and would thus be the sum of all the rates when applied here. The numerator for J_{ab} is the rate for the transition between *state a* and *state b*. In the SAOM, the rate for the transition to *state b* is the same regardless of the state from which we are transitioning. Thus, instead of having a rate for each transition in a matrix, this model has one rate for each node (λ_i). This gives the jump-chain probability of transitioning to any state (j) as,

$$J_j = \frac{\lambda_j}{\sum_i^N \lambda_i} \tag{4.2}$$

In our models, however, all the nodes are equally likely to be selected. They all have the same *base rate* (ρ) which determines the average number of times that node will be selected to have the opportunity to change between t_1 and t_2.

$$\lambda_i = \rho \tag{4.3}$$

This was a simplification that we felt was important in this preliminary implementation of the SAOM on brain networks because of the complexity of the factors in the objective function. Future research might consider including rate related factors, as this framework is capable of accommodating rate related factors

by having λ_i contain a linear combination of factors ($\lambda_i = \rho \sum_j \alpha_j k_j$).

In each mini time step, one node is selected to have the opportunity to change based on the jump-chain probability (Equation 4.2) and a certain amount of time passes drawn from the exponential distribution indicated by the holding-time distribution (Equation 4.1). Mini time steps are conducted until the cumulative time that passes exceeds 1, which is the amount of time between t_1 and t_2.

4.1.2 Objective Function

The SAOM does not simply describe how much change is occurring on the network, but also describes the direction of that change. As the name implies, the model is actor-oriented. In the original version, all the nodes in the network were people or *actors*. In my application, it is more accurate to say that the framework is node-oriented. It describes the direction of change on a network on an individual node level. In the model, large-scale behavior emerges from the actions on the node level. Furthermore, the language used here will mirror that used in other descriptions of the SAOM. It is important to acknowledge, however, that in my application, the language is a personification of nodes that are brain regions.

The objective function describes the direction of particular changes in the framework. Through the rate function, a particular node is chosen to have the opportunity to change; the particular change that is made is based on how satisfied the node is with the particular arrangement of its connections. Calculating and applying this satisfaction is the purpose of the objective function.

The objective function (f_i) takes the form of a linear combination of factors—these are generally network features, but can also be features of the individual nodes (Section 4.2).

$$f_i(\boldsymbol{x}(i \rightsquigarrow j)) = \sum_k \beta_k s_{ik}(\boldsymbol{x}(i \rightsquigarrow j)) \tag{4.4}$$

where $\boldsymbol{x}(i \rightsquigarrow j)$ is the network when the connection between node i and node j is changed. If node i is not connected with node j, a connection is formed, and if node i is connected with node j, the connection is dissolved. β_k is the weight of factor k and s_{ik} is the formula for factor k calculated for node i. The values of β can be positive or negative—where positive values indicate a positive priority on that factor, while negative values indicate a negative priority on that factor.

Each factor does not have the same scale in its calculated value. For example, Factor Degree ($D_i = \sum_j \boldsymbol{x}_{ij}$) is calculated as the degree of node i which is scaled as $[0, N-1]$. On the other hand, Factor Transitive Triads ($T_i = \sum_{j<h} \sum_h \boldsymbol{x}_{ij}\boldsymbol{x}_{ih}\boldsymbol{x}_{jh}$) calculates the number of triangles to which node i belongs. This is scaled as $[0, (N-2)(N-1)]$. The scales of various factors may also be non-linear. As a result, the weights (β) for each factor are scaled differently and cannot be compared directly. A $\beta_1 = 0.5$ for Factor

Degree and a $\beta_2 = 0.5$ for Factor Transitive Triads do not mean that these factors are prioritized the same amount. Individual nodes are impacted by factors not only based on the values of β, but also on the node's local connectivity. These scaling differences will be important to keep in mind when considering the values of β in the results. Normalizing these factors is complicated and not particularly effective because the weights of the priorities are highly dependent on that underlying network structure of the data. Normalizing is not included in the Rsiena implementation. Future research may explore what normalization would look like for these types of models, but would likely require an independent implementation. Thus, in the interpretation, we makean effort to account for this sensitivity and these differing scales.

4.1.3 Model Operation

The first step in understanding the SAOM framework is to understand how it operates when both the rate and the objective function are known. As we know from the rate function, the procedure is split into mini time steps pulled from the exponential distribution, where one node is given the opportunity to change. The goal is to consider which changes to that node would improve its satisfaction based on the objective function. Thus, each possible change that the chosen node can make is considered, and the objective function is solved for those changes.

$f_i(\boldsymbol{x}(i \rightsquigarrow j))$ would be the objective function when node i is given the opportunity to change and is considering a change to node j. The network $\boldsymbol{x}(i \rightsquigarrow j)$ in that equation would not be the current network, but the network that would exist if node i chose to change its current connection with node j. Change here can refer to either building or dissolving that connection. The model can also accommodate node i choosing not to make a change given the opportunity. The objective function, in this scenario, is $f_i(\boldsymbol{x}(i \rightsquigarrow i))$ and the network $\boldsymbol{x}(i \rightsquigarrow i)$ is the current network.

Once the objective function is calculated for each possible change that node i can make, the probability of making each change can be calculated. The probability equation follows this format, where $p_i(\boldsymbol{x}(i \rightsquigarrow j))$ is the probability of node i changing its connection with node j.

$$p_i(\boldsymbol{x}(i \rightsquigarrow j)) = \frac{\exp f_i(\boldsymbol{x}(i \rightsquigarrow j))}{\sum_h^N \exp f_i(\boldsymbol{x}(i \rightsquigarrow h))} \tag{4.5}$$

The sum of the probabilities for each change (and the choice not to change) will be 1, and the number of possible choices is the number of nodes in the network, N.

One of the choices is then selected based on the calculated probabilities, and that change is made to the network. This concludes that mini time step and, if the time limit has not been reached ($t + \Delta t \leq 1$), a new mini time step begins with the selecting of a node.

Factor	Symbol
Degree	D
Transitive Triads	T
Betweenness	B
Distance 2	$D2$
4-Cycles	$C4$
Assortativity	A
Physical Distance	PD
Physical Neighbor Distance	ND
Same Subnetwork	S
Same Subnetwork Transitive Triplets	ST
Jump Subnetwork Transitive Triplets	JT
Same Subnetwork Distance 2	$S2$
Same Subnetwork 4-Cycles	$S4$

Table 4.1: **Potential factors.** This table shows the potential factors that were used in the hypothesis-building procedure. Not all factors are included in the final models. The symbols are used throughout the results to represent that particular factor.

As the procedure continues, changes are made throughout the network. Recall that our base rate, ρ, tells us the average number of opportunities that each node will have to change. So, if $\rho = 5$ and $N = 100$, there are going to be about 500 opportunities to change during the time between t_1 and t_2. These opportunities only allow the chosen node to make one change based on the priorities; thus, changes during mini time steps are subtle, while emergent properties and trends may appear over the entire time window. As a result, this model can tell us something more about the dynamics of changes in brain networks across the lifetime rather than just observing trends.

The SAOM operates in the following procedure:

1. Check if the current time, t, (begins at zero) is less than the final time, $t \leq 1$. If no, exit procedure.
2. Select a node in accordance with the jump-chain probability based on the rate function (Equation 4.2).
3. Calculate the probability for each change the selected node can make (including no change) based on the objective function (Equation 4.5).
4. Select a change based on those probabilities and update the network, $\boldsymbol{x}$, accordingly.
5. Update the current time, $t = t + \Delta t$, by adding a time (Δt) from the exponential distribution (Equation 4.1)
6. Repeat steps 1-5 until the current time, t, surpasses the final time, $t > 1$.

4.2 Factor Definitions

This section will describe the mathematical definitions of all the factors relevant to undirected networks, as well as their independent interpretation. Table 4.1 shows the factors that were included as possibilities in this implementation, as well as their symbol that is used in the rest of this work. Future research should expand this list of factors and generate new factors with implementation specific priorities.

The equations are compiled from the Rsiena manual [Snijders 2024]. Mathematical detail has been added to most. Some equations have been changed, not in meaning, but for clarity and consistency of format in so far as that is possible. Recall that the factor equations describe the relative value of changes made by a single node at a time. This is why the factor definitions describe the feature based on a single node (i).

$\boldsymbol{x}_{ij}$ describes the presence or absence of a connection between node i and node j. As all the networks in this study are undirected, the order of the i and j is irrelevant. These equations are meant to reflect the undirected nature of the networks utilized here and should not be taken to describe these factors when applied to directed networks.

4.2.1 Whole Network Factors

Factor Degree

Factor Degree describes the number of nodes to which node i is connected and can be described mathematically as,

$$D_i = \sum_{j}^{N} \boldsymbol{x}_{ij} \tag{4.6}$$

With a positive weight, this factor would prioritize node i making more connections.

Factor Transitive Triads

Factor Transitive Triads describes the number of triangles to which node i belongs and can be described mathematically as,

$$T_i = \sum_{j<h}^{N-1} \sum_{h}^{N} \boldsymbol{x}_{ij} \boldsymbol{x}_{ih} \boldsymbol{x}_{jh} \tag{4.7}$$

With a positive weight, this factor would prioritize node i making more triangles.

Factor Betweenness

Factor Betweenness describes the number of nodes in unconnected pairs to which node i is connected and can be mathematically represented as,

$$B_i = \sum_{j}^{N} \sum_{h}^{N} \boldsymbol{x}_{hi} \boldsymbol{x}_{ij} \left(1 - \boldsymbol{x}_{hj}\right) \tag{4.8}$$

Unlike Factor Transitive Triads, this factor has not been adjusted for the undirected nature of the network. This leads to this factor counting nodes rather than pairs of nodes. If node A is connected to node B and node C while node B and node C are unconnected, the value for Factor Betweenness would be 2, not 1. This mostly affects the scaling of this factor, which serves as a reminder that the estimated weights do not have consistent scaling. Additionally, this factor is not normalized for the degree of the node, giving it an inadvertent prioritization of higher degree. This is important to note when this factor (and others) appear without Factor Degree.

With a positive weight, this factor would prioritize node i connecting with nodes unconnected to its neighbors.

Factor Distance 2

Factor Distance 2 describes the number of nodes to which node i is connected not directly, but at a path length of two, and can be mathematically described as,

$$D2_i = \sum_{j}^{N} \left(1 - \boldsymbol{x}_{ij}\right) \max_{h} \left(\boldsymbol{x}_{ih} \boldsymbol{x}_{hj}\right) \tag{4.9}$$

With a positive weight, this factor would prioritize node i connecting with nodes that are connected to nodes to which node i is not connected or disconnecting from nodes that are already connected at a path length of two. This is a factor that prioritizes a less densely connected neighborhood, but not a disconnected neighborhood.

Factor 4-Cycles

Factor 4-Cycles describes the number of 4-cycles (number of rectangles) to which node i belongs divided by two and can be mathematically described as,

$$C4_i = \frac{1}{4} \sum_{j}^{N} \sum_{k \neq j}^{N} \sum_{h \neq j \neq k}^{N} \boldsymbol{x}_{ij} \boldsymbol{x}_{ik} \boldsymbol{x}_{hj} \boldsymbol{x}_{hk} \tag{4.10}$$

This factor calculates the number of 4-cycles but will always double count based on node j and k being equivalent. This value is then divided by four, which leads us to the number of 4-cycles divided by two.

With a positive weight, this factor would prioritize node i completing 4-cycles.

Factor Assortativity

Factor Assortativity describes the general popularity of node i and the popularity of nodes to which node i is connected and can be mathematically described as,

$$A_i = \sum_j^N \boldsymbol{x}_{ij} \left(\sum_h^N \boldsymbol{x}_{ih} \right)^{1/2} \left(\sum_k^N \boldsymbol{x}_{jk} \right)^{1/2} \tag{4.11}$$

With a positive weight, this factor would prioritize node i, making connections with nodes that have a higher degree, though more significantly if node i has a high degree.

Similar to previous factors, this factor has an inadvertent priority on making more connections as well. It does not, as the name assortativity implies, demonstrate the priority of connecting similar degree nodes with each other, but the priority of connecting high-degree nodes with other high-degree nodes.

4.2.2 Physical Distance Related Factors

The whole network factors concern the underlying network structure. In addition to these variables, the Euclidean distance between nodes in the brain is known from the atlas and allows for the inclusion of factors related to this distance. The physical distance between nodes does not change between time points nor does it differ between participants, as it is a euclidean distance calculated in MNI space. This section includes the factors related to physical distance that are included as options. In these factors, $\boldsymbol{w}_{ij}$ is the physical distance between node i and node j.

Factor Physical Distance

Factor Physical Distance sums the number of nodes to which node i is connected scaled by the physical distance between node i and those nodes minus the average distance of all nodes from node i and can be described mathematically as,

$$PD_i = \sum_j^N \boldsymbol{x}_{ij} (\boldsymbol{w}_{ij} - \sum_h^N \boldsymbol{w}_{ih}) \tag{4.12}$$

The centering based on node i's average distance can lead this factor to be both a positive priority and a negative priority regardless of the sign of its weight, due to the calculation being able to be negative.

With a positive weight, this factor would prioritize node i connecting with nodes that are closer than the average distance and disconnecting from nodes that are further than the average distance.

Factor Physical Neighbor Distance

Factor Physical Neighbor Distance sums the number of nodes to which node i is connected scaled by the physical distance between those nodes and the other nodes to which node i is connected and can be described mathematically as,

$$ND_i = \sum_{j}^{N} \sum_{h \neq j}^{N} \boldsymbol{x}_{ij} \boldsymbol{x}_{ih} \boldsymbol{w}_{hj} \tag{4.13}$$

With a positive weight, this factor would prioritize node i connecting with nodes that are far away from the nodes to which node i is connected.

4.2.3 Subnetwork Interaction Factors

Recall, also, that the networks studied here are split into seven subnetworks with different structures and functions. We used these subnetwork labels in some of the included factors. The seven subnetworks are immutable during the network change process, and all networks, though containing different connections, have the same subnetwork labels. Changing these subnetworks during each mini time step would be computationally expensive. All the subnetworks are mathematically equivalent. This means that a subnetwork labeled 1 is different than, but not less than, on any scale, a subnetwork labeled 2. Thus, the factors were selected based on this fact and include only binary values (same or different) rather than scaled values. v_i is the subnetwork value of node i and, in this case, describes to which subnetwork node i belongs. Further, $[v_i = v_j]$ uses Iverson brackets to give 1 if node i and node j are in the same subnetwork and to give 0 is node i and node j are in different subnetworks.

Factor Same Subnetwork

Factor Same Subnetwork describes the number of nodes of the same subnetwork to which node i is connected and can be mathematically described as,

$$S_i = \sum_{j}^{N} \boldsymbol{x}_{ij} \left[v_i = v_j\right] \tag{4.14}$$

With a positive weight, this factor would prioritize node i making connections with nodes that are in the same subnetwork.

Factor Same Subnetwork Transitive Triplets

Factor Same Subnetwork Transitive Triplets describes the number of nodes of the same subnetwork to which node i is connected in a triangle, and can be mathematically described as,

$$ST_i = \sum_j^N \sum_h^N \boldsymbol{x}_{ij}\boldsymbol{x}_{ih}\boldsymbol{x}_{hj}[v_i = v_j] \tag{4.15}$$

With a positive weight, this factor would prioritize node i closing triads with nodes of the same subnetwork. This factor likely inadvertently prioritizes more connections and more triangles as well.

Factor Jump Subnetwork Transitive Triplets

Factor Jump Subnetwork Transitive Triplets describes the number of triangles to which node i is connected with one node of the same subnetwork as node i and one node of a different subnetwork as node i, and can be mathematically described as,

$$JT_i = \sum_j^N \sum_h^N \boldsymbol{x}_{ij}\boldsymbol{x}_{ih}\boldsymbol{x}_{hj}[v_i = v_j \neq v_h] \tag{4.16}$$

With a positive weight, this factor would prioritize node i making triangles with one similar node and one different node. Due to the restricted nature of the triangles, it is unlikely that this will prioritize making more triangles generally.

Factor Same Subnetwork Distance 2

Factor Same Subnetwork Distance 2 describes the portion of the neighbors of node i's neighbors that are of the same subnetwork as node i and can be mathematically described as,

$$S2_i = \sum_j^N \boldsymbol{x}_{ij} \sum_{h \neq i}^N \frac{\boldsymbol{x}_{jh}[v_i = v_h]}{\sum_{k \neq i}^N \boldsymbol{x}_{jk}} \tag{4.17}$$

where $0/0$ is considered to be 0.

This factor differs from the full network Factor Distance 2 in an important way. The full network Factor Distance 2 specifically requires that there is no connection between the nodes connected at a path length of two. However, this factor does not register if the node i and the node at a distance two are themselves connected. Essentially, this counts both completed triangles and uncompleted triangles as being at a distance two, given that they otherwise meet the subnetwork criteria.

With a positive weight, this factor would prioritize node i connecting with nodes that are connected to nodes of the same subnetwork, with an emphasis on connecting with nodes of low degree.

Factor Same Subnetwork 4-Cycles

Factor Same Subnetwork 4-Cycles describes the number of 4-cycles (rectangles) to which node i belongs, given that the node at a distance two on the rectangle is of the same subnetwork as node i, and can be described mathematically as,

$$S4_i = \frac{1}{4} \sum_{j}^{N} \sum_{k \neq j}^{N} \sum_{h \neq j \neq k}^{N} \boldsymbol{x}_{ij} \boldsymbol{x}_{ik} \boldsymbol{x}_{hj} \boldsymbol{x}_{hk} [v_i = v_h] \tag{4.18}$$

With a positive weight, this factor would prioritize node i completing 4-cycles with nodes in the same subnetwork.

Chapter 5

Methods: Model Derivation

Now that we understand the framework of the models that we hope to derive, we can discuss how specific models are derived from the data. There are three components to this process and unique challenges inside each one. The first component is how, given a hypothesis of factors, the weights of those factors are estimated. This component is implemented in Rsiena and is an adaptation of the Generalized Method of Moments and Robbins-Monro algorithm. The second component is the data-driven procedure by which a specific hypothesis of factors is selected. This component utilizes tools in Rsiena, but was developed for this specific application. The final component is the evaluation and comparison of factors and factor weights. This component is a result of the other two components and utilizes both unique and previously implemented procedures.

Since components of this procedure are unique to this project, it is important to test their efficacy on simulated data. This chapter will describe the procedures as they were implemented on the real data set; Chapter 6 will present the simulated data results that provide evidence that this procedure is an effective tool for deriving a specific SAOM model.

5.1 Factor Estimation

The factor estimation is, as stated, based in the Generalized Method of Moments (GMM) and utilizes the Quasi-Newton Robbins-Monro algorithm.

Recall that the GMM is based on the minimization of a function Q, where $Q(\theta) = \bar{g}(\theta)^\top W \bar{g}(\theta)$ (Equation 2.18). The sample moment condition function ($\bar{g}(\theta)$) is a set of criteria that the algorithm will attempt to simultaneously minimize. In the SAOM, this function will contain a measure of overall change (C) as well as the distance between the current value of each factor and the observed value of each factor ($\vec{S}$). These

statistics are

$$C(\boldsymbol{X}) = \sum_{i}^{N} \sum_{j \neq i}^{N-1} |\boldsymbol{X}_{ij} - \boldsymbol{x}_{ij}^{obs}(t_1)| \tag{5.1}$$

$$S_k(\boldsymbol{X}) = \sum_{i}^{N} (s_{ki}(\boldsymbol{X})) \tag{5.2}$$

where N is the number of nodes in the network in the estimation, $\boldsymbol{X}$ is the current network, $\boldsymbol{x}^{obs}(t_1)$ is the observed network at time point t_1, s_{ki} is the factor equation value for factor k and node i. The statistic to be calculated is,

$$g(\boldsymbol{X}) = \begin{bmatrix} C(\boldsymbol{X}) \\ \vec{S}(\boldsymbol{X}) \end{bmatrix} \tag{5.3}$$

$C(\boldsymbol{X})$ describes the total difference across all the nodes between the current network and the observed time point t_1 and $\vec{S}(\boldsymbol{X})$ is the vector of the factor statistics across all nodes for the current network. The statistic g shows that θ (Equation 2.18) contains both the base rate (ρ) from C and the weights for the set of factors (β) from $\vec{S}$.

$$\theta = \begin{bmatrix} \rho \\ \vec{\beta} \end{bmatrix} \tag{5.4}$$

Recall these values from the rate function (Equation 4.3) and the objective function (Equation 4.4).

The current network $\boldsymbol{X}$ is not known and $\bar{g}(\theta)$ is usually determined through simulation. At a particular value of θ, a sample of simulated networks ($\boldsymbol{X}^{sim}(\theta)$) can be produced. From this sample, the minimization function $\bar{g}(\theta)$ can be derived.

$$\bar{g}(\theta) = \frac{1}{n_{sim}} \left(\sum_{k}^{n_{sim}} g(\boldsymbol{X}_k^{sim}(\theta)) \right) - g(\boldsymbol{x}^{obs}(t_2)) \tag{5.5}$$

where n_{sim} is the number of simulations, $\boldsymbol{X}_k^{sim}(\theta)$ is the k^{th} simulated network created with the current θ, and $\boldsymbol{x}^{obs}(t_2)$ is the observed network at time point t_2. The goal is to minimize $\bar{g}$ or to minimize the distance between the observed statistic ($g(\boldsymbol{x}^{obs})$) and the average simulated statistic at the given θ. Minimizing this function means convergence towards the true value of θ in accordance with the GMM.

Recall from the background section, the estimation of parameters in the SAOM is based on the Robbins-Monro algorithm updated with Newton-like features, specifically the inclusion of the Jacobian (Equation 2.31). n in the Robbins-Monro algorithm represents the estimation iteration step in the convergence of θ. In this equation, Z_n is the sample vector of the function and α is the known constant. It can be seen that these values could be replaced with the simulated statistics and the observed statistics, respectively, as seen

in the minimization criteria of Equation 5.5. This means that the algorithm equation for the SAOM is,

$$\theta_{n+1} = \theta_n - a_n D_{\theta_0}^{-1}(\bar{g}(\theta_n)) \tag{5.6}$$

D_{θ_0} refers here to the Jacobian of the set of factors with respect to θ at the initial theta value. In practice, this is done through simulating small perturbations in the values of theta and calculating the Jacobian from those simulations. The inclusion of the Jacobian accounts for, in some ways, the different scales of the factors as well as the interactions between the factors.

Using these theories in practice involves three main steps—initializing, estimating, evaluating.

In the initializing step, θ_0 is found based upon the set of initial conditions or the default initial conditions for each factor[1]. Then, simulations are conducted with small perturbations to the value in theta to calculate an estimation for the Jacobian at θ_0 (D_{θ_0}).

In the estimating step, a set of Monte Carlo simulations are run with the current value of theta, θ_n. Then, the t-ratios ($\tau_k(\theta_n)$) are calculated for all the values in θ_n. The value k represents the specific factor or base rate in θ_n and n represents the current state of θ. The t-ratios are derived from the GMM

$$\tau_k(\theta_n) = \frac{\theta_{nk}}{SE(\theta_{nk})} \tag{5.7}$$

The stopping condition[2] for this step is

$$\max_k |\tau_k| < 0.25 \tag{5.8}$$

If the stopping condition is reached the procedure moves on to the evaluating step. Otherwise, θ_n is updated using the algorithm equation (Equation 5.6) and this estimating step is repeated.

In the evaluating step, a set of Monte Carlo simulations are run on the final estimated $\hat{\theta}$. From these estimated values the overall convergence and standard errors are calculated. The convergence value is

$$\tau_k^{conv}(\hat{\theta}) = \max_k |\tau_k(\hat{\theta})| \tag{5.9}$$

The weighting matrix, W, in these estimations is just the identity matrix (all factors are to be equally prioritized in approaching the observed values). Thus, the standard error values based on Equations 2.29 and 2.28 are

$$SE(\hat{\theta}) = \sqrt{\Sigma_{\hat{\theta}}} = \sqrt{D_{\hat{\theta}}^{\top} \widehat{\Sigma_{\hat{\theta}}} D_{\hat{\theta}}} \tag{5.10}$$

[1]For initial simulations, the default settings in Rsiena were used; however, as the estimation is resolved in the final steps the initial conditions are set to previously derived values. This is the convergence reduction procedure.

[2]0.25 is the default setting in Rsiena. The default setting was used in this project.

where $D_{\hat{\theta}}$ is the Jacobian estimated with small perturbations around the final estimation $\hat{\theta}$.

5.2 Hypothesis-Building Procedure

The estimation of these parameters requires a specific and reasonably-selected hypothesis of the factors that will drive change in the network ($\vec{S}$), as estimation with too many interacting and potentially insignificant factors quickly becomes unwieldy and uninterpretable with extremely large errors. However, in the application of this framework to brain networks, a hypothesis selected through literature or logic could not reasonably be formed due to the absence of literature and the shallow applicability of current knowledge to the selection of potential factors. Instead, a data-driven method for building a hypothesis is required to state with any confidence that the derived model is a reasonable descriptor of the changes to brain networks over time. We developed a novel method utilizing the tools at our disposal to draw statistical conclusions. This "hypothesis-building procedure", as we refer to it, is described in this section, and an analysis of its success in deriving factors on simulated data is included in Chapter 6.

The procedure is designed to sequentially add factors until any additional factor does not meet the 90% confidence interval required to be included. This is done through a series of *score-type tests* where the null hypothesis is that a particular factor has a weight of zero. Having a weight of zero can be interpreted as the factor being excluded. This procedure does take significant amounts of time to conduct all the tests, but it is proposed as an alternative to testing every possible combination. Future research may choose to increase the computational efficiency of this procedure.

Rsiena includes a tool for testing the impact of particular factors using a score-type test. During this test, the parameter is fixed, and all the other factors are allowed to estimate normally. The null hypothesis is that the value for the weight of factor k is zero,

$$\theta_k = 0 \tag{5.11}$$

and the statistic is the t-ratio for that factor.

$$\tau_k(\hat{\theta}_k) = \frac{\hat{\theta}_k}{SE(\hat{\theta}_k)} \tag{5.12}$$

A p-value that is less than 0.1 in this test suggests that the value of the factor k is not zero with a 90% confidence interval. The test is two-tailed because we are only interested in the large deviation when the factor is fixed at 0. This is the test that is conducted repeatedly in the hypothesis-building procedure. I will

refer to the factor that is fixed at zero as the factor being tested in describing the application of these tests.

Now, it is important to realize that the potential factors are not independent. Most of the factors are network measures calculated on the same underlying network structure (Section 4.2). Changes to one factor will impact the values of the other factors, but not necessarily in straightforward, predictable ways. This means that factors are connected in some ways but are not necessarily replaceable by each other. However, certain change behaviors may appear from the inclusion of either factor, making them occasionally challenging to distinguish. Determining which factor is responsible for the general change behaviors seen on the network is the challenge that is addressed by this procedure.

If the factors were independent, the result of the score-type test would be the same regardless of the other factors that are estimated alongside the factor being tested. This is not the case. As a result, the procedure contains two important components—the "all-pairs initialization" and the "motion to reconsider". These two elements acknowledge that the results of the score-type test are, in some ways, dependent on the other factors included, but not tested, in the hypothesis.

The Procedure

The procedure involves three main parts—the all-pairs initialization, the factor addition, and the motion to reconsider.

The procedure begins with the all-pairs initialization. During this process, one factor is fixed and tested with each other factor individually. These tests are completed for every factor pair. For example, if there were three potential factors (A, B, C) the conducted tests would be testing A with B, testing A with C, testing B with A, testing B with C, testing C with A, and testing C with B. The all-pairs initialization was favored over testing factors individually because the factors tested alone were almost always considered significant and often equally so. Individual factor tests could not really distinguish between factors, only between random and non-random change. The all-pairs initialization was able to do both.

After the tests are conducted, the factor with the lowest average p-value for all the tests of that factor, given that $p < 0.1$, is selected as the first factor to add. If none of the average p-values are less than 0.1, no factor can be considered to have a weight that is not zero, and the final hypothesis has no factors (a model with no factors has random change at the rate of the determined rate value).

If a first factor is selected, the factor with the lowest p-value when tested with the first factor, given that $p < 0.1$, is selected as the second factor. The conclusion of the all-pairs initialization is the inclusion of zero, one, or two factors into the current hypothesis. If the procedure determines zero or one factors, the procedure is over. If two factors are determined, the procedure continues to the factor addition step.

During the factor addition step, the current hypothesis is tested with the addition of each of the remaining

potential factors. The factor that yields the lowest p-value, given that $p < 0.1$, is then added to the current hypothesis. Every time a new factor is added, a motion to reconsider is conducted. This is continued until no factor tested with the current hypothesis has a p-value less than 0.1, meaning that the null hypothesis that the tested factors have a weight of zero cannot be rejected with a confidence interval of 90%.

Each time a factor is added during the factor addition step, a motion to reconsider is conducted. The motion to reconsider takes into account the fact that there may have been many factors that were significant, and the factors that were included were just those with the lowest p-value[3]. This allows for the reconsideration of the paths not traveled earlier in the selection processes. It also takes into account that the addition of new factors means that the results of the score-type tests may have changed. It allows for the reconsideration of previously added factors if, in the current model, that factor cannot reject the null hypothesis that its weight is zero.

The motion to reconsider involves each factor in the current hypothesis being tested with the rest of the current hypothesis. This means that the addition of a factor at any time is not a permanent decision; if it is later found that that factor does not meet the requirements when tested with the current hypothesis, it can be removed. All factors with a p-value greater than 0.1 during these tests are reconsidered, meaning they are removed from the current hypothesis, but remain in the list of potential factors. This means that they could be added again as the hypothesis continues to develop. After a motion to reconsider, the factor addition procedure is repeated.

The procedure ends when all the p-values from the tests of all remaining potential factors are greater than 0.1, and therefore none of them can be considered not zero. In this case, there is no statistical reason to include additional factors. This procedure can result in a final hypothesis that has any number of factors from 0 to the total number of potential factors. The factors in the final hypothesis are derived from the data rather than selected from some prediction of which factors are driving change on the network.

This procedure is not perfect and retains many of the limitations that exist when simply selecting a hypothesis. After all, the original list of potential factors is finite and limited, in this project at least, by the factors available and interpretable from RSiena. Therefore, this procedure will not claim to select for the true set of factors underlying change on the networks, but support instead the claim that these factors, in combination, are significant to driving change on the network and no additional factors would provide a stronger convergence if included. The final model that is derived through the hypothesis-building procedure and estimation can provide insight into network changes.

Figure 5.1 shows an example of how the procedure might behave with a set of five potential factors. The

[3]If the p-values are equivalent (usually at zero), the factor with the highest χ^2 value is selected. Finally, if both the p-value and the χ^2 values are equivalent, one of those factors is selected randomly with the knowledge that it may be reconsidered later. This is extremely rare.

table on the left represents the tests that are conducted with the top (dark red) row being the tested factors. Each of the rows below represent an individual set of tests being run on that column's factor. For example, in Frame 1 (all-pairs initialization) Factor A is being tested in a hypothesis with Factor B, another test with Factor C, and so on down the column. The bottom row is the average p-value from each of the tests in that column this average is only relevant during the all-pairs initialization. The boxes on the right represent the various factors, and the blue line encircles the hypothesis at the end of the tests conducted in that frame. For example, in Frame 1 the lowest average p-value is for Factor D as seen in the bottom row of the table so Factor D is in the current hypothesis. One can see that during the second Motion to Reconsider, Factor D which had previously been added could no longer be considered not to be zero ($p > 0.1$) given that the hypothesis now contains Factor B and Factor E. As a result, Factor D is reconsidered and removed from the current hypothesis.

The conclusion of the hypothesis-building procedure is a set of factors that describe change on the network. A different set of factors is found for each time window in the dataset. The next section will go over the next steps in model derivation, including factor consensus, weight estimation, and model evaluation.

5.3 Model Evaluation

After obtaining a hypothesis set of factors for each time window in the dataset. These time window results were examined to determine what, if any, consistency they showed across participants. Some consistency across participants was shown, resembling the consistency found in simulated datasets with the same underlying model. Thus, a reasonable threshold was selected from the simulated data results (Chapter 6).

The dataset was split up into a group from which the hypothesis was determined, the "Hypothesis Group" and a group on which the estimation of the factors was conducted, the "Estimation Group". A set of 40 participants was selected as the Hypothesis Group with a total of 53 functional and 59 structural time windows that have hypothesis-building results. The remaining 220 participants were set aside for the Estimation Group. These groups were not selected entirely randomly due to procedural constraints; however, both groups were determined to be reasonably representative of the ages, sexes, and diagnoses of the full population[4]. The population and sample had indistinguishable distributions of age using a Kolmogorov-Smirnov test (Hypothesis Group: $p = 0.15 > 0.05$, Estimation Group: $p = 0.99 > 0.05$). The population and sample also showed indistinguishable ratios of male and female participants using a χ^2 test of independence (Hypothesis Group: $p = 0.30 > 0.05$, Estimation Group: $p = 0.46 > 0.05$), and indistinguishable ratios of impaired and control using a χ^2 test of independence (Hypothesis Group: $p = 0.53 > 0.05$, Estimation

[4]Population in this context refers to the entire dataset not the generalized case of human brains

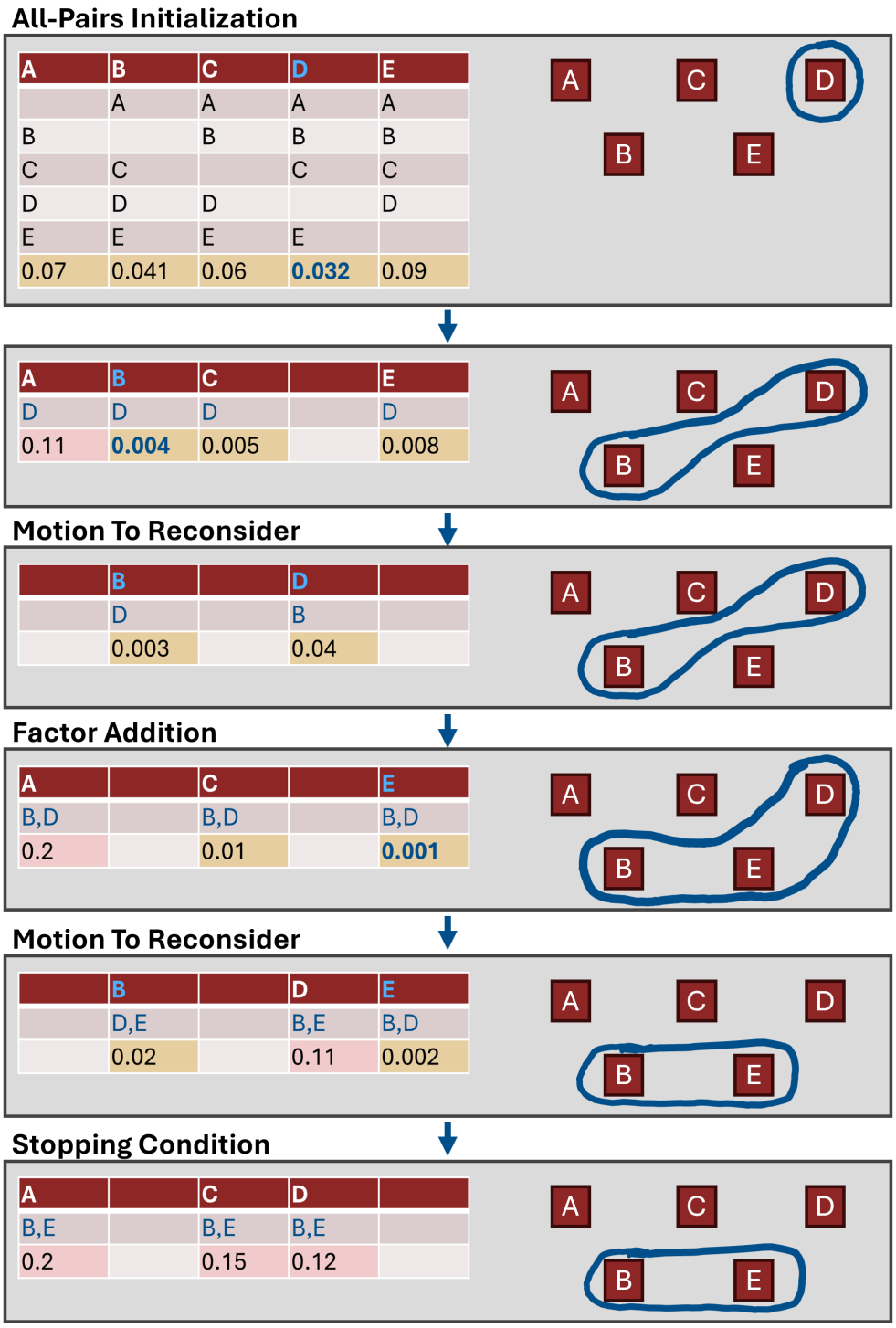

Figure 5.1: **Hypothesis-building procedure.** This figure shows an example of the hypothesis-building procedure with five potential factors. The table on the left shows the tests that were conducted, with the top (dark red) row showing which factors are being tested. The cells below show the factors that are included in the test, but are not being tested. The bottom-most row is the average p-value of all the tests in that column (apart from the all-pairs initialization, this average is only of one test). The boxes on the right represent the factors, and the blue line encloses the factors in the hypothesis at the end of those tests. This graphic demonstrates the ways that hypothesis changes during the hypothesis-building procedure.

Group: $p = 0.26 > 0.05$). Some tests were run on the raw hypothesis-building results for the Hypothesis Group to determine if there were any significant differences in the determined set of factors between the various demographic groups. These results are presented in Chapter 7.

The factors that appeared in 40% of the time windows in the Hypothesis Group were considered to be the factors of the "overall hypothesis". This thresholding was conducted separately on the functional time windows and the structural time windows, as well as the functional subnetworks and structural subnetworks. The subnetworks were considered in combination rather than individually because of the goal of comparability across subnetworks. The subnetwork factor results did not significantly diverge from one another (Chapter 7).

The overall hypotheses for each of these categories were then applied to each individual time window in the Estimation Group. With that set of factors, the weights were estimated with some standard convergence reduction practices as recommended by Rsiena [Snijders 2024].

It was important, once the estimated factor weights were determined, to understand the general shape and pattern of the models, despite most of the result analyses focusing on differences between various groups and conditions.Therefore, a method for determining a meaningful average of the weights of the factors (after thresholding) is useful. We utilized the same method that is applied in Rsiena's meta-analysis; however, we implemented it independently.

The averaging methodology takes into account the standard error values for each of the factor weights that are produced during the estimation process and uses a weighted least squares approach to determine the mean and standard error of the values. The mean equation is

$$\hat{\mu}_k = \frac{\sum_i^{N_I} (\hat{\theta}_k / (\hat{\sigma}_k^{2,OLS} + s_k^2)}{\sum_i^{N_I} (1/(\hat{\sigma}_k^{2,OLS} + s_k^2)} \tag{5.13}$$

where

$$\hat{\sigma}_k^{2,OLS} = \frac{1}{N_I - 1} \sum_i^{N_I} \left(\hat{\theta}_k - \frac{1}{N_I} \sum_i^{N_I} \hat{\theta}_k \right)^2 - \frac{1}{N_I} \sum_i^{N_I} SE(\hat{\theta}_k)^2 \tag{5.14}$$

where N_I are the number of time windows in the set, $\hat{\theta}_k$ is the estimation of the weight of factor k. As stated, this average is used to understand the broad behavior of these models, which are quite individual and significantly impacted by age, sex, and cognitive impairment. The averages as well as the analyses were conducted after a standard removal of outliers that are more than three scaled median absolute deviations from the median.

With the overarching goal of developing models for structural and functional brain networks in aging, we needed to 1) access and process human brain data into networks—preprocessing, 2) understand and apply a

model of network change—the stochastic actor-oriented model, 3) determine the factors involved when these models are applied to the brain—the hypothesis-building procedure, and 4) estimate the weights of those factors—model evaluation. Over the last three chapters, I have discussed each of these steps. Chapter 6 will present the simulated data results, which validate the use of the hypothesis-building procedure, and Chapter 7 will present and discuss the models developed using this methodology on the human brain networks.

Chapter 6

Results: Simulated Data

The goal of the hypothesis-building procedure is to determine the set of factors that is most likely to explain changes in the network. As previously stated, the selection of factors to estimate is generally decided by the researcher prior to the estimation process and can be adjusted after estimation. The hypothesis-building procedure was developed using the tools of these post-hoc adjustments to select a hypothesis (a set of factors) in a data-driven process. In order to evaluate the effectiveness of the hypothesis-building procedure, we utilized a generated set of second time points where the underlying model (the factors and their weights) is known. We will refer to this as the "simulated dataset". In this chapter, I will first describe the simulated dataset and how it was developed. Second, I will report the evaluation of the performance of the hypothesis-building procedure to generate the correct set of factors. Third, I will discuss the features that affect the performance of the hypothesis-building procedure.

6.1 Simulated Dataset

The simulated dataset is a set of networks where time point 2 is generated so that the underlying model is known. We generated these simulated data in two parts. The first part, with an earlier conception of the data and models, is missing certain factors that had not yet been added, and only pulls from the fMRI dataset. The second has fewer simulated examples, but uses the final set of factor options and pulls from both the fMRI and DTI dataset. Both parts are included together in the results presented in this chapter.

The general simulated dataset collection for both parts involves the following steps. First, we randomly selected a network from our dataset—this would be time point 1 (t_1). Second, we selected a rate of change, a set of factors, and weights for those factors. Finally, we produced a network that utilizes the factors and weights that have been assigned to make changes to the network—this would be the simulated time point 2

(t_2^{sim}).

Our simulated dataset consists of 185 model sets—101 in the first part and 84 in the second part—with at least 20, but up to 50, examples of each model. The model sets were created to test the reliability of the hypothesis-building procedure on networks with different t_1s, but the same underlying model. This is to simulate the assumption that the factors that underlie brain network change can be considered the same for all individuals.

There are many points in the process where the computation can fail. The hypotheses as to why this occurs will be discussed in Section 6.2.3. The dataset numbers listed here exclude the examples that did not make it through the procedure.

6.1.1 Selecting a Model

Selecting a model was a crucial step in creating the simulated dataset. There are a number of choices that had to be made regarding the rate, the factors, and the weights.

The rates that were selected from to produce the t_2^{sim}s are $\rho = 5$, $\rho = 20$, $\rho = 35$, $\rho = 50$, and $\rho = 65$. Recall that these represent the number of opportunities for change that each node is likely to have during the simulation. These particular weights were selected to cover a range of values.

Each time a model was selected to simulate, a desired number of factors was specified, and that many factors were then randomly selected. Thus, we controlled the number of factors that the models that had, but we did not control the factors that would be selected. The dataset was designed to contain models with various numbers of factors. Certain factors are underrepresented in the dataset—Factors Physical Distance (PD), Physical Neighbor Distance (ND), and Same Subnetwork 4-Cycles ($S4$) are only contained in the second part of the dataset; thus, they are represented in fewer simulated examples.

Selecting the weights for the different factors is a tricky endeavor as the ranges for the weights are different for each factor and not easily derived. Therefore, it was necessary to create a convention for selecting reasonable weights for each factor. We selected, for each factor, four weight options—a large negative weight, a small negative weight, a small positive weight, and a large positive weight. When a factor is selected, a weight from this set of four is randomly selected.

These four weights were selected independently for each factor based on the density behavior of networks when the factor is simulated alone after many sequential iterations. We simulated a t_2^{sim} with the factor in question as the only factor affecting change, then simulated a t_3^{sim} from that t_2^{sim} with the same model. This was repeated for many iterations to mimic the behavior of a model across a long period of time. The density of the networks, many iterations later, was calculated and compared at various weights for the factor. The

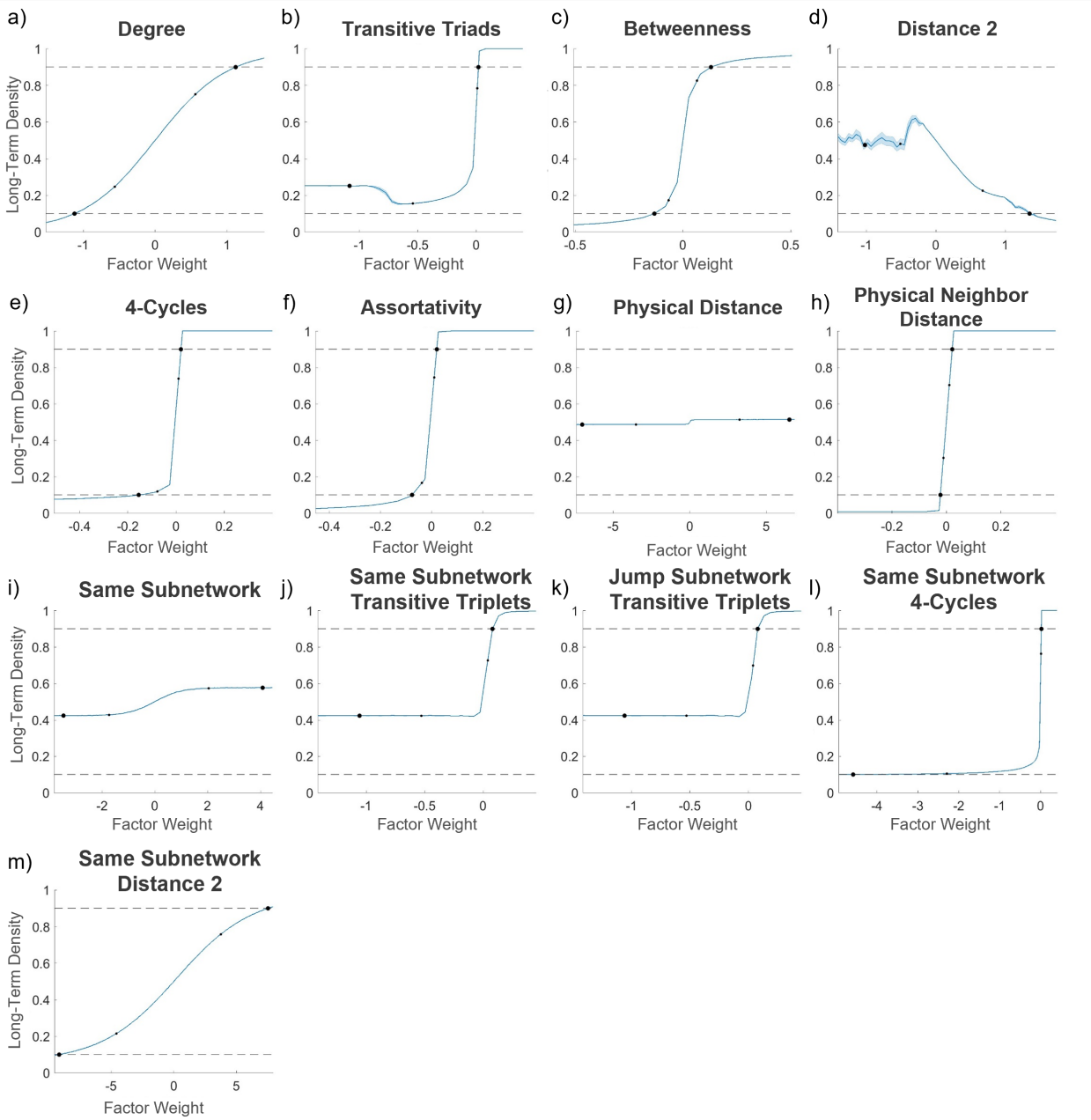

Figure 6.1: **Long-term density of factor weights.** These graphs show the density of the network after many iterations of models with a single factor at various factor weights. This was used to determine reasonable simulation ranges for each factor. Each graph represents a different factor. The large marks show the selected large negative and large positive weights, while the smaller marks represent the small negative and small positive weights.

results of this procedure suggested that the density after a long time converges to a particular value, and this converged density is impacted by the weight of the factor. This became the convention that we used to select the reasonable weights for each factor.

The large negative and the large positive weights were selected as the weights where the density converged to either 10% or 90%. For those factors that level out before reaching those cut-off densities (e.g. Factor Same Subnetwork (S)), the large negative and large positive weights were selected based on the weight at which the density leveled off. Once the large negative and large positive weights are selected, the small negative and small positive weights were calculated as the midpoint between the large weights and zero. The positive and negative values were considered independently.

We would characterize this procedure as a convention rather than a rule because of the odd behavior of certain factors and the inventive nature of the procedure. This convention was selected based on our experience with the SAOM and the behavior that we had observed, rather than on some specific literature. This convention is intended only as a baseline for creating a relevant, comparable simulated dataset. We argue that these selected ranges represent the ranges within which the influence of the factors is well-balanced and the models created the fewest complications. The long-term densities in the selected ranges is graphed in Figure 6.1.

It is important to discuss the limitations of this convention. As we have discussed, the interaction between factors in a model of the SAOM is paramount to the behavior of the network both in the short- and long-terms. Thus, the behavior of a model with a particular factor weight may be a feature only when that factor is alone. Thus, the ill-behaved nature of a model at larger (absolute value) weights of a factor alone may be tempered by the presence of other factors. (Ill-behaved here refers to the network becoming very densely or sparsely connected after many simulations). For example, Factor Same Subnetwork 4-Cycles ($S4$), whose long-term density goes to fully connected with almost any positive weight, would perhaps be able to have a positive weight when other factors are present.

This simulated dataset is not a direct analog to the real dataset; however, it serves as a reasonable baseline for understanding the hypothesis-building procedure and informing future steps in analysis. A simulated dataset like this one can further inform understanding of various factors and their interactions.

6.2 Hypothesis-Building Performance

The main goal in creating a simulated dataset was to evaluate the performance of the hypothesis-building procedure. With our produced t_2^{sim}s, we ran the hypothesis-building procedure to determine whether the procedure was able to correctly identify the factors involved in change. We used measures of *precision*, *recall*,

specificity, and *accuracy* to evaluate the success of the procedure.

The measures of precision, recall, specificity, and accuracy can each reveal unique information about the performance of the procedure.

Precision is calculated as,

$$PR = \frac{TP}{TP + FP} \tag{6.1}$$

where TP indicates the number of true positive values and FP indicates the number of false positive values. Precision can be described as the number of correctly found values out of the total number found.

Recall is calculated as,

$$RE = \frac{TP}{TP + FN} \tag{6.2}$$

where FN indicates the number of false negative values. Recall can be described as the number of correctly found values out of the total number wanted.

Specificity is calculated as,

$$SP = \frac{TN}{TN + FP} \tag{6.3}$$

where TN is the number of true negative values. Specificity can be described as the number of correctly excluded values out of the total number that were not wanted.

Finally, overall accuracy is calculated as,

$$AC = \frac{TP + TN}{TP + FP + TN + FN} \tag{6.4}$$

Accuracy can be described as the number of values that were correctly determined (included or excluded) out of all the possible values.

6.2.1 Overall Performance Analysis

When evaluating all the examples individually, one can calculate the precision, recall, specificity, and accuracy of the procedure by averaging the precision, recall, specificity, and accuracy of each example. The precision, recall, specificity, and accuracy of the individual factors are also calculated as the values across all the examples (In this case, the denominator of accuracy would be equal to the number of examples and not the number of factors).

The procedure demonstrated reasonable precision, low recall, and high specificity. This indicates that the most common mistake is missing a factor that should have been included rather than including a factor that should have been excluded. Furthermore, the precision and recall of individual factors varies greatly,

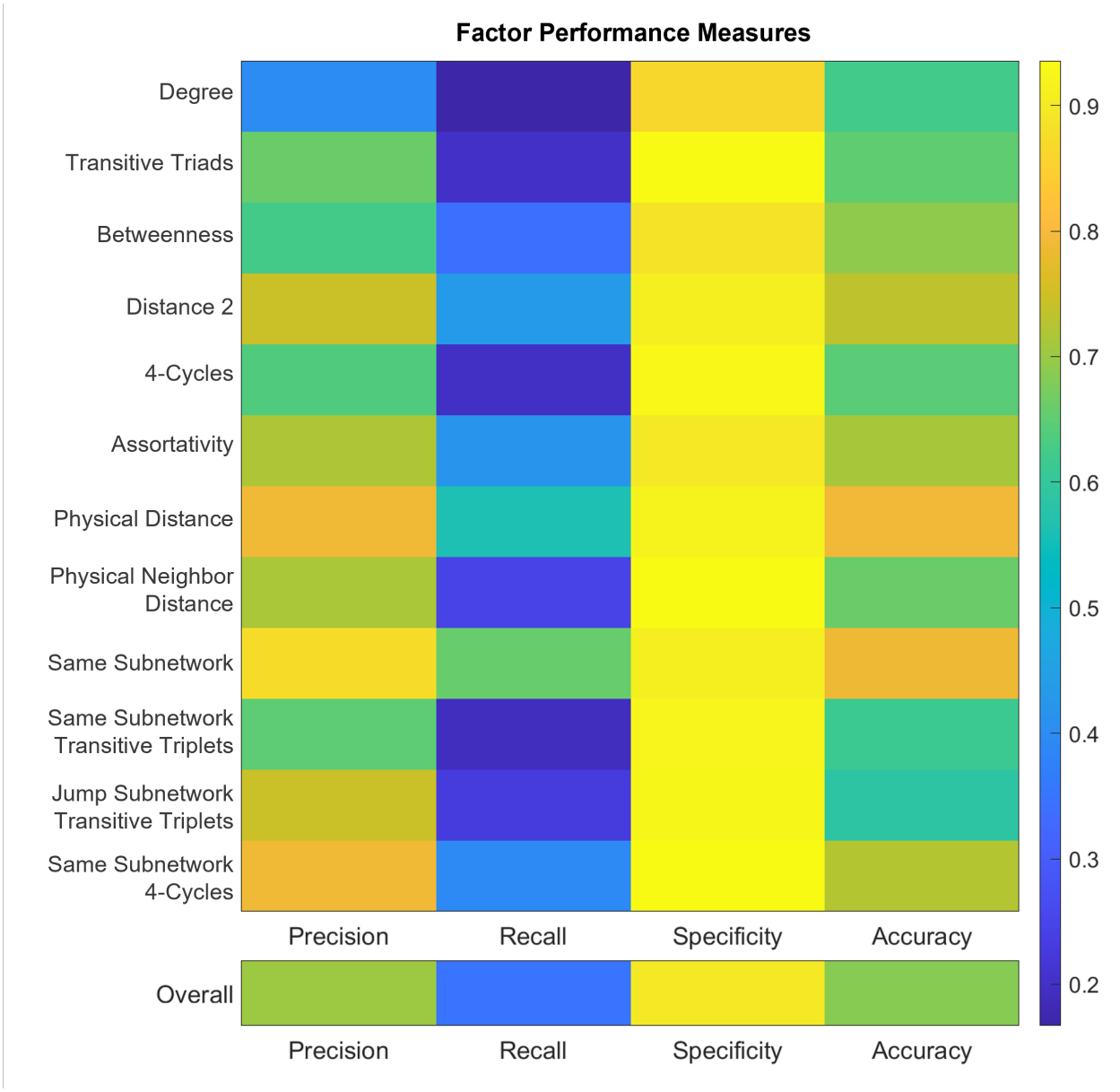

Figure 6.2: **Overall factor performance.** This graph shows the relative success on metrics of precision, recall, specificity, and accuracy of individual factors. The lowest separated row represents the overall success of all the individual examples.

with some demonstrating near perfect alignment with the goals and others performing at or below baseline.

Figure 6.2 shows the relative value of the various success measures for individual factors as well as the overall success measures. Of all the examples individually, the overall precision is $PR = 0.70$, the overall recall is $RE = 0.35$, the overall specificity is $SP = 0.89$, and the overall accuracy is $AC = 0.69$. The precision of individual factors range from $PR_D = 0.40$ to $PR_S = 0.87$. The recall of individual factors range from $RE_D = 0.17$ to $RE_S = 0.66$. The specificity of individual factors range from $SP_D = 0.87$ to $SP_T = 0.94$. The accuracy of individual factors range from $AC_{JT} = 0.59$ to $AC_{PD} = 0.79$.

These results only provide a surface-level analysis of the overall performance of the procedure with excellent specificity and better precision than recall. However, a threshold value was used to develop the receiver operating characteristic (ROC) and precision-recall curves for the model sets. The ROC curve and the precision-recall curve are commonly used tools for determining the success of a particular algorithm or procedure [Buckland 1994, Goutte 2005, Powers 2008]. Thus, much of the remaining analysis will be on analyzing the model sets together.

6.2.2 Model Sets Analysis

Using the model sets, there are further analyses of precision, recall, specificity, and accuracy that can be performed. Each of the 185 model sets has up to 50 examples of results, all with the same underlying model. It can be seen that, in one model, certain factors will appear in a certain percentage of examples, and this corresponds somewhat with the factors that were wanted (Figure 6.3). Using this observation, one can form a final set of factors based upon the percentage of examples that found a particular factor being greater than a certain threshold. For example, Figure 6.3 shows the results of a particular model set, with each row indicating the hypothesis-building procedure result for an example of that model and each column representing a factor. The desired result is shown in the upper bar labeled Goal. With a threshold of, say, 40%, a set with $factor\,1$, $factor\,12$, and $factor\,13$ (black boxes) would be the result with an overall accuracy of $AC = 0.85$.

We calculated the precision, recall, specificity, and accuracy of the model set from the factors found at various percentage thresholds. Then, these values were averaged across all the model sets. These values can produce the ROC curve, which is $(1 - SP)$ (also called the false positive rate) and recall (also called the true positive rate) (Figure 6.4a). We can also produce the precision-recall curve (Figure 6.4b). The area under these curves is considered a demonstration of the procedure's performance, with $AUC = 0.5$ being a procedure of no skill and $AUC = 1$ being a procedure of perfect skill [Saito 2015, Boyd 2013]. Our procedure has an area under the ROC curve of 0.767 and an area under the precision-recall curve of 0.787.

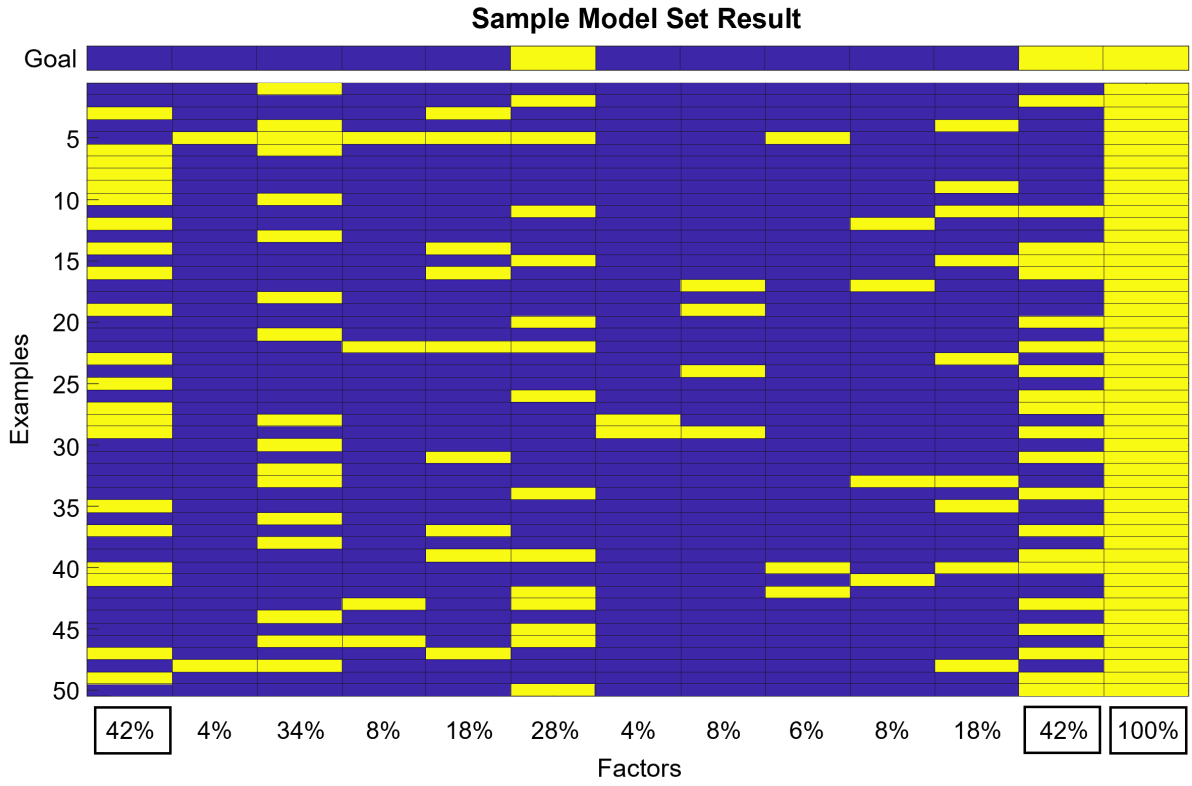

Figure 6.3: **Sample simulated model set** This graph shows one model set with 50 examples. All examples have the same underlying model with three factors. The separate bar above the examples is the underlying model or Goal. Each example produces a set of factors from the hypothesis-building procedure. The results of the procedure for each example are the rows of this graph. Yellow indicates that the factor was found and blue indicates that the factor was not found. The percentages are calculated as the percentage of examples that found that particular factor and are located at the bottom of each column. The percentages in the black boxes indicate those above a 40% threshold.

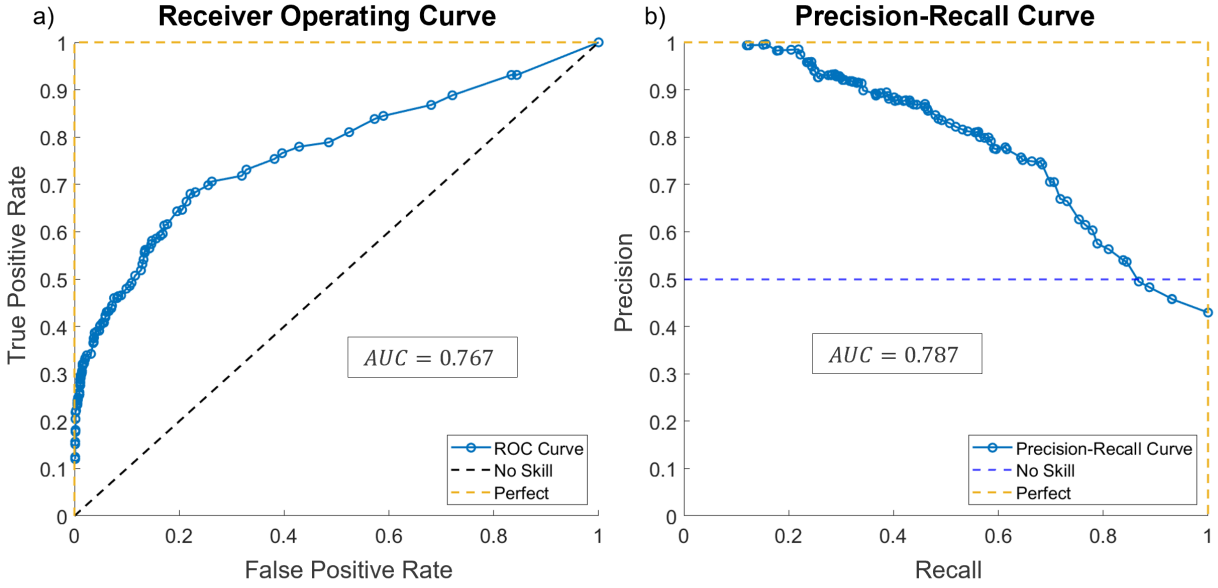

Figure 6.4: **Overall ROC and precision-recall curves.** Figure a) is the ROC curve for the overall hypothesis-building procedure. Figure b) is the precision-recall curve for the overall hypothesis-building procedure. In both graphs, each point on the graph represents a different threshold value. The area under the curve describes the success of the procedure, with 0.5 being no skill and 1 being perfect categorization.

The F-score (F_β) calculates the performance of the procedure on various scales of precision and recall.

$$F_\beta = \left(1+\beta^2\right) \frac{PR \times RE}{\beta^2 \times PR + RE} \tag{6.5}$$

where β represents the fractional priority of recall over precision. A $\beta = 1$ represents the success of the procedure with equal priority of recall and precision. A $\beta > 1$ represents the success of the procedure if recall is considered more important than precision. A $\beta < 1$ represents the success of the procedure if precision is considered more important than recall [Goutte 2005].

The F-score may be calculated at any threshold value, and Figure 6.5 shows F_β graphed as a function of threshold. Various values of β are included to demonstrate the performance based on different priorities of precision and recall. It is evident from the graph that prioritizing precision over recall gives a higher overall performance at most thresholds. This is consistent with the observation that the procedure generally performs better at precision than recall.

Now, to better understand the performance of the individual factors, the F-score curve (Figure 6.6a and 6.6b) can be graphed for each individual factor. These graphs are split into two separate graphs for visual clarity. Precision, recall, specificity, and accuracy are calculated from the thresholded result for each model at the various percentage thresholds. The number of models that correctly found a particular

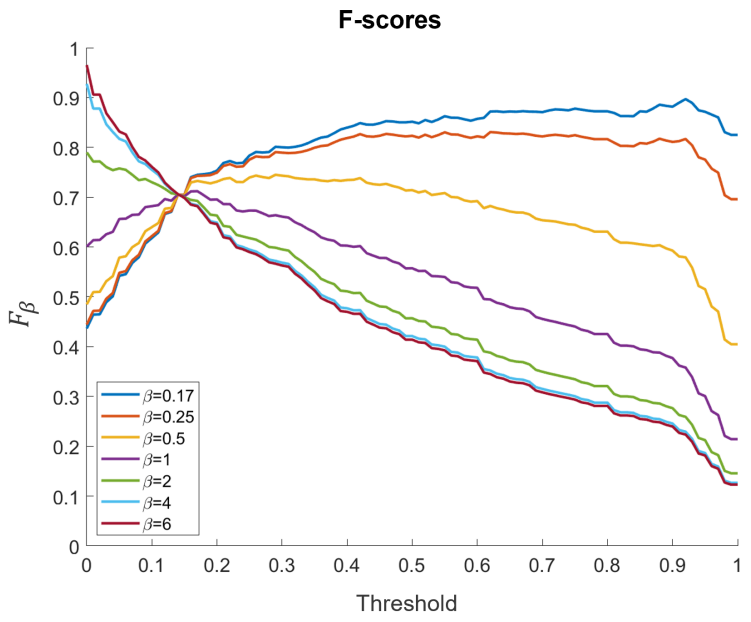

Figure 6.5: **Overall F-score.** The F-score for the overall hypothesis-building procedure at various values of β, demonstrating the superior performance of precision over recall and the differences in overall performance at different thresholds.

factor is the number of true positives. For the individual factors, the $F_{0.5}$ curves were chosen to show the behavior prioritizing precision over recall. It is important to note that this procedure does not include the step of averaging the precision and recall values across the models for each threshold, which makes the graphs less smooth and the performance more sensitive to the number of times a particular factor is wanted. The differences between the number of times that a factor is wanted are known as *class imbalance* [Saito 2015, Richardson 2024].

As can be seen in the performance figures (Figure 6.6), certain factors perform better than others. Some of this variation can be explained by the class imbalance. There is an inherent class imbalance in the simulated dataset due to the two-part nature of the dataset creation. Recall that Factors Physical Distance (PD), Physical Neighbor Distance (ND), and Same Subnetwork 4-Cycles ($S4$) are only found in the second part of the dataset. For these factors, it is likely better to focus on the precision-recall curves rather than the ROC curves in evaluating performance, as the precision-recall curve is less sensitive to low-prevalence class imbalance [Saito 2015]. In this chapter, the F-score values, which are based on the precision-recall curves, are shown. For a more in depth analysis including the ROC curves and precision-recall curves for individual factors, see Appendix A.

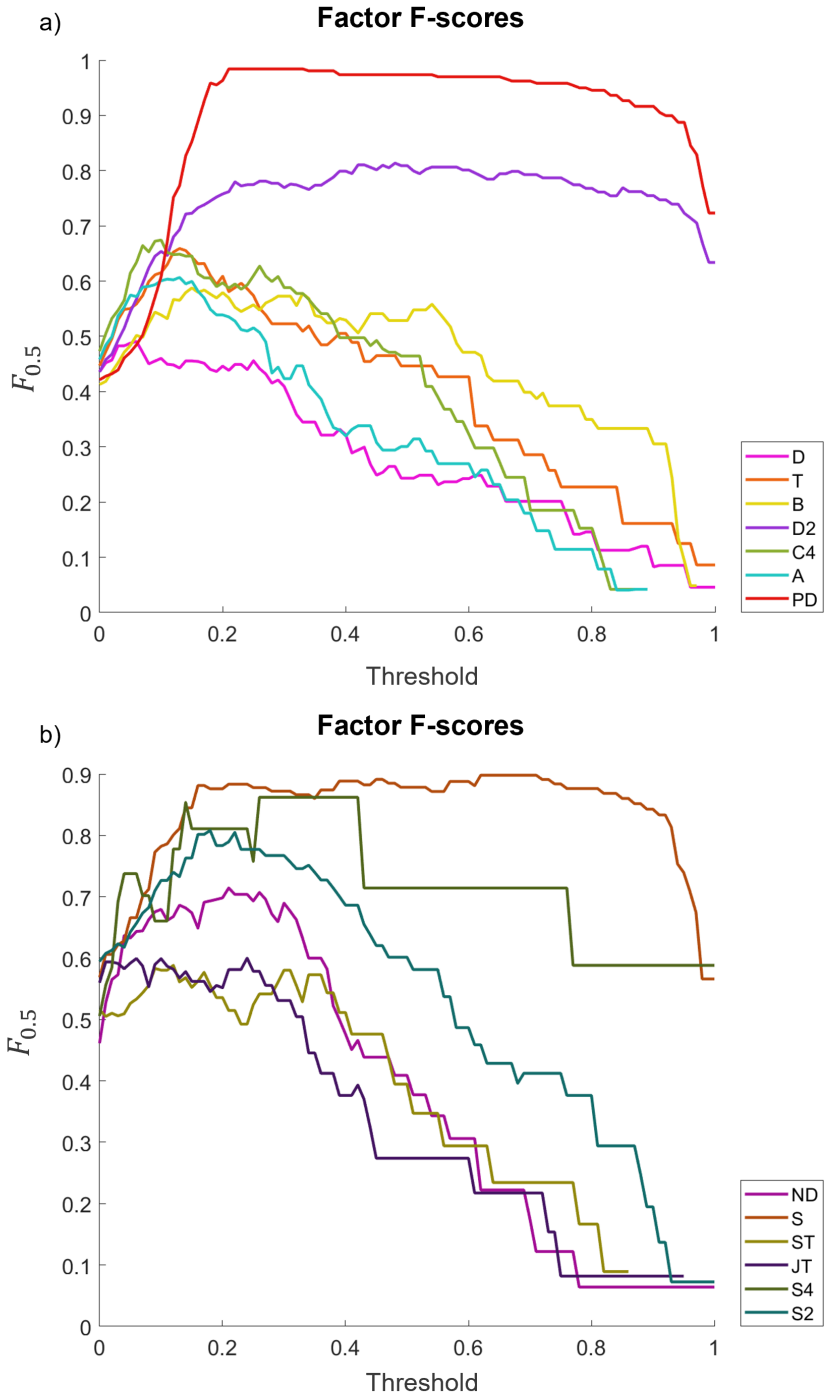

Figure 6.6: **F-scores for individual factors.** The F-score for $\beta = 0.5$ for each of the individual factors with half the factors in Figure (a) and half the factors in Figure (b). The factors were split for visual clarity.

6.2.3 Performance Explanations

There are two main hypotheses that can provide insight into the main shortcomings in performance. The first we will refer to as the "poor model hypothesis", which predicts how certain underlying models are not well-conceived or well-behaved enough to be derivable through any procedure or indeed realistic enough to exist in nature. The second we will refer to as the "interaction effects hypothesis", which describes how, through the interdependence of the various factors, certain factors may become functionally undetectable. It is likely that both these hypotheses play a role in the performance of the procedure. This section will explore these two hypotheses and argue that the procedure performs well enough to be used on the real data.

The Poor Model Hypothesis

Both the hypotheses for the procedure performance rely on an important fact—the conventions used to select an underlying model in these simulated data are somewhat arbitrary. As we saw, the weight ranges were determined through an imperfect convention and, further, no effort was made in balancing the weights of the various factors when they appear together. Thus, it is arguable that the underlying truth is not wholly derivable, nor particularly realistic.

The class imbalance between various factors that influences the performance is not only a result of the disjoint dataset creation, but also impacted by procedure failures. Certain models with a particular factor (or factor weight) may have a higher instance of not making it through the procedure. This suggests that there is some survivorship bias in these results.

A model not making it through the procedure may be due to a number of circumstances. For instance, if the density trends towards one or towards zero, Rsiena will have a hard time running any estimation, let alone the more than fifty-five required in the procedure. Individual factor weights being set too high or too low may disrupt the procedure completion. Other factors demonstrate a strong bias against either positive or negative factor weights that may impact the frequency of procedural failure.

Beyond failure in making it through the procedure, unrealistic models can disrupt the accuracy of correctly identifying the set of factors through particular factors dominating detectable change or creating extremely high variability among t_2^{sim}s.

All of this is evidence of the poor model hypothesis. This hypothesis argues that certain models in the simulated dataset are unrealistic to ever exist in the real data. Recall, for instance, that density is necessarily allowed to fluctuate between t_1 and t_2^{sim} in the simulated data, whereas the density is constant in the real data. Models that significantly increase or decrease the density make the factors less detectable and are fundamentally unrealistic, especially in this real dataset. Additionally, factor weights that were perhaps

set too high, bias against certain weight values, or particular factor combinations can seemingly disrupt the overall derivability of the underlying model. This seems to be an indication not of poor procedural performance, but of poor model conception. These "poor models" could therefore be classified as out of the scope of the hypothesis-building procedure.

Interaction Effects Hypothesis

The poor model hypothesis is robust in explaining, especially those (not inherent) class imbalances, and the models that did not make it through the procedure. However, there are still some performance shortcomings that can be explained by the interaction effects hypothesis. Recall that the main performance mistake in the procedure is missing factors that are supposed to be found. Because of the interdependence of the various factors, it is possible that most of the influence of a particular factor may be partially or mostly explained by another factor, thus increasing the likelihood that one of those factors will be missed.

This can be seen in the often better performance of factors which are determined with non-network information such as Factor Physical Distance (PD). This factor does not rely as heavily on network features and is, therefore, easier to detect. Similarly, the generally poor performance of Factor Degree (D) can be explained by the inadvertent priority of making connections inherent in the definitions of other factors. This could make Factor D harder to detect.

This is very similar to the poor model hypothesis in that some models are less derivable than others, but, while "poor models" can be considered outside the scope of the procedure, the interaction effects hypothesis suggests that even a resultant model that is incorrect by missing factors can still explain most of the changes occurring on the network. This is in line with the hypothesis-building procedure's criteria defined, as it is, as only including the minimum set of factors that can be considered not to be zero.

In combination with the overall performance results, these explanations of the shortcomings increase the confidence with which this procedure is applied to the real dataset. The interpretation of the results will assume that the underlying model that we wish to derive in this work is a well-behaved model that can be explained through some subset of these factors. Of course, the factors included in this list are themselves a limitation, and future work could expand and balance this list to maximize its explanatory power. Finally, it is important to remember that all of these performance results and explanations serve only to confirm within the SAOM framework. These results do not provide evidence of the merits of choosing the SAOM nor of its application to brain networks. These do, however, explain the merits of using the novel hypothesis-building procedure to determine the factors of the specific model of network change. The next section will review the thresholding and estimating procedure based on these simulated data performance results.

6.2.4 Thresholding and Estimating

It was discussed in the model derivation procedure section that after the hypothesis-building procedure is completed, a threshold of 40% is applied. The resultant set of factors is considered the overall hypothesis. Then, those factors' their weights are estimated for each window in the set, regardless of whether the initial hypothesis-building procedure for that window produced those factors. This is done to increase the level of comparability between the windows.

The 40% threshold was selected based upon these simulated results. A 40% threshold states that if at least 40% of the time windows find a particular factor, that factor is included. The peaks in the F-score indicate the highest performing threshold. 40% is near the peak of the overall F-score curve ($\beta = 0.5$) in both the overall and individual factors' F-scores (Figures 6.5 and 6.6). A β value of 0.5 acknowledges the interaction effects hypothesis that the factors being missed do not preclude the resultant model from explaining most of the change. Thus, a 40% threshold was determined to be a reasonable choice given the performance of the procedure.

A simulated dataset allows this procedure to be evaluated for its precision, recall, specificity, and accuracy when the underlying model is known. The procedure is currently specific to undirected networks, and the evaluation of the simulated data was conducted with the goals and assumptions of studying brain networks. However, the basics of this procedure may be useful in other applications with other kinds of networks. It is a proof of concept for applying the SAOM without a specific hypothesis in mind and having the development and derivation of a specific hypothesis be data-driven. Overall, the hypothesis-building procedure is found to be a useful and effective tool for applying the SAOM.

Chapter 7

Results: Aging Models

The application of the procedures that have been discussed to brain networks provides insights into the aging process and into the progression of age-related cognitive impairment. Recall that the dataset covers ages 56-92, and most individuals with impairment have mild impairment. As discussed, this means that results concerning impairment must be put into the context of Mild Cognitive Impairment (MCI). For the calculation and categorization of impairment, we utilized the Clinical Dementia Rating Sum of Boxes (CDR-SB) to retrieve a more dynamic categorization [O'Bryant 2008]. A time window is classified as *control* if the average CDR-SB score across the two time points is less than or equal to 0.5. A time window is classified as *impaired* if the average score is above 0.5, with *mild impairment* between 0.5 and 4, and *significant impairment* above 4.

Throughout this section, statistical tests were run to determine the impact of demographic variables on the factor weights. Certain symbols are used to represent the significance of these statistical tests. If $0.05 \leq p < 0.1$, the test is not significant, but represents a trend or pattern that may be informative; it is marked with a $\dagger$. If $0.01 \leq p < 0.05$, the test is marked with a $*$. If $0.001 \leq p < 0.01$, the test is marked with a $**$. If $p < 0.001$, the test is marked with a $***$. The p-values are reported in the captions of the figures. Recall that all calculations are made after the removal of outlier values.

The first section shows the pre-thresholded factor results to discuss the consistency and variability of the resultant factor lists from the hypothesis-building procedure across subnetworks and demographic groups. The second section covers the factor weight results for the models once the weights are estimated with the same factor list to discuss the behavior of the general model of network change. The final section compares the factor weights between demographic groups.

7.1 Factor Results

This first section covers the inclusion and exclusion of particular factors from the hypothesis-building procedure. It will discuss these results in the context of age, sex, and level of impairment for both the functional and structural networks.

7.1.1 Functional Results

The overall hypothesis for the full fMRI networks includes the following factors:

- Factor Degree

$$D_i = \sum_j^N \boldsymbol{x}_{ij}$$

- Factor Transitive Triads

$$T_i = \sum_{j<h}^{N-1} \sum_h^N \boldsymbol{x}_{ij}\boldsymbol{x}_{ih}\boldsymbol{x}_{jh}$$

- Factor Betweenness

$$B_i = \sum_j^N \sum_h^N \boldsymbol{x}_{hi}\boldsymbol{x}_{ij}\left(1 - \boldsymbol{x}_{hj}\right)$$

- Factor Distance 2

$$D2_i = \sum_j^N \left(1 - \boldsymbol{x}_{ij}\right) \max_h \left(\boldsymbol{x}_{ih}\boldsymbol{x}_{hj}\right)$$

- Factor 4-Cycles

$$C4_i = \frac{1}{4} \sum_j^N \sum_k^N \sum_h^N \boldsymbol{x}_{ij}\boldsymbol{x}_{ik}\boldsymbol{x}_{hj}\boldsymbol{x}_{hk}$$

- Factor Physical Distance

$$PD_i = \sum_j^N \boldsymbol{x}_{ij}(\boldsymbol{w}_{ij} - \sum_h^N \boldsymbol{w}_{ih})$$

- Factor Physical Neighbor Distance

$$ND_i = \sum_j^N \sum_{h \neq j}^N \boldsymbol{x}_{ij}\boldsymbol{x}_{ih}\boldsymbol{w}_{hj}$$

- Factor Same Subnetwork

$$S_i = \sum_j^N \boldsymbol{x}_{ij}\left[v_i = v_j\right]$$

These factors were found in at least 40% of the networks in the Hypothesis Group. Figure 7.1a shows the networks of the Hypothesis Group that found each factor. The banding that is seen in this figure indicates consistency across participants in the factors that are found. The derived factors are indicated with black rectangles. The consistency of certain factors appearing in large numbers of individual time windows is evidence that the change in these networks over time is not random or so individualized as to obscure the overall pattern. Thus, the inclusion of all these factors for all participants in the Estimation Group was preferred.

For the functional subnetworks, the found factors for all the subnetworks combined, as shown in Figure 7.1b,

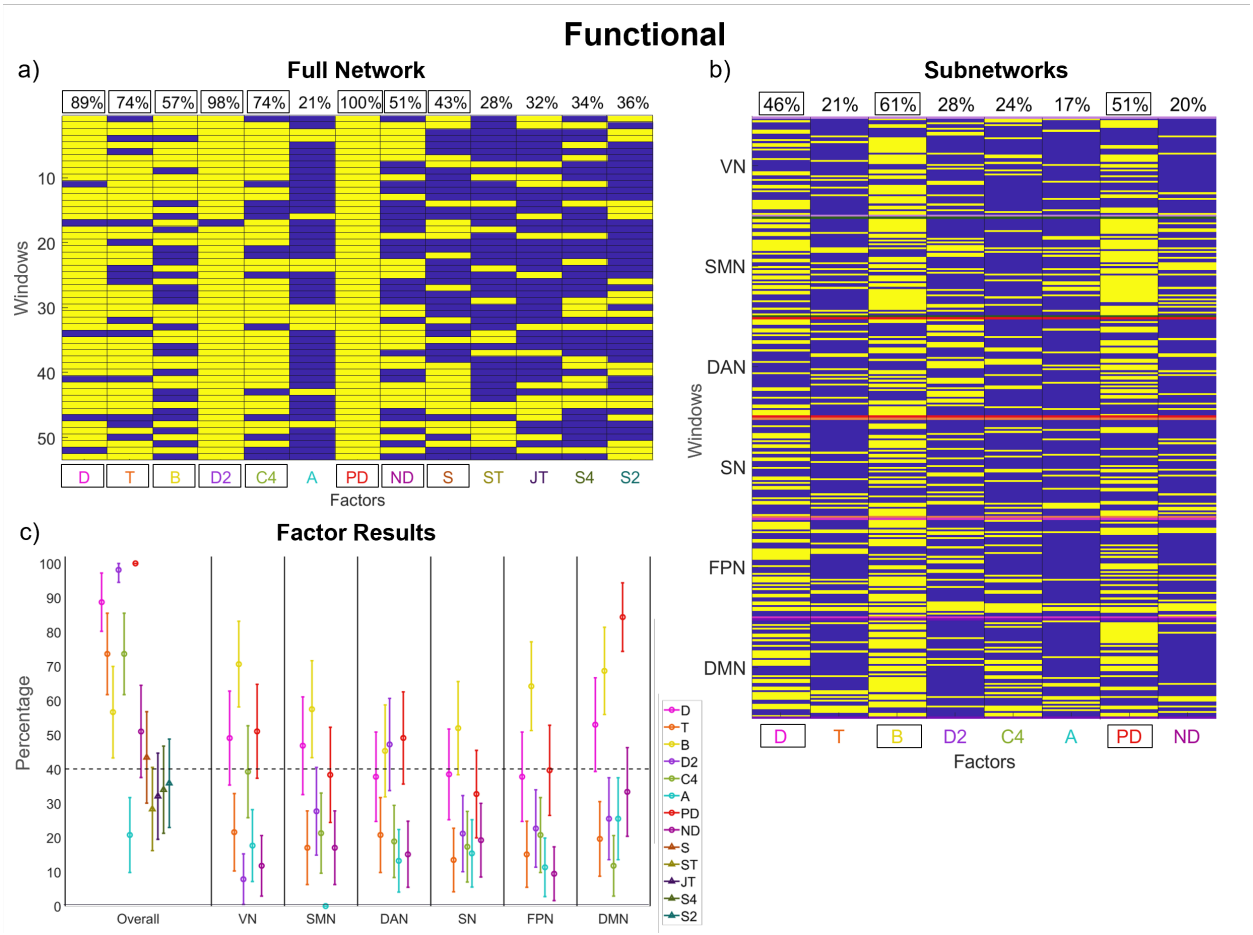

Figure 7.1: **Functional factor results.** These are the results of the hypothesis-building procedure for the functional networks. In Figures (a) and (b), each column is a potential factor and each row is an time window from the Hypothesis Group. Figure (a) shows the full network results, and Figure (b) shows the subnetwork results. For these figures, yellow indicates that the factor was found while blue indicates that the factor was not found. The percentages listed at the top are the percentage of the time windows that found that particular factor. The time windows in Figure (b) are split into the subnetworks as indicated on the y-axis. Figure (c) shows the same percentages separated by subnetwork. The first column of results are those for the full network, and the following columns are the subnetworks. The factors above the dotted line at 40% are those that meet the threshold that was set for inclusion in the overall hypothesis.

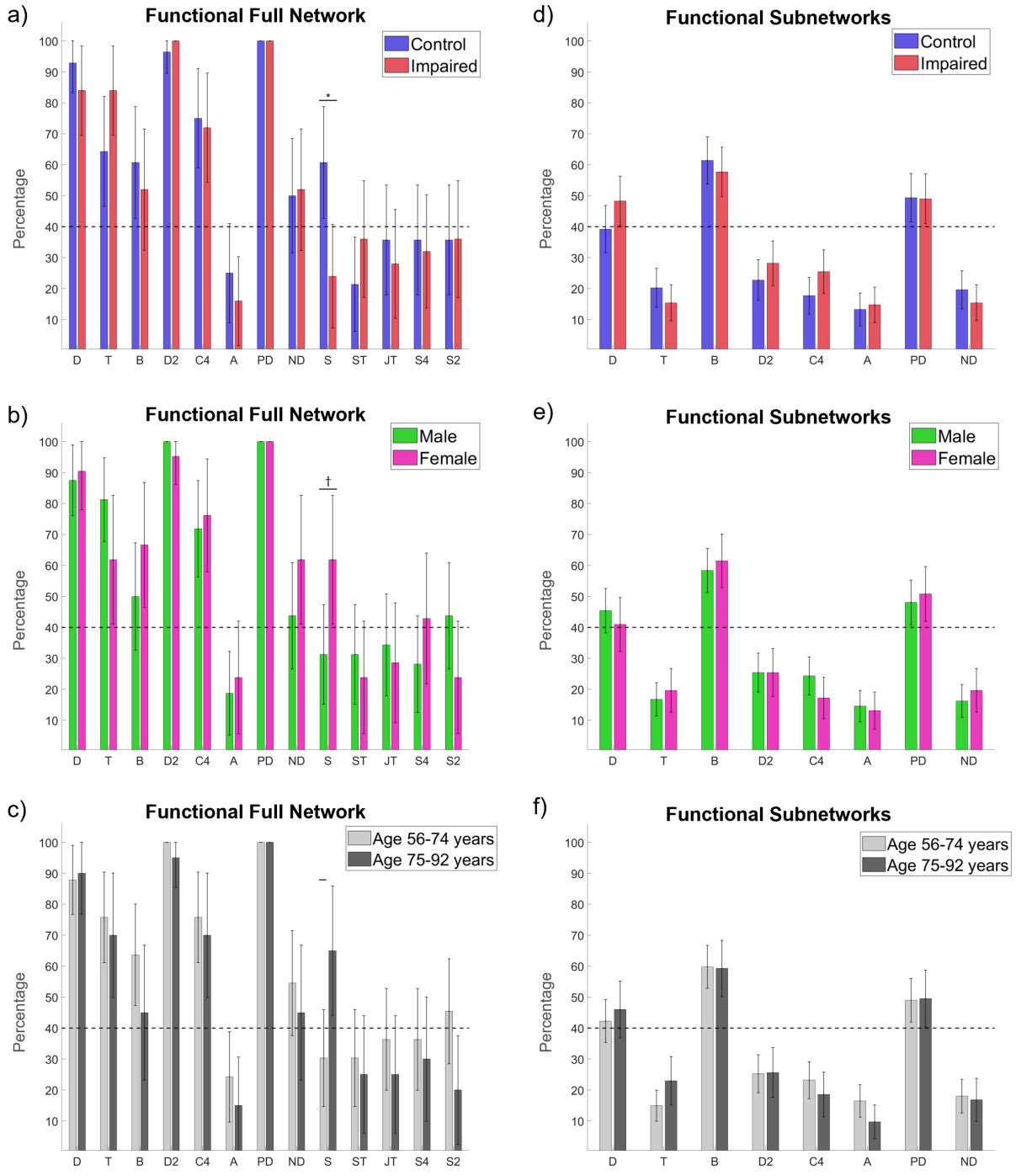

Figure 7.2: **Functional factor result comparisons.** These are the results for the analysis of the inclusion and exclusion of factors based on the demographic measures of impairment group (Figures a and d), sex (Figures b and e), and age group (Figures c and f). Figures (a), (b), and (c) are for the full functional networks, while Figures (d), (e), and (f) are for the functional subnetworks. Three analyses showed significant differences or trends between groups for prevalence of Factor Same Subnetwork (S) in the full network—impairment: $p = 0.016$, sex: $p = 0.055$, and age: $p = 0.029$.

were Factor Degree (D^S), Factor Betweenness (B^S), and Factor Physical Distance (PD^S). The potential factor list for the subnetworks is shorter than the full network list because it does not contain the subnetwork interaction factors (S,ST,JT,$S4$,$S2$). Figure 7.1c shows the percentages broken down by the individual subnetworks. As can be seen, the subnetworks differ somewhat in which factors were found in each. For instance, subnetwork DAN uniquely found Factor $D2^S$ and it can be seen in Figure 7.1b that the time windows in the DAN that found Factor $D2^S$ often did not find Factor B^S indicating some impact of the overlap of these two factors. However, the consistently high values for the three found factors indicate their explanatory significance to general subnetwork change over time.

The percentage of each factor found in the functional networks can also be analyzed for differences across impairment groups, sex, and age groups as shown in Figure 7.2. These comparisons were conducted for each of the full network factors and the subnetwork factors. The significances are from a Yates's corrected χ^2 test of the proportion of that factor found in each group. Significant differences were found in the impairment group and age group for Factor Same Subnetwork (S) ($p = 0.016$ and $p = 0.029$, respectively). However, it is hard to say with the small sample size which of these demographic categories has the greatest impact or how they interact. As this factor is included in the overall hypothesis, the factor weight with these demographic measures may provide greater insight into these observed differences.

7.1.2 Structural Results

The overall hypothesis for the full structural networks includes mostly the same factors as the functional result, except Factor Same Subnetworks (S) was not found, and Factor Assortativity (A) was found. These are the resultant factors for the structural networks.

- Factor Degree

$$D_i = \sum_{j}^{N} \boldsymbol{x}_{ij}$$

- Factor Betweenness

$$B_i = \sum_{j}^{N} \sum_{h}^{N} \boldsymbol{x}_{hi}\boldsymbol{x}_{ij}\left(1 - \boldsymbol{x}_{hj}\right)$$

- Factor Transitive Triads

$$T_i = \sum_{j<h}^{N-1} \sum_{h}^{N} \boldsymbol{x}_{ij}\boldsymbol{x}_{ih}\boldsymbol{x}_{jh}$$

- Factor Distance 2

$$D2_i = \sum_{j}^{N} \left(1 - \boldsymbol{x}_{ij}\right) \max_{h} \left(\boldsymbol{x}_{ih}\boldsymbol{x}_{hj}\right)$$

- Factor 4-Cycles

$$C4_i = \frac{1}{4}\sum_{j}^{N}\sum_{k}^{N}\sum_{h}^{N} \boldsymbol{x}_{ij}\boldsymbol{x}_{ik}\boldsymbol{x}_{hj}\boldsymbol{x}_{hk}$$

- Factor Assortativity

$$A_i = \sum_{j}^{N} \boldsymbol{x}_{ij}\left[v_i = v_j\right]$$

- Factor Physical Distance

$$PD_i = \sum_{j}^{N} \boldsymbol{x}_{ij}(\boldsymbol{w}_{ij} - \sum_{h}^{N} \boldsymbol{w}_{ih})$$

- Factor Physical Neighbor Distance

$$ND_i = \sum_{j}^{N}\sum_{h\neq j}^{N} \boldsymbol{x}_{ij}\boldsymbol{x}_{ih}\boldsymbol{w}_{hj}$$

These factors were found in at least 40% of the structural networks in the Hypothesis Group. Figure 7.3a shows the networks of the Hypothesis Group that found each factor.

Figure 7.3b shows the factor results for the structural subnetworks. The set of found factors for the combined set of subnetworks is just Factor Physical Distance (PD^S). The percentages for the individual subnetworks, shown in Figure 7.3c, demonstrate consistency with the functional results (Figure 7.1c) in that the default mode network (DMN) retains the most factors. This may be because it is the largest subnetwork with 24 nodes. The second largest subnetwork is the visual network (VN) with 17 nodes. Interestingly, in the functional analysis, the VN retained all the factors, albeit with a lower proportion of Factor PD^S (red); however, in the structural analysis, no factors were found in the VN. This could possibly be explained by the larger spread of the nodes in the DMN compared to the VN, which is considered one of the most local subnetworks [Yeo 2011]. This could dampen the influence of Factor PD^S in the VN.

The demographic analysis between impairment groups, sex, and age groups for the structural networks shown in Figure 7.4 indicate no strong differences that impact the inclusion or exclusion of a factor, as the differences found are either well-below or well-above the 40% threshold.

7.2 Factor Weight Results

This section will show the results once the networks are thresholded and estimated with the same factors. Because the factor weights show significant differences on measures such as impairment group, sex, and age (Section 7.3), the reported weights are not indicative of universal applicability as a model. However, the purpose of these averages is descriptive rather than predictive, offering a dynamical explanation for the trends seen in previous research. Therefore, it is important to understand the general model that is found to describe how these networks are changing. These averages are calculated using the mean least squares approach discussed in Chapter 5 to include the uncertainty both from the estimation and between participants.

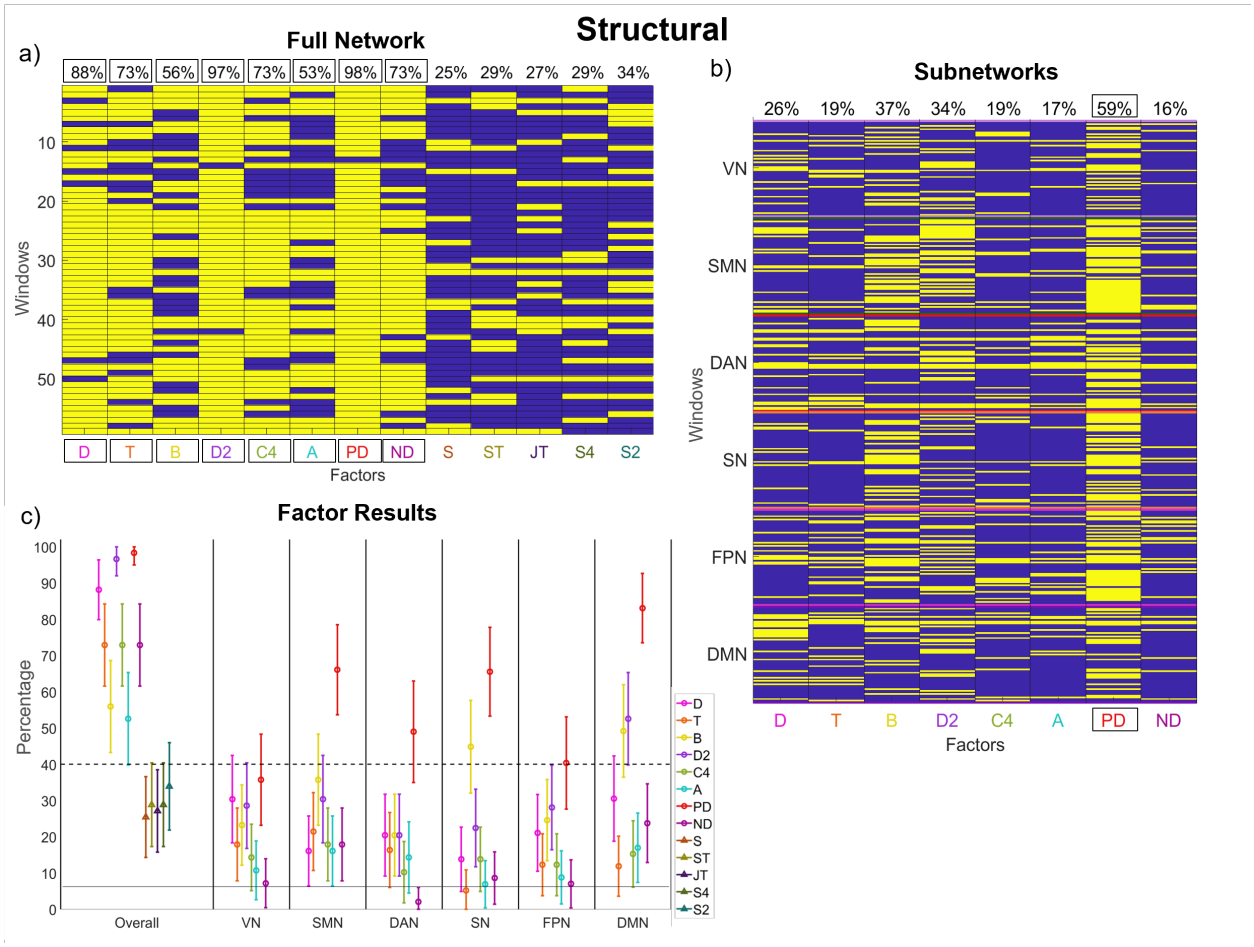

Figure 7.3: **Structural factor results.** These are the results of the hypothesis-building procedure for the structural networks. In Figures (a) and (b), each column is a potential factor and each row is a time window from the Hypothesis Group. Figure (a) shows the full network results, and Figure (b) shows the subnetwork results. For these figures, yellow indicates that the factor was found while blue indicates that the factor was not found. The percentages listed at the top are the percentage of the time windows that found that particular factor. The time windows in Figure (b) are split into the subnetworks as indicated on the y-axis. Figure (c) shows the same percentages separated by subnetwork. The first column of results are those for the full network and the following columns are the subnetworks. The factors above the dotted line at 40% are those that meet the threshold that was set for inclusion in the overall hypothesis.

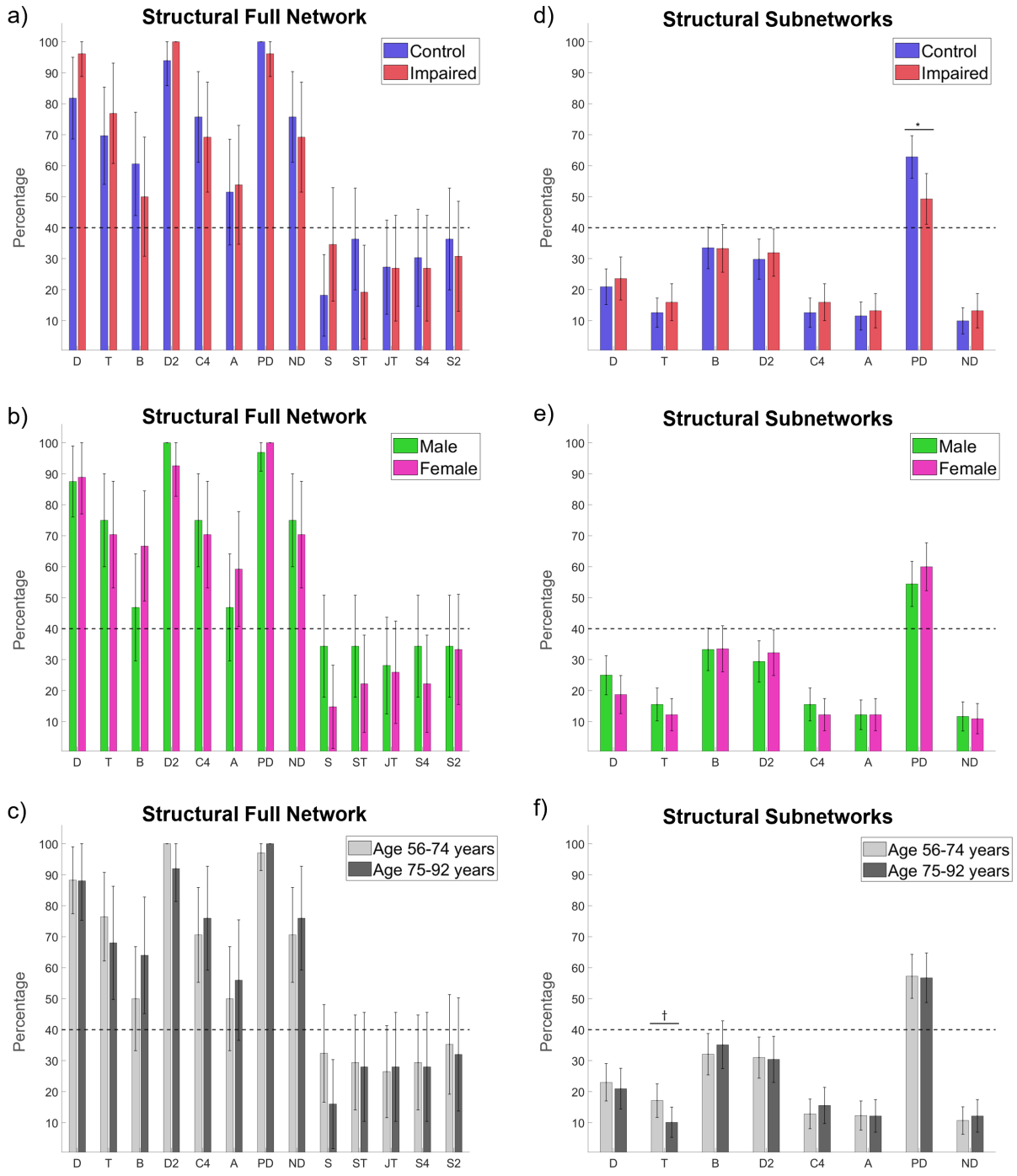

Figure 7.4: **Structural factor result comparisons.** These are the results for the analysis of the inclusion and exclusion of factors based on the demographic measures of impairment group (Figures a and d), sex (Figures b and e), and age group (Figures c and f). Figures (a), (b), and (c) are for the full structural networks, while Figures (d), (e), and (f) are for the structural subnetworks. Two analyses showed significant differences or trends between groups in the subnetwork results—for impairment group differences for Factor Physical Distance (PD) ($p = 0.018$) and for age group differences for Factor Transitive Triads (T) ($p = 0.095$). However, all of these differences are well-above or well-below the 40% threshold for the difference to have an impact on factor inclusion.

Factor	Functional	Structural
ρ	$(5.75 \pm 0.17) \times 10^{1}$	$(1.79 \pm 0.12) \times 10^{1}$
D	$(-102.0 \pm 1.6) \times 10^{-2}$	$(-189 \pm 4) \times 10^{-2}$
T	$(259 \pm 5) \times 10^{-3}$	$(259 \pm 5) \times 10^{-3}$
B	$(-45.0 \pm 1.4) \times 10^{-3}$	$(-17 \pm 3) \times 10^{-3}$
$D2$	$(-114 \pm 2) \times 10^{-3}$	$(-111 \pm 3) \times 10^{-3}$
$C4$	$(-72 \pm 2) \times 10^{-4}$	$(-64 \pm 2) \times 10^{-4}$
A		$(-9 \pm 2) \times 10^{-3}$
PD	$(-69 \pm 2) \times 10^{-4}$	$(-226 \pm 6) \times 10^{-4}$
ND	$(11.0 \pm 0.8) \times 10^{-5}$	$(20.0 \pm 1.4) \times 10^{-5}$
S	$(28.0 \pm 1.9) \times 10^{-2}$	

Table 7.1: **Full network factor weights.** This table shows the weighted average values and standard errors for the factors in the full network models for both functional and structural. These averages include all participants.

7.2.1 Full Network Results

The results for the full networks are shown in Table 7.1. It is important to remember that these weights are not normalized. Thus, the relatively low values for Factor Physical Neighbor Distance (ND), for example, are not indicative that Factor ND has a lower impact compared to the other factors. For the purposes of this discussion, I will focus mainly on the signs of the weights, which indicate whether the network is changing towards or away from that factor. These factors interact in unique and interesting ways, and I will discuss some of those here. Figure 7.5 shows a series of toy networks that will aid in this discussion.

Factor Degree (D) is the number of connections to which a node is connected (Figure 7.5a). A negative weight for Factor D suggests that nodes in the network are unlikely to connect with one another unless there is some other incentive from the other factors in the model. In other words, it can be said that connections are expensive.

Factor Transitive Triads (T) is the number of triangles to which a node belongs (Figure 7.5b). A positive weight for Factor T indicates that nodes in the network want to make triangles. This factor is connected to clustering in traditional network analysis. If the first two factors were alone in the model, it would indicate

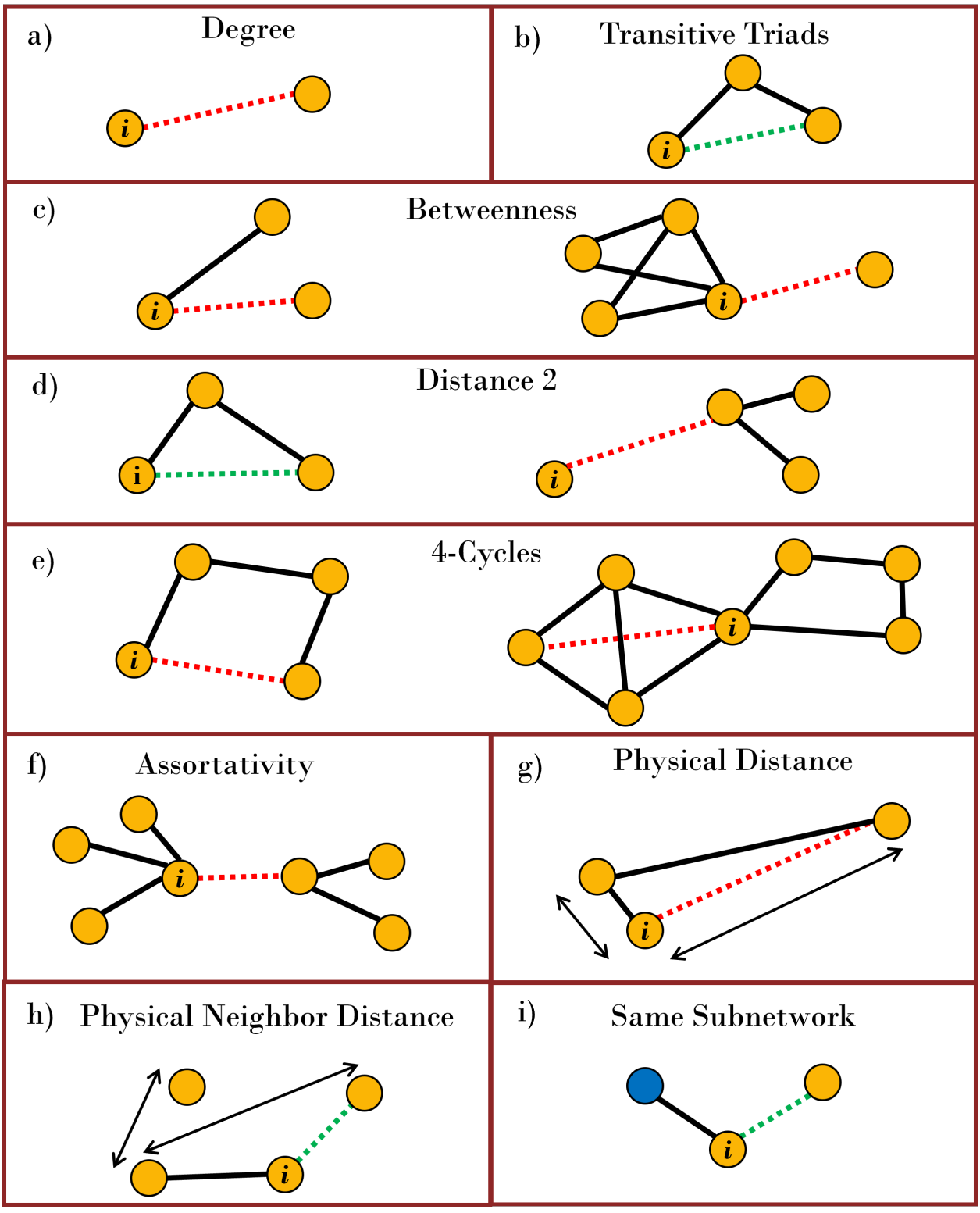

Figure 7.5: **Factor toy networks for the models.** These toy networks demonstrate the local behaviors of various factors in accordance with the models found in the brain networks. Red dotted lines indicate the likelihood to dissolve a connection, while green dotted lines represent the likelihood to build a connection given the weights. Arrowed lines demonstrate physical distance.

that nodes are unlikely to connect with other nodes unless a triangle is formed.

Factor Betweenness (B) is a measure of to how many pairs of disconnected nodes a node is connected (Figure 7.5c). A negative weight for Factor B indicates that nodes in the network will tend to dissolve connections with nodes that are not part of their own neighborhood, as these nodes are likely to be disconnected from a large number of the node's neighbors. The second toy network in Figure 7.5c shows this dynamic.

Factor Distance 2 ($D2$) is a measure of the number of nodes that a node is not directly connected to, but is connected to at a distance of two connections (Figure 7.5d). This is a measure of network distance and not physical distance like Factors PD and ND. A negative weight for Factor $D2$ indicates, in harmony with Factor T, that nodes will tend to close the gap between nodes that are at a path length of two. The first image in Figure 7.5d shows this. However, dissolving connections can also be an effective way to decrease a node's measure of Factor $D2$. Specifically, by dissolving connections with highly connected nodes of different neighborhoods the measure of Factor $D2$ can be reduced by more than just one node. The second image in Figure 7.5d shows this dynamic. Since this factor does not count how many ways a node is connected at a distance of two, redundancies in the network remain quite robust to this factor.

Factor 4-Cycles ($C4$) is a measure of the number of rectangles to which a node belongs (Figure 7.5e). With a negative weight, Factor $C4$ indicates that nodes will decrease their connections with rectangles. This measure does not distinguish between rectangles where the node of interest is a part of a triangle and ones where it is not, indicating some interplay with Factor T. Of particular interest for this factor is the kite shape shown in the second toy network in Figure 7.5e in which node i is a part of eight rectangles and dissolving one of these connections in the kite would eliminate four of those rectangles compared to eliminating two by dissolving from the open rectangle (remember that nodes are only allowed to make one change at a time). The redundancies in the network are not as robust to this factor as they are to Factor $D2$. Thus, this factor, with a negative weight, can indicate an increase in local efficiency.

Factor Assortativity (A), which is only present in the structural models, is a measure of the connectivity of a node and its neighbors (Figure 7.5f). The impact of this factor is scaled by the connectivity of the node of interest. So, Factor A is not a true measure of assortativity, where low-degree nodes connect with low-degree nodes and high-degree nodes connect with high-degree nodes. Instead, if the node of interest is low-degree, the factor is less impactful and will give a slight negative preference to high-degree nodes, but if the node of interest is high-degree, the factor has a much higher impact and the node is much more likely to avoid connecting with other high-degree nodes. With a negative weight, this factor indicates that high-degree nodes are likely to dissolve their connections with other high-degree nodes breaking hub-to-hub connectivity.

Factor Physical Distance (PD) is a measure of the sum of the physical distances (Euclidean distances)

between a node and its neighbors (Figure 7.5g). With a negative weight, this factor indicates that nodes will tend to dissolve connections with the furthest away nodes and build connections with local nodes.

Factor Physical Neighbor Distance (ND) is a measure of the physical distance between a node's neighbors regardless of their distance from the node itself (Figure 7.5h). With a positive weight, this factor indicates that nodes tend to connect with nodes that are far away from their own neighbors. Along with Factor PD, this indicates that the connections in the network are traversing the brain through local hops across the brain space—connecting with the local node furthest away from its neighbors.

Factor Same Subnetwork (S), which is only found in the functional models, is a measure of a node's connectivity with members of its own subnetwork (Figure 7.5i). With a positive weight, this factor indicates that nodes are more likely to connect with members of their own subnetwork or, in combination with Factor D, dissolve connections with nodes of other subnetworks. This is likely to increase connectivity within subnetworks and descrease cross-network connectivity.

7.2.2 Subnetwork Results

The results for the subnetworks are displayed in Table 7.2. While the factors involved in the subnetworks are mathematically the same as in the full network, careful consideration of their interpretation in context can lead to some unique conclusions.

Factor Degree (D^S) has a positive weight in the functional subnetwork models, despite a negative weight in the full network models. This is because this factor is a measure of connectivity within the subnetwork and is more closely tied to Factor S, establishing that connections within subnetworks are less expensive than connections outside of subnetworks. This is in harmony with the results for Factor S in the full network.

The subnetwork Factor Betweenness (B^S) would be less focused on dissolving connectivity between large-scale modular groups (like the subnetworks themselves tend to be). Instead, with a negative weight, this factor is likely to decrease the connectivity of internal subnetwork hubs, which tend to have the highest betweenness in a highly-connected network.

The subnetwork Factor Physical Distance (PD^S) is still closely tied to the full network measure of physical distance; however, in the subnetworks, this factor interplays with the established geometry of the subnetworks. In the full network, the nodes are evenly spaced, while in the subnetworks, some subnetworks are more spread out than others. For instance, the DMN has a large spread while the VN has a small spread [Yeo 2011]. We might expect to see long-range connections be more expensive in the DMN than the VN, but this is not the case in the functional models. this suggests that the DMN is more willing to make distant connections despite its geometry. This is an excellent way to highlight that the factor weights across

Factor	Functional	Structural
VN		
ρ	2.41 ± 0.09	0.76 ± 0.05
D^S	$187 \times 10^{-2} \pm 3 \times 10^{-2}$	
B^S	$-62.2 \times 10^{-2} \pm 1.2 \times 10^{-2}$	
PD^S	$-16.1 \times 10^{-3} \pm 0.8 \times 10^{-3}$	$-23 \times 10^{-3} \pm 2 \times 10^{-3}$
SMN		
ρ	1.73 ± 0.08	1.06 ± 0.07
D^S	$177 \times 10^{-2} \pm 4 \times 10^{-2}$	
B^S	$-81 \times 10^{-2} \pm 2 \times 10^{-2}$	
PD^S	$-6.3 \times 10^{-3} \pm 0.6 \times 10^{-3}$	$-36 \times 10^{-3} \pm 2 \times 10^{-3}$
DAN		
ρ	5.3 ± 0.3	0.65 ± 0.04
D^S	$168 \times 10^{-2} \pm 4 \times 10^{-2}$	
B^S	$-76.1 \times 10^{-2} \pm 1.8 \times 10^{-2}$	
PD^S	$-11.1 \times 10^{-3} \pm 0.6 \times 10^{-3}$	$-17 \times 10^{-3} \pm 3 \times 10^{-3}$
SN		
ρ	1.07 ± 0.05	0.81 ± 0.04
D^S	$133 \times 10^{-2} \pm 6 \times 10^{-2}$	
B^S	$-94 \times 10^{-2} \pm 4 \times 10^{-2}$	
PD^S	$-10.2 \times 10^{-3} \pm 0.7 \times 10^{-3}$	$-35.2 \times 10^{-3} \pm 1.6 \times 10^{-3}$
FPN		
ρ	3.49 ± 0.20	0.50 ± 0.03
D^S	$129 \times 10^{-2} \pm 5 \times 10^{-2}$	
B^S	$-86 \times 10^{-2} \pm 3 \times 10^{-2}$	
PD^S	$-9.2 \times 10^{-3} \pm 0.4 \times 10^{-3}$	$-15.3 \times 10^{-3} \pm 1.1 \times 10^{-3}$
DMN		
ρ	9.43 ± 0.53	1.56 ± 0.07
D^S	$184 \times 10^{-2} \pm 3 \times 10^{-2}$	
B^S	$-66 \times 10^{-2} \pm 1.0 \times 10^{-2}$	
PD^S	$-8.1 \times 10^{-3} \pm 0.3 \times 10^{-3}$	$-21.2 \times 10^{-3} \pm 0.9 \times 10^{-3}$

Table 7.2: **Subnetwork factor weights** This table shows the weighted average values and standard errors for the factors in the subnetwork models for both functional and structural. These averages include all participants.

subnetworks are not directly comparable due to their differing numbers of nodes, despite having the same model. However, these may be an indication of the need for further exploration as to the physical constraints on connectivity in the subnetworks. Keeping the differing geometry in mind while analyzing this factor is important to understanding the meaning of differences in this factor.

Overall, the functional subnetworks are connecting within their own community, decreasing the connectivity of the internal hubs, and choosing more local connections. The structural subnetworks are mostly driven by the negative prioritization of the distance between their nodes, indicating some segregation inside the subnetworks based on distance. These results are mostly in keeping with the full network results; however, there is some indication of heterogeneity in these subnetwork weight results, which can inform later analyses.

7.2.3 Functional and Structural Comparisons

The first thing to establish is that because the functional and structural networks have different models, the weights of the factors are not directly comparable. As a result, this section will talk generally about the observable differences between the functional and structural models based on what is known about the factors' behaviors.

The rate (ρ) is defined as the average number of opportunities that each node in the network will have to change between time point 1 (t_1) and time point 2 (t_2). One can see the much higher rate in the functional compared to the structural. Changes are happening more rapidly in the functional network.

The weights for Factors D, PD, and ND are much higher (in absolute value) in the structural compared to the functional, with many of the other priorities staying at similar values. This indicates that the relative impact of these factors is higher in the structural models. It is likely that connections, especially those that span large distances, are more expensive in the structural networks compared to the functional.

The impact of Factor B is much lower in the structural compared to the functional; however, looking at the addition of Factor A might provide some insight. Factors B and A cover some similar network structures, such as decreasing hub-to-hub connectivity. The lower value for Factor B could be due to the presence of Factor A leaving Factor B, in the structural, to focus on the betweenness of lower degree nodes where Factor A has less impact. Factor A is present in the structural networks and absent in the functional networks. This indicates that it is a priority in the structural to decrease hub-to-hub connectivity, but this is not a significant priority in the functional.

Factor S is present in the functional networks and absent in the structural networks. The overall pattern of the factors so far indicates a movement towards greater modularity, specifically with factors like Factors

T, B, and $D2$, which drive greater segmentation and clustering. Thus, Factor S would be in harmony with these movements and would perhaps guide them towards the already established subnetworks rather than promoting general modularity. The absence of this factor in the structural is indicative of a network less concerned with the established subnetwork structure. Noting that these subnetworks are, by definition, functional subnetworks, this makes sense.

In the subnetworks, the presence of Factors D^S and B^S in the functional models suggests some dynamics inside the subnetworks not particularly present in the structural subnetworks. This, in combination with the presence of Factor S, suggests that the functional networks experience significant subnetwork changes over time.

Overall, these networks seem to promote modularity and local efficiency and deter long-range connectivity over time. In the functional, the promotion of modularity is focused on the established subnetworks where there is a deterrent for betweenness. In the structural, the deterrent of long-range connectivity is stronger, and the networks uniquely deter hub-to-hub connectivity. The next section will explore the difference in the estimated factor weights across impairment groups, sex, and age for the functional and structural networks.

7.3 Factor Weight Demographic Results

This section will analyze the impact of demographic measures such as impairment group, sex, and age on the factor weights. In order to understand the differences between impairment groups, a series of weighted t-tests were conducted to see if the mean of the control was significantly different than the means of the impairment groups. The control group, blue in the graphs, are the individuals with low CDR-SB scores. The impairment group, red in the graphs, is the combination of the mild impairment and significant impairment individuals. Weighted t-tests were also run between the control and the mild impairment group (light red) and between the control and the significant impairment group (dark red). A weighted t-test was run between males (bright green) and females (bright pink), and a weighted 2-way ANOVA was used with impairment, sex, and their interaction. This was done for the full impairment group and the mild impairment group. The number of significant impairment individuals is low so ANOVAs between those groups was not conducted. For the ANOVA, the graphs from left to right are male controls (light blue), male impairment (green), female controls (purple), and female impairment (dark pink). Individual weighted t-tests were conducted between these groups to further understand the interactions. Finally, we fit weighted linear regression models with predictors for age, impairment group, and their interaction. Age was mean-centered to aid interpretation, such that the main effect of impairment tested group differences at the average age, the main effect of age reflected the age slope within the control group, and the interaction tested whether age-related changes

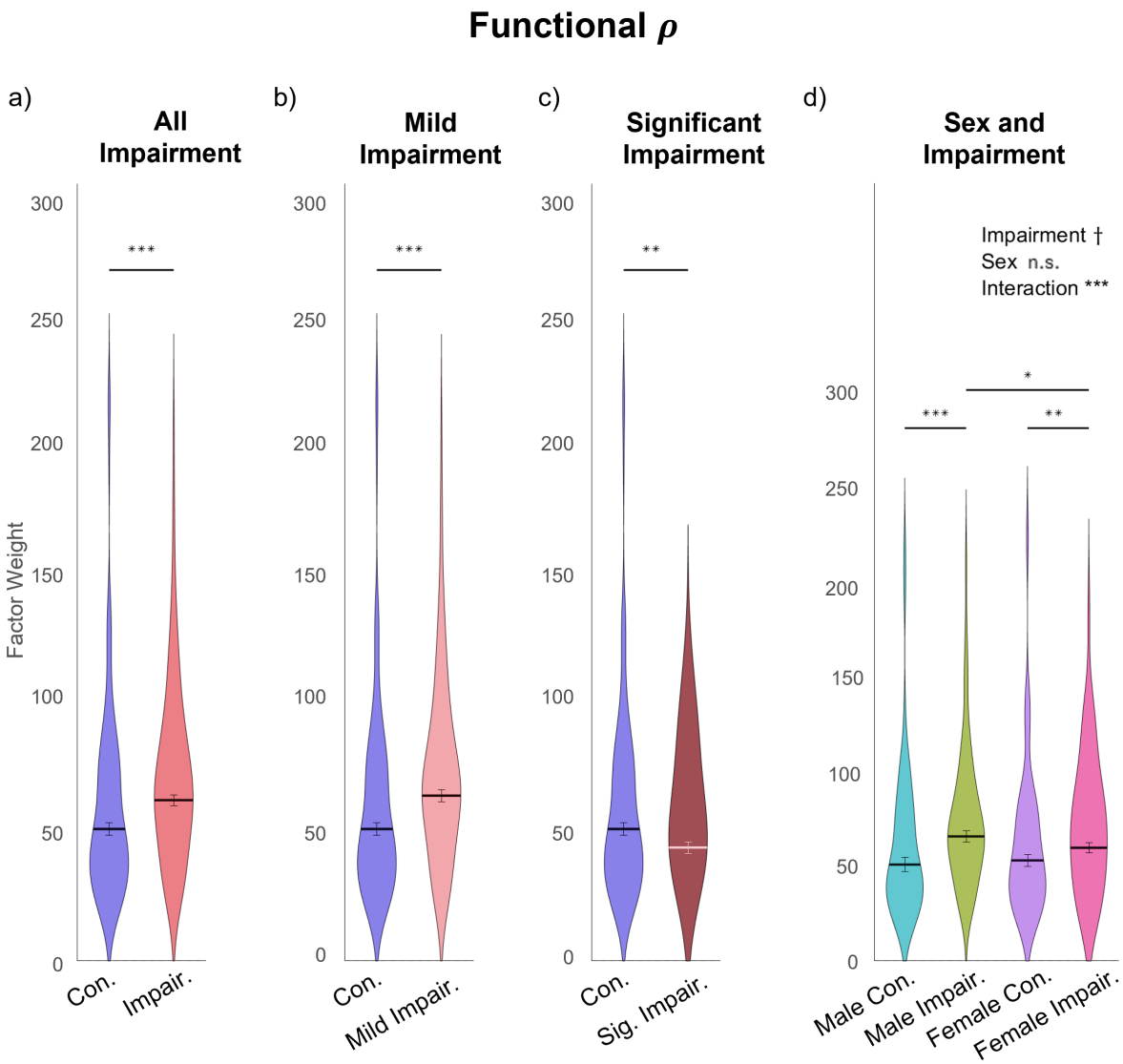

Figure 7.6: **Functional rate comparisons.** These graphs show the differences between demographic groups for the rate in the functional networks. Figure (a) shows a higher rate in the impairment group (red) compared to the control group (blue), $p = 3 \times 10^{-8}$. Figure (b) shows a higher rate in the mild impairment group (light red) compared to the control group (blue), $p = 2 \times 10^{-7}$. Figure (c) shows a lower rate in the significant impairment group (dark red) compared to the control group (blue), $p = 0.007$. Figure (d) shows a minor impairment effect, $p = 0.06$, and an impairment-sex interaction effect, $p = 3 \times 10^{-4}$ in a 2-way ANOVA. It shows a lower rate in the male control group (light blue) compared to the male impairment group (green), $p = 2 \times 10^{-7}$, a lower rate in the female control group (purple) compared to the female impairment group (dark pink), $p = 0.002$, and a higher rate for the male impairment group (green) compared to the female impairment group (dark pink), $p = 0.03$.

differed between groups. In addition, individual weighted correlations were used to quantify associations between continuous variables, and fitted regression trend lines are shown in the figures to illustrate the direction and magnitude of effects. Together, these tests allowed us to evaluate both group-level differences and the influence of demographic variables on the factor weights. The current reported results do not make adjustments for repeated measures due to the longitudinal data and further analyses such as mixed-effects models could be conducted to assess the impact of repeated measures. In the reporting of these tests, only informative graphs were included. The remaining tests were either not significant or reiterated information contained in the included graphs (like showing little difference between the impairment ANOVA and the mild impairment ANOVA).

7.3.1 Functional Results

The functional rate of change (ρ) is consistently higher in the impairment group compared to the control, specifically in the mild impairment group (Figures 7.6a and 7.6b). The most significantly impaired individuals actually saw a decline in their rates compared to controls (Figure 7.6e). Individuals with mild impairment have functional networks that are changing the most rapidly, but this acceleration declines in significant impairment. These differences are modulated by sex, with males showing a larger difference between the control and impairment group (Figure 7.6).

In the subnetworks, some subnetworks show consistency with the full network rate results and others do not, suggesting that the rates of change are heterogeneous across the brain. Higher rates for the overall impairment group are found in the SN and DMN (Figures 7.7h and 7.7k), while lower rates for the impairment group are found in the VN and FPN (Figures 7.7a and 7.7d). The most significantly impaired individuals have rate behavior that is inverse of the subnetwork's overall trend in the VN and DMN (Figures 7.7b and 7.7l) while the FPN and SN show consistency with that subnetwork's overall impairment trend (Figures 7.7e and 7.7i). The FPN and DMN both show stronger impairment differences to rate in females (Figures 7.7g and 7.7n) while the VN and SN show stronger impairment differences in rate in males (Figures 7.7c and 7.7j).

When discussing factors weights in the following sections, more weight will refer to a higher absolute value of the factor weight. This refers to how impactful a factor is rather than the overall number of the weight since some weights are negative and others are positive. The dotted line at zero orients the graph based on whether the weights are mostly positive or mostly negative.

As shown in Figure 7.8a, Factor Degree (D) in the impairment group has a smaller negative weight than the control group. Along with the pattern of the rate, for individuals with mild impairment, the functional

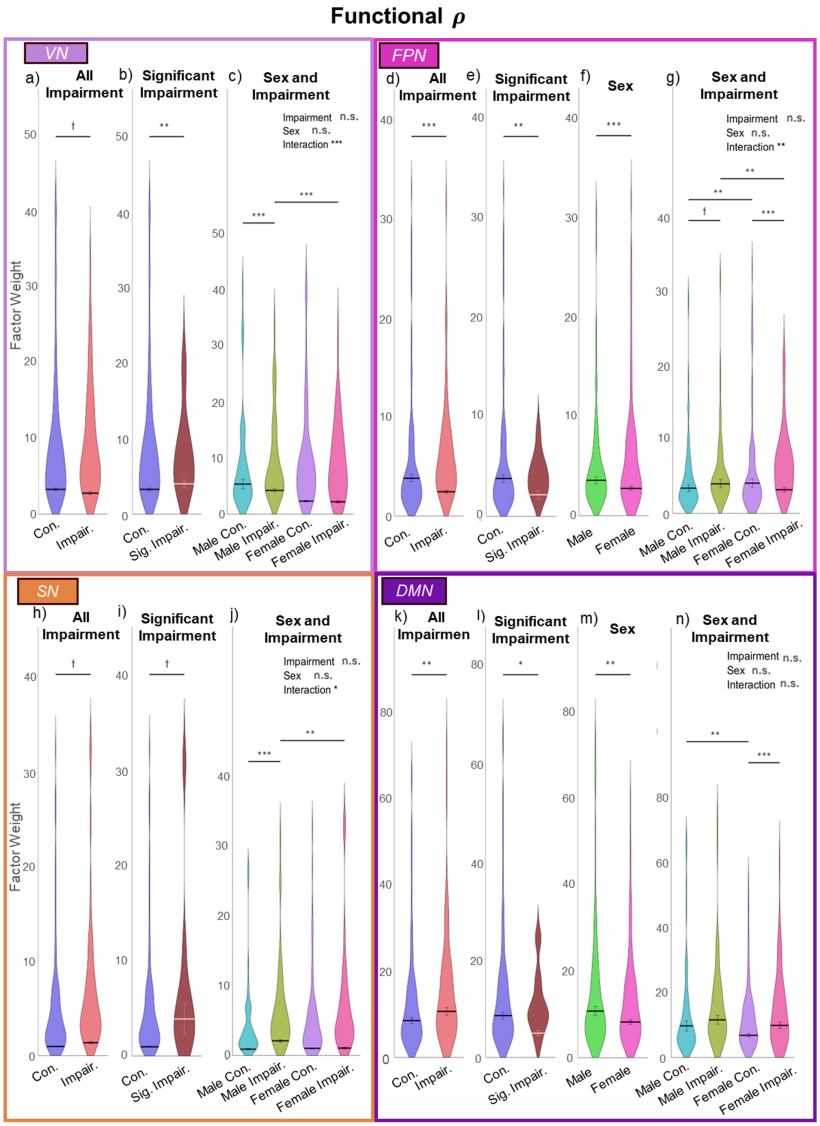

Figure 7.7: **Functional rate for subnetworks comparisons.** These graphs show the differences between demographic groups for the rate in the functional subnetworks. Figure (a) shows a trend of lower rates in the impairment group, $p = 0.07$, in the VN. Figure (b) shows a higher rate in the significant impairment group, $p = 0.003$, in the VN. Figure (c) shows an impairment-sex interaction effect, $p = 1 \times 10^{-4}$, lower rates in impairment group among males, $p = 1 \times 10^{-6}$, and lower rates for females among the impairment group, $p = 2 \times 10^{-5}$, in the VN. Figure (d) shows a lower rate in the impairment group, $p = 3 \times 10^{-8}$, in the FPN. Figure (e) shows a lower rate in the significant impairment group, $p = 0.002$, in the FPN. Figure (f) shows a lower rate for females compared to males, $p = 1 \times 10^{-4}$, in the FPN. Figure (g) shows an impairment-sex interaction effect, $p = 0.006$, a trend of higher rates in the impairment group among males, $p = 0.05$, lower rates in the impairment group among females, $p = 3 \times 10^{-14}$, an increase in the rate for females among the control group, $p = 0.008$, and a decrease for females among the impairment group, $p = 0.003$, in the FPN. Figure (h) shows a trend of higher rates for the impairment group, $p = 0.06$, in the SN. Figure (i) shows a trend of higher rates for the significant impairment group, $p = 0.06$, in the SN. Figure (j) shows an impairment-sex interaction effect, $p = 0.01$, a higher rate in the impairment group among males, $p = 1 \times 10^{-4}$, and a lower rate for females among the impairment group, $p = 0.008$, in the SN. Figure (k) shows a higher value in the impairment group, $p = 0.005$, in the DMN. Figure (l) shows a lower value in the significant impairment group, $p = 0.02$, in the DMN. Figure (m) shows a lower value in females, $p = 0.002$, in the DMN. Figure (n) shows lower rates in females among controls, $p = 0.001$, and higher rates in the impairment group among females, $p = 1 \times 10^{-4}$, in the DMN.

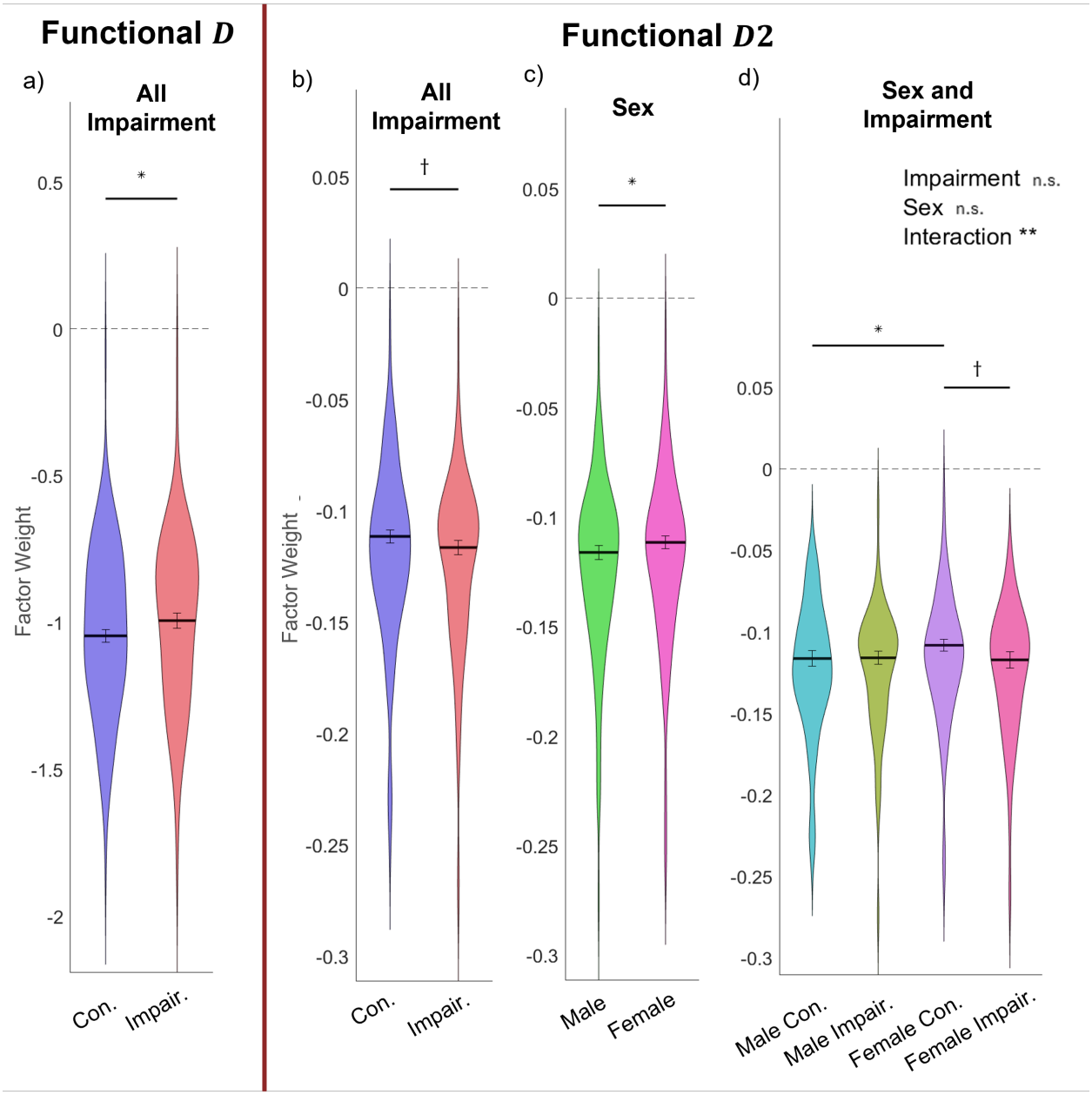

Figure 7.8: **Functional weight comparisons for Factor Degree and Factor Distance 2.** These graphs show the differences between demographic groups for Factor Degree (D) (left) and Factor Distance 2 ($D2$) (right) in the functional models. Figure (a) shows a less negative value of Factor D in the impairment group (red) compared to the control group (blue), $p = 0.04$. Figure (b) shows a trend towards a more negative value for Factor $D2$ in the impairment group (red) compared to the control group (blue), $p = 0.08$. Figure (c) shows a less negative value for Factor $D2$ in the female group (bright pink) compared to the male group (bright green), $p = 0.03$. Figure (d) shows an impairment-sex interaction effect, $p = 0.01$, a difference between the male control group (light blue) and female control group (purple), $p = 0.03$, and a weak trend between the female control group (purple) and female impairment group (dark pink), $p = 0.08$ for Factor $D2$.

networks are changing more rapidly, and connections are not as expensive as they are in the control networks. This demonstrates greater randomness in the network changes in the mild impairment group.

Figure 7.8b, 7.8c, and 7.8d shows an interdependency in Factor Distance 2 ($D2$) where female controls show a smaller weight compared to male controls (Figure 7.8d) and a weakly significant trend of higher values compared with females with impairment (Figures 7.8d). This suggests that because females have a lower baseline of segmenting communities and impairment may pose a disruption in this pattern.

A slightly different pattern is seen in Figures 7.9a and 7.9b where Factor Same Subnetwork (S) has a lower positive weight in females compared to males specifically in the impairment group (Figures 7.9a and 7.9b). A significant difference between the female controls and the females with impairment, combined with the Factor $D2$ results, suggests that the disease progression for females with impairment sees a disruption in the modular structure and network segmentation.

This result may also clarify the results seen in Figure 7.2 where it is unknown if the significant inclusion disparity is due to impairment, sex, or age group. If the weight for a factor is closer to zero, this may mean that factor is less likely to appear as a factor after the hypothesis-building procedure. In this case, females showed lower weights for Factor S, but perhaps a higher instance of finding Factor S after the hypothesis-building procedure and a lower value in impairment—this could indicate that the primary driver of the inclusion disparity is impairment rather than sex or age. Further exploration of this subject with a larger Hypothesis Group is suggested for future research.

One can observe Factor S as a general measure of the intra-network connectivity in the subnetworks. The subnetworks Factor Degree (D^S) provides further detail into any heterogeneity in the intra-network connectivity of individual subnetworks. Only one network, the FPN, showed significant differences on demographic measures for Factor D^S. A trend towards a more positive weight in the impairment group was found with weak significance, but the pattern is much stronger between control and diagnosed females (Figures 7.9c and 7.9d). This extends the pattern of females with impairment showing a disrupted modular structure.

The behavior of the functional subnetworks can be studied further by exploring the other two factors that make up the subnetwork hypothesis. The subnetwork Factor Betweenness (B^S) showed some results specifically among the mild impairment group. In the DMN, the general trend of more negative prioritization of Factor B^S in the mild impairment group was found to be particularly prominent in the female groups (Figures 7.10a and 7.10b). The VN demonstrated interaction results with the negative priority increasing among females with impairment, consistent with the DMN, but decreasing among males with impairment (Figures 7.10c and 7.10d). There was also an interaction effect on the mild impairment difference with age in the VN, where a greater difference is shown early in the aging process (Figure 7.10e). These both may explain the lack of result in Figure 7.10c. These results suggest a disruption in the subnetwork hub

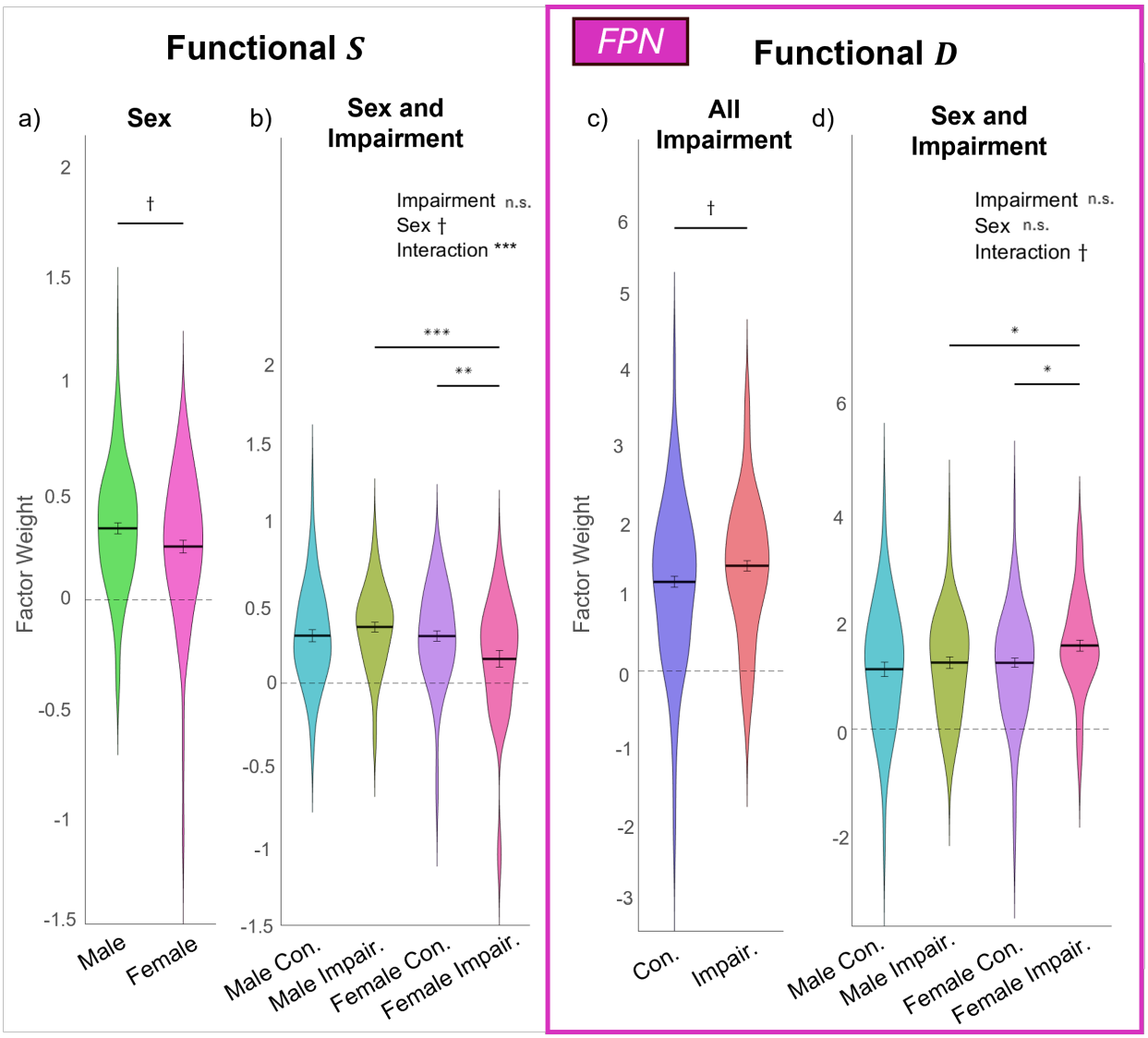

Figure 7.9: **Functional weight comparisons for Factor Same Subnetwork and subnetwork Factor Degree.** These graphs show the differences between demographic groups for Factor Same Subnetwork (S) in the functional networks and for Factor Degree (D^S) in the functional subnetworks. Figure (a) shows a somewhat less positive value in the female group (bright pink) compared to the male group (bright green), $p = 0.05$. Figure (b) shows a (not really significant) sex effect, $p = 0.09$ and a significant impairment-sex interaction effect, $9 \times 10^{-}5$, and shows a difference between the male impairment group (green) and female impairment group (dark pink), $p = 5 \times 10^{-}5$, and a difference between the female control group (purple) and female impairment group (dark pink), $p = 0.005$. Figure (c) shows a trend towards a more positive value in the impairment group (red) compared to the control group (blue), $p = 0.06$, in the FPN. Figure (d) shows a weak interaction effect, $p = 0.07$, between impairment group and sex, and shows a difference between the male impairment group (green) and female impairment group (dark pink), $p = 0.003$, and a difference between the female control group (purple) and female impairment group (dark pink), $p = 0.04$, in the FPN.

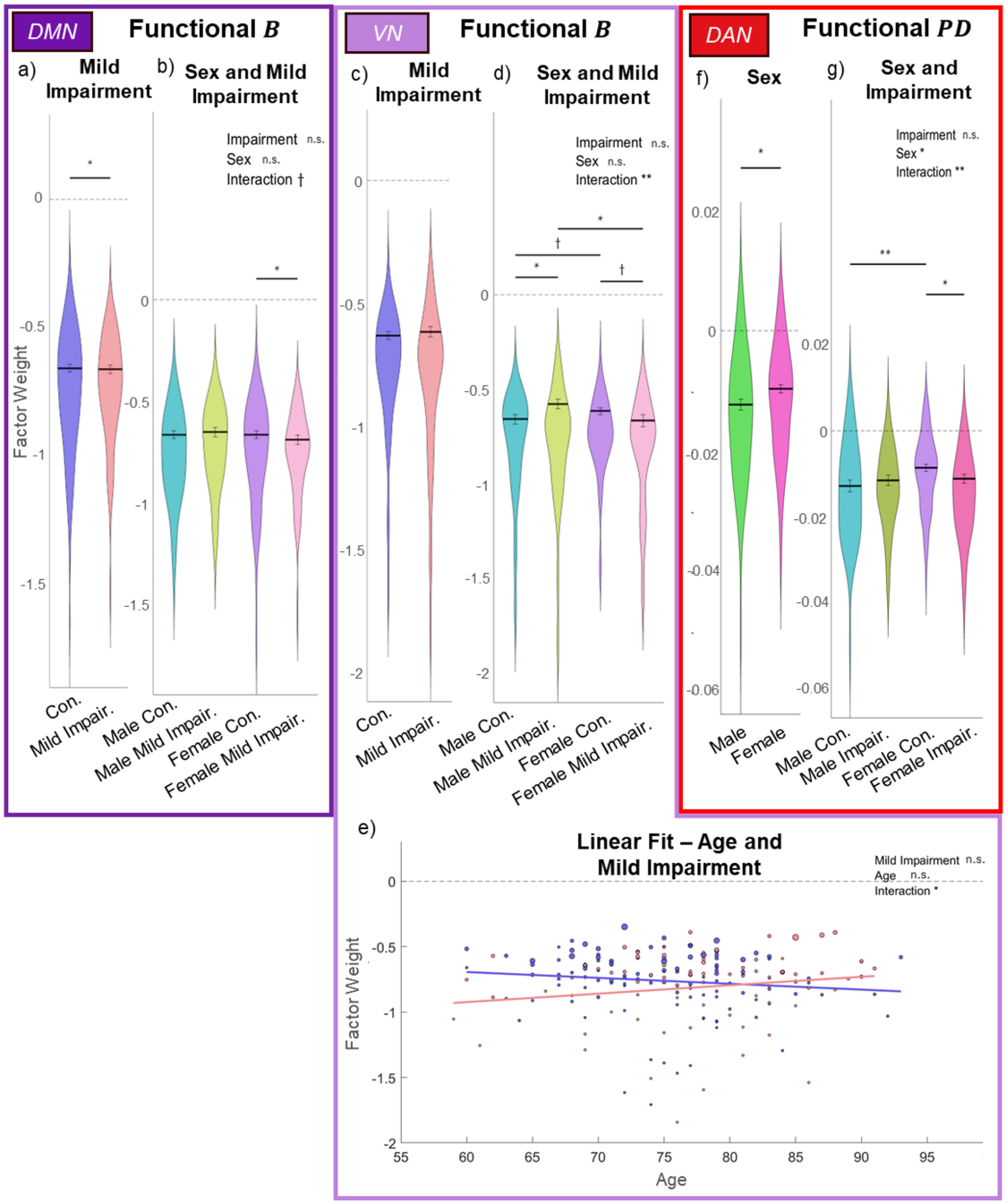

Figure 7.10: **Functional weights for subnetwork Factor Betweenness and subnetwork Factor Physical Distance.** These graphs show the differences Factor Betweenness and Factor Physical Distance in the functional subnetworks. (a) shows a difference for subnetwork Factor B^S in the mild impairment group, $p = 0.04$, in the DMN. (b) shows a (not significant) impairment-sex interaction effect, $p = 0.09$, for Factor B^S, and shows a difference between impairment among females, $p = 0.02$, in the DMN. (c) shows no significant difference between the mild impairment and controls for Factor B^S in VN. (d) shows an interaction effect, $p = 0.003$, between mild impairment group and sex for Factor B^S, and shows a difference between sexes among controls, $p = 0.08$, and among the impairment group, $p = 0.02$. It shows a difference between impairment groups among males, $p = 0.02$, and among females, $p = 0.06$, in the VN. (e) shows a mild impairment-age interaction effect, $p = 0.03$, for Factor B^S in the VN. (f) shows a higher value for Factor PD^S in females, $p = 0.02$, in the DAN. (g) shows a sex effect, $p = 0.04$, an impairment-sex interaction effect, $p = 0.002$, for Factor PD^S, and shows a difference between sexes among the control, $p = 0.009$, and a difference among impairment group among females, $p = 0.02$, in the DAN.

connectivity with mild impairment.

The final subnetwork factor is Factor Physical Distance (PD^S). The DAN showed significant sex differences where males consistently more negatively prioritize physical distance compared to females even as females in the impairment group show a higher negative prioritization than their control counterparts (Figures 7.10f and 7.10g). The large sex difference in the control group suggests that a larger negative priority for males compared to females is the baseline in the DAN. This may be influenced by the differences in the size of the brain between males and females [van Eijk 2021] especially for a widespread subnetwork like the DAN [Yeo 2011]. Because this can be seen as a measure of the cost of long-range connections, the larger brains of males may explain why building long-range connections is more expensive[1]. However, this result was only seen in the DAN, so further exploration may be needed to better understand this phenomenon.

Overall, the evidence in these results is that the changes to functional networks are particularly impacted by impairment and sex. Mild impairment often behaves differently from both control and significant impairment. Mildly impaired networks change more rapidly with changes distributed unevenly in the various subnetworks. Additionally, between the modularity-related full network factors and the subnetwork factors, females with impairment demonstrate a disruption in the subnetworks that is somewhat absent for males.

7.3.2 Structural Results

Similar to the functional results, the structural networks demonstrated an increased rate of change (ρ) in the impairment, and particularly the mild impairment, group compared to controls (Figures 7.11a and 7.11b). This difference is similarly most pronounced among males (Figure 7.11d). Once again, however, the significant impairment group shows an inverse trend with lower rates in the significantly impairment group compared to the control group (Figure 7.11c). Unique to the structural networks, age plays a role in the rate. The rate decreases with age in the mild impairment group. This trend amplifies the difference between mild impairment and control in early aging and demonstrates that the difference declines with the age of the participant (Figure 7.11e).

The rate for the subnetworks in the structural shows strong consistency with the full network results. Faster rates of change in the impairment group were found in the DAN, SN, and FPN (Figures 7.12a, 7.12d, and 7.12g). The subnetworks that found differences between the impairment groups found stronger differences among females, differing from the male-dominated differences in the full network results (Figures 7.12c, 7.12f, 7.12i, and 7.11d). Despite the differences seen in the full network rate, the SN and FPN showed the significant impairment group to have a higher rate compared to the controls, suggesting that other

[1]The coordinate system used in this study is the same for all individuals, and brain size is not a considered variable. Despite this, the implication about cost can still be extrapolated.

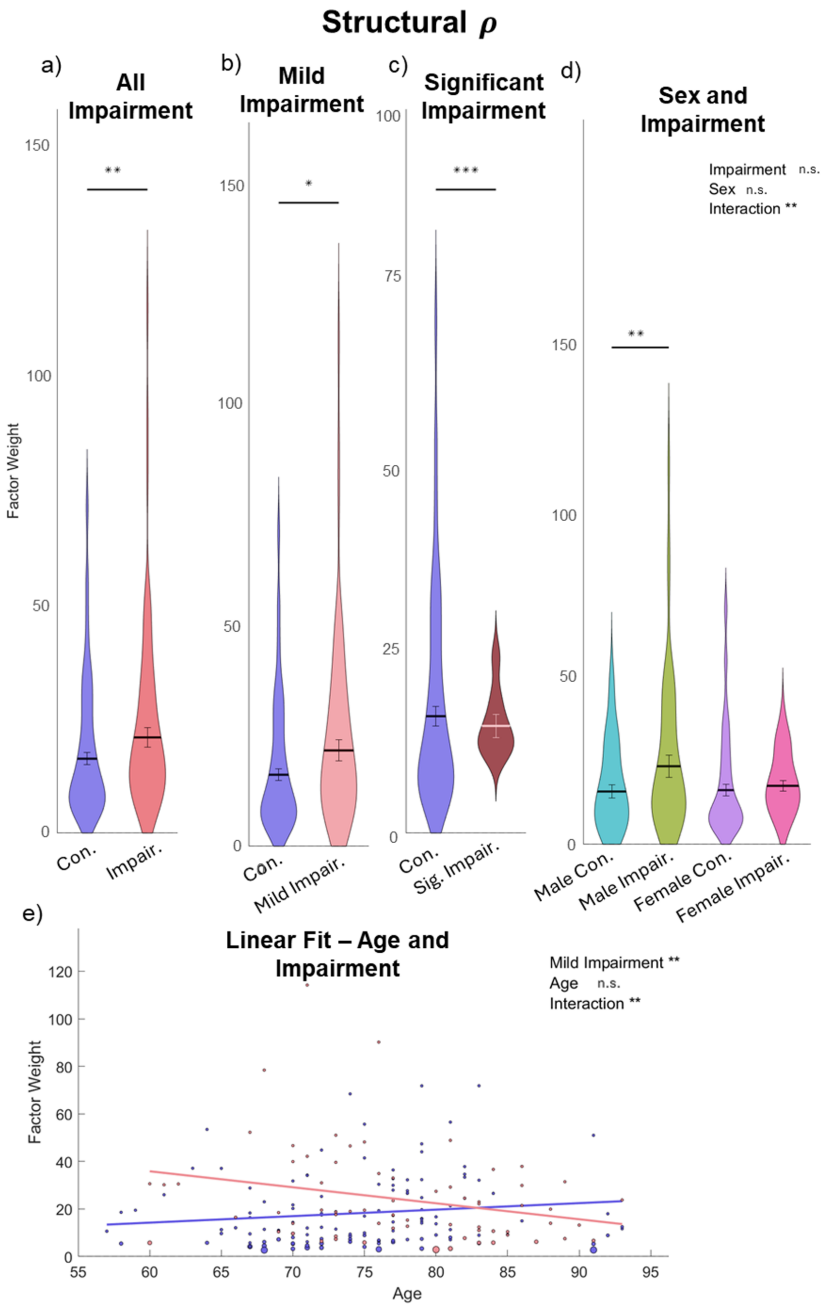

Figure 7.11: **Structural rate comparisons.** These graphs show the differences between demographic groups for the rate in the structural networks. Figure (a) shows a higher rate in the impairment group (red) compared to the control group (blue), $p = 0.006$. Figure (b) shows a higher rate in the mild impairment group (light red) compared to the control group (blue), $p = 0.02$. Figure (c) shows a lower value in the significant impairment group (dark red) compared to the control group (blue), $p = 2 \times 10^{-4}$. Figure (d) shows an impairment-sex interaction effect, $p = 0.008$, and a difference between the male control group (light blue) and male impairment group (green), $p = 0.001$. Figure (e) shows an mild impairment effect, $p = 0.008$, and an mild impairment-age interaction effect, $p = 0.005$ for a weighted linear regression model. It also shows a weak negative correlation with age in the mild impairment group (light red) ($R^2 = 0.03$, $p = 0.02$).

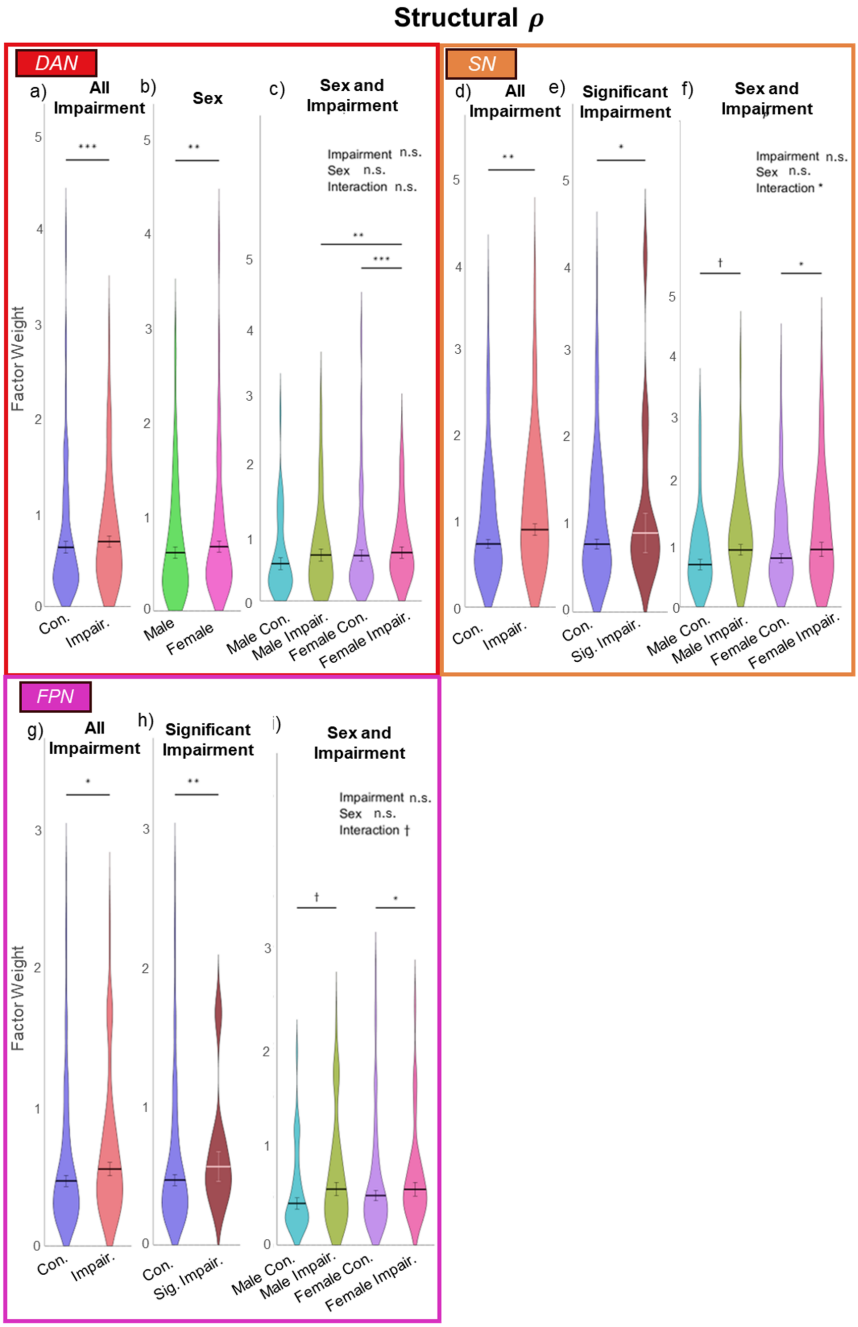

Figure 7.12: **Structural rate for subnetworks comparisons.** These graphs show the differences between demographic groups for the rate in the structural subnetworks. Figure (a) shows a higher rate in the impairment group compared to the control group, $p = 1 \times 10^{-6}$, in the DAN. Figure (b) shows a higher value in the female group compared to the male group, $p = 0.002$, in the DAN. Figure (c) shows a higher rate for the impairment group among females, $p = 2 \times 10^{-5}$, and a high rate for females among the impairment group, $p = 0.003$, in the DAN. Figure (d) shows a higher value in the impairment group compared to the control group, $p = 0.005$, in the SN. Figure (e) shows a higher value in the significant impairment group compared to the control group, $p = 0.03$, in the SN. Figure (f) shows a impairment-sex interaction effect, $p = 0.03$, a trend of higher rates in the impairment group among males, $p = 0.07$, and a higher rate in the impairment group among females, $p = 0.01$, in the SN. Figure (g) shows a higher value in the impairment group compared to the control group, $p = 0.01$, in the FPN. Figure (h) shows a higher value in the significant impairment group compared to the control group, $p = 0.009$, in the FPN. Figure (i) shows a weak impairment-sex interaction effect, $p = 0.06$, a higher rate in the impairment group among males, $p = 0.05$, and among females, $p = 0.04$, in the FPN.

subnetworks may be contributing to the lower full network rate. Of course, that heterogeneity requires further research due to the small sample size of the significant impairment group in this study.

Once again mirroring the functional results, the negative prioritization of Factor Degree (D) trends towards decreasing in the impairment group compared to the control group (Figure 7.13a). However, while in the functional, the difference was most pronounced in the mild impairment group, the structural shows a difference more pronounced in the significant impairment group (Figures 7.13b and 7.13c). The mild impairment differences may be absent due to the intersection with age that suggests that this factor weight in the mild impairment group becomes more negative with time meaning any lower prioritization in the mild impairment group compared to the control all but disappears by about 78 years (Figure 7.13d).

Factor Transitive Triads (T) has a significantly lower positive priority in the impairment group compared to the control (Figure 7.13e). The effect, once again, is most pronounced in the early stages of aging (Figure 7.13g). This suggests that impairment is related to a decreased priority of clustering on the network. This difference is also most pronounced in females (Figure 7.13f). This may indicate some consistency in the female-specific modularity disruption seen in the functional models.

As seen in Figure 7.14a, Factor 4-Cycles ($C4$) shows a decrease in negative prioritization in the impairment group. This factor follows a similar age-related pattern to the other structural factors, with a decrease in the differences between groups with age (Figure 7.14b). The impairment group sees an increase in negative prioritization with age. This suggests that the impairment group sees a lower prioritization of local efficiency that improves with age.

Factor Assortativity (A), in Figures 7.14c and 7.14d, shows a decrease in the negative prioritization in the impairment group, especially among males, trending towards zero. This suggests that males with impairment are not preventing hub-to-hub connectivity as well as the control group.

The only factor found as part of the subnetwork hypothesis for the structural networks was Factor Physical Distance (PD). In the SMN and SN, a lower negative priority in the significant impairment group was found (Figures 7.15b and 7.15e), likely impacting the overall impairment group (Figures 7.15a and 7.15d). The result was most prominent among males (Figures 7.15c and 7.15f). This indicates that, in significant impairment, the prevention of long-range connectivity is less of a priority compared to controls. In the conversation about connectivity cost of long-range connections, it may be interpreted that in these subnetworks, which are considerably less widespread than, say, the DMN [Yeo 2011], the significant impairment group is wasting connectivity resources on expensive long-range connections, but only within those subnetworks.

Overall, the structural networks seem to be more strongly impacted by impairment compared to the functional, as a greater number of factors are impacted. Except for rate, the significant impairment group shows greater and more consistent impacts compared to controls in the structural. There are some impairment

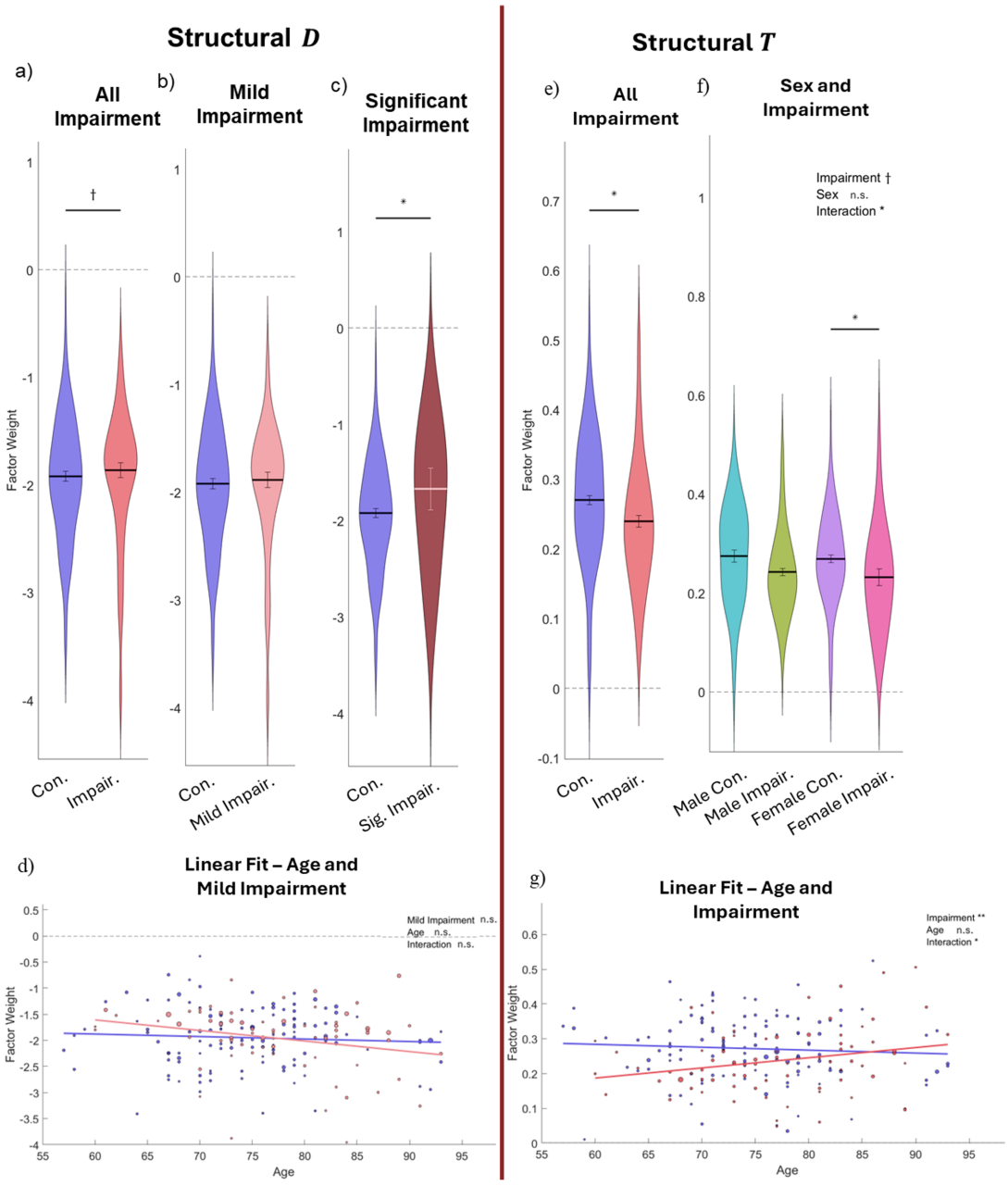

Figure 7.13: **Structural weight comparisons for Factor Degree and Factor Transitive Triads.** These graphs show the differences between demographic groups for Factor Degree (D) (left) and Factor Transitive Triads (T) (right) in the structural networks. Figure (a) shows a trend towards a less positive value in the impairment group (red) compared to the control group (blue), $p = 0.08$, for Factor D. Figure (b) shows no significant difference between the mild impairment group (light red) compared to the control group (blue) for Factor D. Figure (c) shows a less positive value in the significant impairment group (dark red) compared to the control group (blue), $p = 0.04$, for Factor D. Figure (d) shows a weak negative correlation with age in the mild impairment group ($R^2 = 0.03$, $p = 0.02$) for Factor D. Figure (e) shows a less positive value in the impairment group (red) compared to the control group (blue), $p = 0.01$, for Factor T. Figure (f) shows a minor impairment effect, $p = 0.06$, and an impairment-sex interaction effect, $p = 0.01$ on a 2-way ANOVA. It shows a higher value in the female control group (purple) compared to the female impairment group (dark pink), $p = 0.02$ for Factor T. Figure (g) shows an impairment effect, $p = 0.004$, (at average age) and an impairment-age interaction effect, $p = 0.03$ on a weighted linear regression model. It shows a weak positive correlation with age in the impairment group ($R^2 = 0.03$ $p = 0.03$).

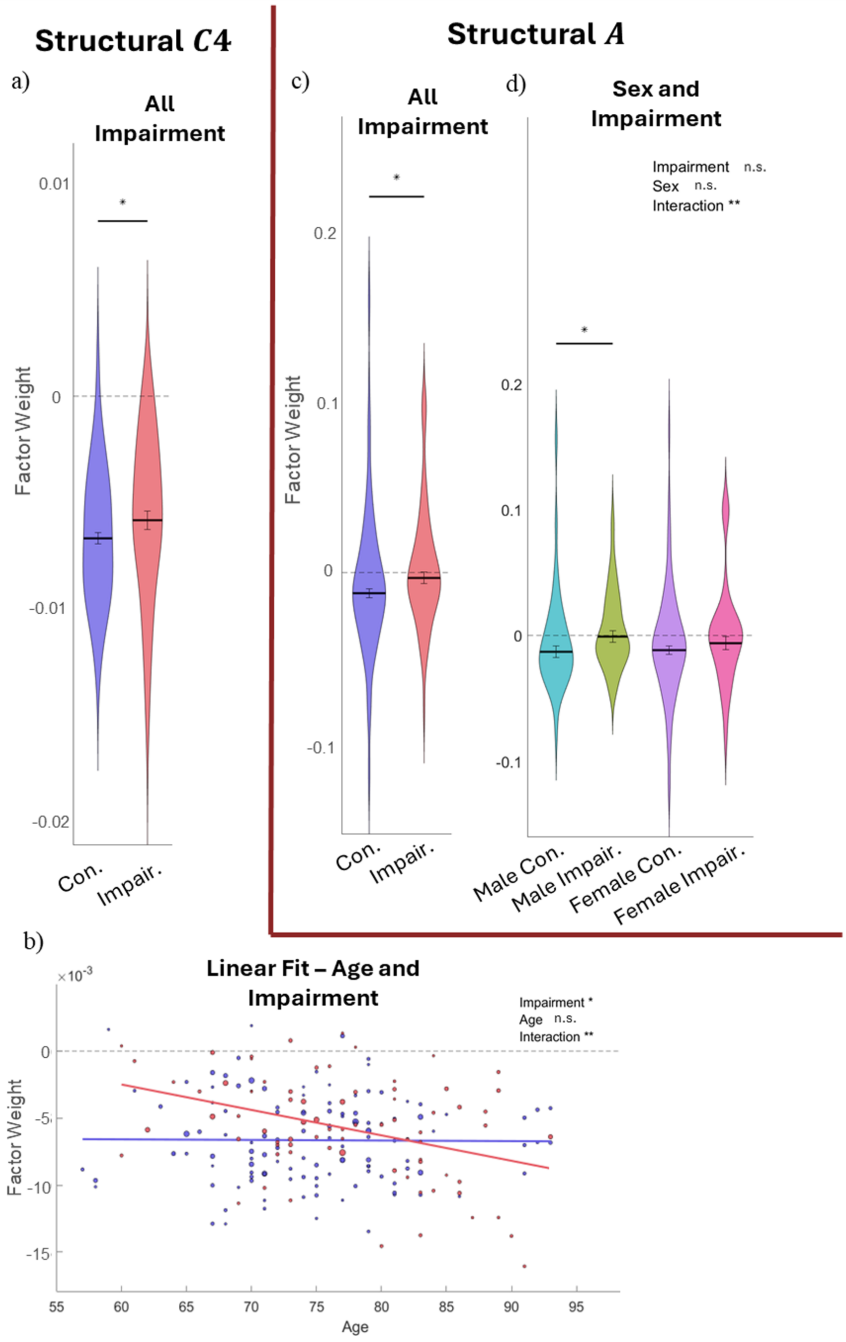

Figure 7.14: **Structural weight comparisons for Factor 4-Cycles and Factor Assortativity.** These graphs show the differences between demographic groups for Factor 4-Cycles ($C4$) (left) and Factor Assortativity (A) (right) in the structural networks. Figure (a) shows a less negative value in the impairment group (red) compared to the control group (blue), $p = 0.04$, for Factor $C4$. Figure (b) shows a Factor $C4$ impairment effect (at the average age), $p = 0.01$, and an impairment-age interaction effect, $p = 0.003$ on a weighted linear regression model. It also shows a weak negative correlation with age in the impairment group ($R^2 = 0.07$, $p = 2 \times 10^{-4}$). Figure (c) shows a less negative value in the impairment group (red) compared to the control group (blue), $p = 0.02$, for Factor A. Figure (d) shows a Factor A significant impairment-sex interaction effect, $p = 0.004$, and a higher value for the male control group (light blue) compared to the male impairment group (green), $p = 0.04$.

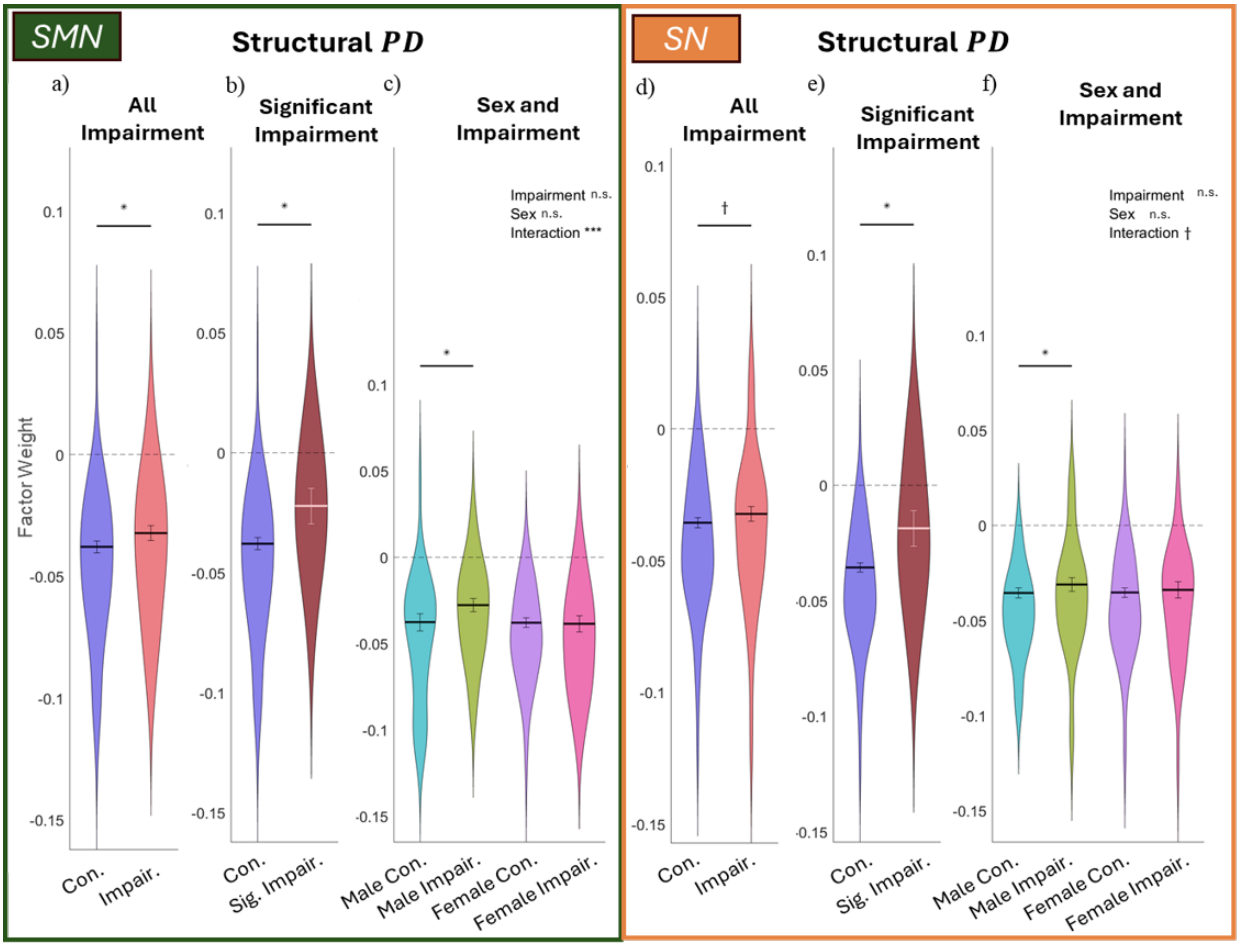

Figure 7.15: **Structural weight comparisons for subnetwork Factor Physical Distance.** These graphs show the differences between demographic groups for Factor Physical Distance (PD^S) in the structural subnetworks. Figure (a) shows a less negative value in the impairment group (red) vs the control group (blue), $p = 0.04$, in the SMN. Figure (b) shows a less negative value for the significant impairment group (dark red) compared to the control (blue), $p = 0.04$, in the SMN. Figure (c) shows a significant impairment-sex interaction effect, $p = 4 \times 10^{-4}$, and a lower value for the male control group (light blue) compared to the male impairment group (green), $p = 0.03$, in the SMN. Figure (d) shows a non-significant trend between the impairment group (red) compared to the control group (blue), $p = 0.09$, in the SN. Figure (e) shows a less negative value for the significant impairment group (dark red) compared to the controls (blue), $p = 0.01$, in the SN. Figure (f) shows an impairment-sex interaction effect, $p = 0.05$, and a lower value for male controls (light blue) compared to males with impairment (green), $p = 0.03$, in the SN.

differences that are more prominent in males, suggesting there may be some greater connection between structural decline and cognitive ability in males. The impairment group shows a consistent pattern of strong differences in early age that trend toward the control in later adulthood. The most consistent and striking result is the tendency of factors in the structural models to have weights closer to zero in the impairment groups. This indicates a trend toward randomness in the connectivity of the impaired structural networks over time.

Chapter 8

Discussion

In this project, we developed a set of models of network change for functional and structural brain networks in aging by applying the stochastic actor-oriented model (SAOM) as the framework for these models. The models propose a dynamical explanation of aging trends through the prioritization of certain factors—these factors drive change on the network. The models found in this study generally promote modularity and local efficiency while preventing long-range connectivity. The general models, as well as the differences between factor weights in different demographic groups, contribute significantly to the emerging picture of aging grounded in complex interactions and dynamics. The careful consideration of the interpretation of these models is essential for placing them in the context of our current understanding of the aging brain. In this section, I will discuss the results in terms of key interpretive hypotheses and place them in the context of the literature.

8.1 The Maintenance Hypothesis

To begin understanding these models and their promotion of modularity, efficiency, and local-range connectivity, a central question emerges that will shape the interpretation and future applications of these models. In a population of aging adults with and without impairments, do the models found in this project represent an overall decline that occurs with age or the maintenance of established brain structure?

We argue that the overall models generally demonstrate maintenance rather than decline and we will refer to this interpretation as "the maintenance hypothesis." This interpretation is most in line with the model results and is supported by the current literature. The maintenance hypothesis is the interpretation that these models promote the maintenance of established structures in the brain and defend key topology from a trend towards randomness through changes to local connectivity.

Both structural and functional brain networks have shown a small-world architecture [Bassett 2006, Hagmann 2007, Bullmore 2009, Deco 2011] characterized by high clustering and a short average path length. A positive weight for Factor Transitive Triads (T) is an indication of the promotion of clustering, and, while there are no global measures in this model (being node-oriented as it is), a negative weight for Factor Distance 2 ($D2$) and a negative weight for Factor 4-Cycles ($C4$) promote local efficiency. Brain networks have also been shown to have high modularity with some consistent community structure [Meunier 2010, Sporns 2016]. The promotion of modularity is clear in these results with a positive weight for the Factor T, a negative weight for the Factor Betweenness (B), a negative weight for the Factor $D2$, and, in the functional, a positive weight for the Factor Same Subnetworks (S) which suggests greater segmentation between subnetworks. This suggests that the factors in the network are promoting modularity. Lastly, the promotion of short-range connectivity and local hops across the brain is in line with consistent patterns of connectivity in previous literature especially in structural networks [Ercsey-Ravasz 2013, Bullmore 2012, Roberts 2016, Supekar 2008]. These results are in line with the maintenance hypothesis, as the key structures known to appear in brain networks are specifically and consistently promoted in these models.

By promoting the network structures that are consistently seen in the literature, the act of maintenance in the brain has been seen consistently on various scales. There have been many studies, for instance, that show consistency of large scale topology regardless of task, across individuals, across the lifetime, and across species [Betzel 2014, Chan 2014, Gratton 2018, Bassett 2011, Chklovskii 2004, Kaiser 2011]. Beyond this, some studies have explicitly discussed the brain's homeostatic tendencies [Turrigiano 2012], or model with maintenance structures to prevent over- or under-connectivity [Litwin-Kumar 2014, Zenke 2013, Rocha 2018]. It is, therefore, likely that long-term brain dynamics will involve the homeostatic maintenance that is observed in this project.

Recall that the stochastic actor-oriented models are not deterministic and are, as the name implies, stochastic. Randomness is a key component of the behavior of the model. As a result of this randomness and the limited nature of changes in the network, nodes have the opportunity to act beyond of the single most optimal interest of their own satisfaction and often do. The randomness reflects the noisy nature of the brain. Previous studies reviewing the short-term behavior of brain networks suggest that there is a significant amount of noisy fluctuation in brain activity [Honey 2007, Faisal 2008, Kiviniemi 2008, Deco 2009, Jafari 2019, Ye 2024], it follows that, in the long-term, there may be noisy fluctuations in network connectivity.

Recall, also, that these models are a framework of individual changes selected based upon a probability calculated from a linear combination of factors. The models are node-oriented and driven by individual node satisfaction. As a result, the model is not driven by the overall structure of the network, but by local structures. Often, due to the local connectivity, one node will be particularly impacted by a certain factor

while another node will be particularly impacted by a different factor, despite the fact that all the nodes have the same weight for each factor. Each node is looking out for its individual satisfaction within its connectivity; thus, changes to local connectivity are what is driving the whole network structure. Thus, the maintenance of large-scale network structures can be connected, through these models, to adjustments on the local level. This aligns with research on the emergence of large-scale connectivity from local connectivity [Bassett 2006, Xie 2021, Forrester 2020, Varier 2011, Kaiser 2011].

As a result of the stochasticity and node-orientation of SAOMs, there is no network structure where all the nodes will be completely satisfied and will no longer make changes. Conflict arises between individual nodes when changes to one node impact the satisfaction of another node. Conflict also arises between the priorities of different factors. For example, a negative weight for Factor Degree would suggest removing all connections, but, in combination with a positive weight for the Factor Transitive Triads, nodes may build connections if a triangle can be formed. These conflicts are a key feature of the SAOMs.

As an example, let us examine an SAOM with no factors. This indicates random change on the network—all nodes are equally likely to be selected and all choices for that node are equally likely. Regardless of the initial network structure, the overall network will trend towards a random architecture. The exact connectivity of this random network may be different, but the overall architecture is random. One can then extrapolate that models with factors may trend toward certain large-scale network architectures, but maintain a degree of variability for individual connections and significant noise through randomness and conflicts between factors and between nodes. All these behaviors of SAOMs suggest that a network driven by this model can stochastically approach states of ideal connectivity, but maintain noisy fluctuations and high variability. The maintenance hypothesis suggests that the initial network is already in a fairly satisfied state of global architecture, and the factors are serving to maintain the network in this general state rather than some other less ideal state. Previous research has shown significant inter-subject variability in the specific connectivity with consistent global structures in the network [Baldassarre 2012, Seghier 2018] indicating that one-to-one mapping would be an oversimplification of natural variability. Additionally, other studies found dynamics within-subjects, though this area requires further research, especially regarding functional adaptability and consistency of structure on short time scales or while performing tasks. [Shine 2016, Allen 2014, Hutchison 2013, Zalesky 2014].Thus, framing these SAOMs as describing fluctuations around a certain state lends further evidence to the maintenance hypothesis.

Recall, finally, that these networks are not originally binary networks, which means that the building or dissolving of connections in the network represent marginal changes to the weights of those connections above or below the 20% threshold. As a result, the interpretation of the models is even less dramatic than some of the social network interpretations.

If we were to make a social network analogy, we might view connections between nodes as a sliding scale of emotional intimacy in, say, a small workplace. You are likely to know everyone in your small workplace; however, the connection you have with certain individuals might be considered "friendship" while others may be better classified as "acquaintanceship." In this analogy, the top 20% of the closest coworkers are considered "friends" while the rest are not. Perhaps, a team-bonding activity increases the intimacy between most individuals on the network; the 20% rule still applies, so the threshold for "friendship" will go up. Node-oriented changes on a network like this would look like you prioritizing a new project and becoming closer with the coworkers in that new project. You did not stop having some emotional closeness to those other coworkers; you just prioritized these new relationships.

Relating this back to functional brain networks, the threshold of correlation can fluctuate based on the overall connectivity in the network, changing what it means for brain regions to be connected. Node-oriented changes in the network can be interpreted as changes to activity which aligns or misaligns a node with another node in the context of the overall correlations. In structural brain networks, the threshold for connectivity is still 20% even if the white matter tracts have significantly atrophied. In that situation, the remaining connections would be the ones that have atrophied the least. This is different than the notion that a dissolved connection means that two brain regions are no longer connected at all, but instead suggests that the brain regions have less connectivity compared to the overall connectivity.

This may seem like a subtle difference, but it has an impact on the interpretation of the effects of these models on the networks. The comparative significance of the connectivity between brain regions suggests that there is a difference between barely not meeting the threshold and being significantly below the threshold. It follows that connections that are dissolved are more likely to be created in a future time step. This is not a direct part of the models, because changes in SAOMs are memoryless and binary, but it informs the view of changes as less random and less permanent than the model alone suggests. The maintenance hypothesis acknowledges this interpretation by suggesting that the networks strive to maintain connectivity between essential regions broadly. A future study may incorporate this higher probability into these models.

There is significant evidence that the maintenance hypothesis is the strongest interpretation of the models found in this project and is grounded in the nature of the models, the networks, and the results. The maintenance hypothesis is further tested by the remaining results from this project including demographic differences. If maintenance is the nature of these models, one would not expect different groups to have extremely different models of network change, even in such a pervasive disorder as dementia and cognitive impairment; instead, marginal differences in the weights of particular factors suggest the models are pushing the network toward a different stable state. This is seen in the demographic comparison results. These models may be best interpreted as the priorities that maintain the known network structure and the differences and

disruptions to those priorities in different groups.

8.2 The Functional Compensation Hypothesis

To explore the understanding of these models further, we will refer to our second interpretive hypothesis as "the functional compensation hypothesis", which suggests that the functional network is able to compensate for the decline of the structural network. Compensate here refers to the continued ability of the functional network to perform cognitively during aging despite possible atrophy in the structural networks and this kind of compensation has been found in previous research [Ferreira 2013, Stern 2012, Nyberg 2012]. This hypothesis interacts with the maintenance hypothesis and is evidenced by a couple of important results. Overall, the functional network models suggest greater resilience to random changes by demonstrating more rapid changes, fewer physical constraints, and less impact from disorder compared to the structural network models.

First, across the board, the rate of change (ρ) on the functional networks is higher than the rate of change on the structural networks. In the model, this means that each node will have a greater number of opportunities to change between time point 1 and time point 2. Inside of the maintenance hypothesis, this suggest that the connections that are dissolved, but remain close to the threshold, will have more opportunities to reestablish. More rapid changes in the functional network compared to the structural networks align with the known behavior of these networks during short timescales [Honey 2007, Deco 2011]. Thus, it is reasonable to postulate that the functional networks, fluctuating rapidly around some stable structure, have more opportunity to correct random deviations from that stable structure compared to the structural networks.

Second, the structural network models suggest greater physical constraints on the changes that the structural network can make compared to the functional network models. This is evidenced by the higher values for the Factors Degree (D), Physical Distance (PD), and Physical Neighbor Distance (ND). This suggests that building connections is more expensive in the structural networks, especially if those connections are physically far away. At a basic level, this finding is very in line with the architecture of structural networks, which are significantly negatively correlated with distance [Alexander-Bloch 2013]. Thus, in the maintenance hypothesis, the maintenance of the short-range connectivity structure is shown in these results. However, a further look into this result, in combination with the slower rate, suggests that connections, especially long-range connections, are unlikely to be rebuilt once lost, regardless of the closeness to the threshold. This is very in line with findings of high wiring costs and physical constraints on structural networks [Sporns 2005, Bassett 2006, Nyberg 2012]. future research may be able to study this directly using

networks with fluctuating rather than static densities.

Third, differences between the impairment and control groups are more prominent and significant in the structural compared to the functional, affecting a greater number of factors. If, as we postulate, these results demonstrate the diminished resilience of the structural networks compared to the functional networks, it follows that the disruptions on the structural network from cognitive impairment will be more significant and more permanent. The differences between the impairment and control groups in the structural models demonstrate a diminishing of impacted factors while the differences in the functional models demonstrate increases and decreases in the significance of impacted factors. This indicates that the structural networks in impairment trend towards randomness more consistently compared to the functional networks. The more significant impact of impairment in the structural models suggests that the structural networks are adapting less to the disruptions of cognitive impairment. This interpretation is in line with much of the research in this area, which shows structural networks to be more rigid and prone to decline first and faster [Morcom 2015, Betzel 2015, Tang 2025, Deschwanden 2025, Madden 2020, Damoiseaux 2017].

The functional compensation hypothesis suggests that the structural results do not necessarily represent a pure maintenance of the structural networks. There is some evidence that structural networks decline much earlier than functional networks [Madden 2020, Damoiseaux 2017]. Thus, it is not unreasonable to suggest that the structural models represent some kind of trend toward decline. Future research using this approach could include younger adults to determine if the structural models of older adults demonstrate a significant difference from the structural models of younger adults. The functional compensation hypothesis, suggesting that the functional networks are adapting to random changes while the structural networks are more restricted adds to the interpretation of these models beyond the maintenance hypothesis.

8.3 The Subnetwork Compensation Hypothesis

When compensation is discussed in the literature, it is often about certain areas of the brain compensating for decline in other areas of the brain. This is found primarily in the functional networks and often during tasks [Cabeza 2002, Reuter-Lorenz 2008, Davis 2008, Bokde 2010]. However, there is some evidence of regional compensation in the resting-state as well [Tomasi 2012, Tang 2025]. The third interpretive hypothesis for the results of this study we will refer to as "the subnetwork compensation hypothesis", which suggests that certain subnetworks experience less disruption, with age or diagnosis, compared to others, and even increase activity and connectivity. This hypothesis interacts with the functional compensation hypothesis by suggesting the way in which the functional network is adapting to structural decline.

The results from this study provide some evidence of the subnetwork compensation hypothesis through

heterogeneity of results across the subnetworks in the functional models. There are differences in the rate (ρ) between the control and impairment groups in the subnetworks which do not always match the overall trend of impairment difference or the other subnetworks. Significant heterogeneity could be evidence of changes to the functional subnetwork architecture in aging. For rate, the SN and DMN follow the overall trend—a faster rate in the impairment group, while the VN and FPN show the opposite trend—a slower rate in the impairment group.

For subnetwork Factor Degree (D), a measure of intra-subnetwork connectivity, the FPN was the only subnetwork that showed a significant difference between the control and the impairment groups, with the impairment group showing a higher prioritization of intra-subnetwork connectivity. Among females, the opposite trend as the full network model is shown—females with impairment showed a decrease in intra-subnetwork connectivity, but females with impairment in the FPN showed an increase. This suggests that the FPN, specifically among females, is changing more slowly and increasing its internal connectivity with impairment.

For subnetwork Factor Betweenness (B), a measure of the hub structure inside of the subnetwork, the DMN is the only subnetwork that shows a decline in this factor in the mild impairment group. This is particularly interesting because of the significant research showing a disruption in the default mode network [Greicius 2004, Jones 2011, Tomasi 2012] with cognitive impairment. The evidence from our study is somewhat weaker, but it suggests that the DMN is increasing its rate, decreasing its internal connectivity, and perhaps losing its hub structure during cognitive impairment.

This kind of result is often interpreted as evidence of compensation; however, it is clear that this study is not measuring compensation directly. The results here are in some ways aligned with previous research on compensation in functional networks. Previous research has found disruptions in the DMN and increased activity and connectivity in the FPN [Stern 2009, Tomasi 2012, Yang 2023, Onofrj 2026, Wu 2024]. More research is needed to unravel the picture of subnetwork compensation in cognitive impairment and age. Future research would do well to increase the sample size to better examine the subnetwork differences, which appear to be more subtle than the full network results. Future research could also choose the Schaefer atlas with more overall regions (nodes) so that each subnetwork has more nodes. The structural subnetworks do not show the same heterogeneity as the functional, with the subnetwork results mostly aligning between the subnetwork and with the full network results. The subnetwork compensation hypothesis seems to exclusively explain results on the functional networks, which lends further credence to the functional compensation hypothesis by providing the beginnings of a mechanism of how the functional networks compensate.

8.4 Impairment Differences

Using our three interpretive hypotheses, we can provide greater context to the impairment differences found in this work. Overall, cognitive impairment is connected with increased rates of change in both the functional and structural networks. Functional networks show less differences between the control and impairment groups with only a few factors showing minor differences. On the other hand, the structural networks show significant differences in Factors Degree (D), Transitive Triads (T), 4-Cycles ($C4$), and Assortativity (A) all trending towards greater randomness, or less impact of the factors. The structural differences are mirrored in most of the subnetworks again trending towards greater randomness; whereas, the functional differences are more heterogenious in the subnetworks, behaving differently in different functional systems of the brain.

As we have discussed, the differences line up with the maintenance hypothesis, the functional compensation hypothesis, and the subnetwork compensation hypothesis. There are two further topics when it comes to cognitive impairment that are worth exploring further. Specifically, the differences between the mild impairment and significant impairment groups, as well as the age related differences that are seen throughout the results. This discussion contains an important asterisk in that there are very few significant impairment participants in this dataset. Future research would do well to have a more even distribution of mild and significant impairment individuals.

There is significant evidence that mild impairment behaves differently in these models compared to significant impairment. The faster rate is one of the most prominent and significant results in these models. However, this result only appears for the mild impairment group and is absent or even reversed in the significant impairment group. Even in the functional subnetworks, the results for the significant impairment group tend to be reverse of the mild impairment group—in the VN, the mild impairment rate is lower than control and the significant impairment rate is higher than control, and in the DMN, the mild impairment rate is higher than control and the significant impairment rate is lower than control. These differences in the rate between the mild and significant impairment groups indicate that there are differences in how these diseases are progressing. These results are not entirely repeated in the structural where the trend for the significant impairment group is largely the same as in the mild impairment group.

Some research has explored the possibility that MCI may not always be a precursor to AD [Petersen 2009, Mitchell 2009a, Mauri 2012, Roberts 2013]. While these results do not necessarily suggest that the mild impairment group will not progress towards significant impairment, they state that the functional networks of the mild impairment group are behaving differently than controls, but not in the same way as the significant impairment group. In the context of the functional compensation hypothesis and the subnetwork compensation hypothesis, these results would indicate that the compensation that is able to be performed by the

mild impairment group is somewhat protective, in a way, that is not present in the significant impairment group. There is some previous research in this area that indicates this compensation difference as well as lending greater credence to this interpretation [Stern 2009, Zhou 2010, Jones 2011, Grady 2012].

There are also some age-related results concerning impairment. In the structural networks especially, the mild impairment group often shows large deviations from the control group in the earliest stages of aging and almost no deviations in the latest stages of aging. In other words, the mild impairment group often trends toward the control on various factor weights with age. There are two reasonable interpretations of these results. The first is more in line with the maintenance hypothesis and suggests that some older individuals with mild impairment are demonstrating stable MCI that will not progress towards AD, explaining the greater difference in early aging. This is especially explanatory in the largely cross-sectional statistical analysis performed here. Due to the low number of time points per participant, we do not specifically analyze individuals that progress from mild impairment to significant impairment. The second interpretation of the age related result concerning mild impairment on the structural networks, less in line with the maintenance hypothesis, uses the change over time nature of the models to suggest that the differences that occur in mild impairment occur early in the disease progression. Thus, the networks are already changed, and the push towards that change is not required later in the progression. This does not particularly align with the behavior demonstrated by the models in other contexts. however, With the difference in the maintenance hypothesis in the structural models, this interpretation is not entirely oppositional to the current interpretations, as structural networks do demonstrate greater rigidity in their maintenance. A dataset with a greater number of time points per person and more individuals who progress from MCI to AD could provide a more definitive answer to this question. However, both of these interpretations, along with the overall greater impact of impairment on the structural networks, suggest that the structural networks are less adaptive compared to the functional. These add evidence to the functional compensation hypothesis and suggest that the structural networks are impacted earlier and more significantly than the functional networks.

8.5 Sex Differences

Most of the subnetwork differences in the functional networks were found primarily among females. Female participants showed greater differences between the control and impairment groups for Factor Same Subnetwork (S), as well as on the subnetwork Factors Degree (D), Betweenness (B), and Physical Distance (PD). Specifically in the DMN, females show a lower rate compared to males generally, and show more prominent differences between the control and impairment groups. In previous research, females have been shown to have higher modularity than males while males display greater hierarchical structure and inter-subnetwork

connectivity [Chen 2024, Zhang 2025] as a baseline for comparisons in decline. This is interesting in light of the functional Factor Distance 2 ($D2$) results, where female controls showed a lower negative weight for Factor $D2$. This means that females showed a lower baseline priority of segmentation. In accordance with the maintenance hypothesis, the opposite trend would perhaps be more expected.

The previous research trends are reflected in other results. The sharp decline in the positive weight of Factor S suggests a failure in modularity maintenance might be occurring among females with impairment and this appears to be driving the lower value among females generally. In accordance with the maintenance hypothesis, failure to maintain the modular structure expected in control female functional networks is a reasonable interpretation of these results. Additionally, the increase in intra-subnetwork connectivity seen in the FPN that we interpreted as a compensatory mechanism is most prominent in females who may rely more on intra-modular structure in compensation.

Highlighting the DMN specifically is important to contextualize these results in the significant amount of research surrounding the DMN's role in cognitive impairment. Prior work shows women often start with stronger DMN connectivity, but show steeper decline, especially in the hubs, in the progression of dementia [Ficek-Tani 2023, Boccalini 2025, Ju 2023]. Our results for the DMN show a faster rate for females with impairment, but a decrease in the rate in the significant impairment group. We also show a general decline in inter-subnetwork connectivity in females with impairment and a greater negative priority on DMN Factor Betweeness (B) in females with impairment. These indicate a decrease in hub connectivity over time inside the DMN. These results fall in line with the steep decline and the hub connectivity disruptions in the DMN that has been seen in females with impairment.

Overall, female participants with impairment show a stronger deterioration of the subnetwork structure especially in the DMN, compared to males, while males show a somewhat stronger trend towards randomness in the structural network. Some evidence suggests that males often show more measurable structural changes in dementia [Sangha 2021, Oltra 2024], but more evidence is needed to form a strong conclusion about structural decline. Clinically, females with MCI decline faster cognitively [Lin 2015, Koran 2017, Levine 2021]. This literature lends some support to the interpretation of stronger functional collapse in females and a stronger structural collapse in males. More research is needed to fully integrate sex differences into the maintenance hypothesis, the functional compensation hypothesis, and the subnetwork compensation hypothesis; however, there is evidence of sex differences impacting the underlying architecture of the networks and the requirements of maintaining that architecture.

8.6 Limitations and Future Directions

This study has a few limitations that are important to note. There were dataset limitations, including the limited availability of participants with Alzheimer's Disease and the relatively few time points per participant in this dataset. There are some implementation limitations. The preprocessing mistake and the inclusion of both basic and multiband scans could bias the data and results. The requirement of binarized networks for the implementation of the SAOM means that some information about the brain connectivity is lost. The factor list that was utilized here was limited to those available and usable from Rsiena. All the analyses were run on all the time windows with no particular consideration of the repeated measures. Finally, there were some execution limitations. For example, the hypothesis-building procedure is time consuming and computationally expensive, limiting the number of participants that could be included in the Hypothesis Group. These limitations were discussed throughout this thesis and there are a number of future research directions regarding these limitations that may be implemented in the future.

There are some exciting directions for future research in this area, and some of the limitations might be addressed in that future research. This work is strong evidence that data-driven testing of factor inclusion is possible and useful in selecting a hypothesis. This work is somewhat limited by the performance of that procedure, and future work could improve the efficiency and accuracy of that procedure. Additionally, future research could just utilize the principles from the procedure to systematically test additional factors before adding them to the hypothesis.

Being a preliminary application of the SAOM on brain networks, many choices were made for the sake of model simplicity. It would be interesting, for example, to expand the set of factors that are being selected from including statistical considerations of thresholding, factors integrating specific subnetworks directly into the overall model, or even factors that include sex, age, or level of impairment. One could also include rate factors. Rate factors could incorporate the subnetwork rate differences into the full network model. Statisitcal tests concerning repeated measures could be conducted. Additionally, future expansions of this framework could include a multi-network analysis to incorporate the functional-structural interactions as factors in the model. An independent implementation of the model could better reflect the specific application and allow for increased flexibility of implementation choices.

As more data becomes available, these analyses can be expanded to larger datasets to increase statistical power and gain greater insight into Alzheimer's Disease and disease progression. Moreover, this approach can be applied to other age groups across the lifetime including early childhood and adolescence. It could also be applied to other brain conditions with questions about progression like Parkinson's Disease or Autism Spectrum Disorder. This initial implementation serves as a proof of concept for a robust and data-driven

implementation of the SAOM on brain networks and expands on and alters procedures significantly from the only other use of the SAOM on brain networks ([Shappell 2019]).

8.7 Conclusion

This thesis was able to achieve all of its objectives in developing a set of models of network change in the aging brain.

1. Developed a data-driven procedure for deriving factors in SAOM and evaluated the procedure on a simulated dataset.

2. Applied the procedure to functional and structural aging brain data to derive models of network change over time.

3. Analyzed and compared the resultant longitudinal models to demographic measures of impairment, sex, and age to understand the models in the context of aging and neurodegenerative illness.

A data-driven method for deriving a hypothesis of factors for the models was developed and tested, demonstrating success in deriving underlying SAOM hypotheses.

This method was then applied to the functional and structural brain networks from the dataset. The results were a dynamical description of how networks change over time and showed networks prioritizing clustering, segmentation, and short-range connectivity, likely maintaining key network structures.

Analyses of differences across demographic measures of impairment, sex, and age were conducted to understand the differing long-term dynamics in these groups. The results revealed disruptions to the maintenance of the networks in cognitive impairment, evidence of functional compensation for structural decline, differences between mild impairment and significant impairment, especially in subnetwork compensation and rate of change, and differences in modularity maintenance between sexes. These results represent a new understanding of the ways in which we age, consistent with and expanding upon the current picture.

Bibliography

[Alexander-Bloch 2013] Alexander-Bloch, A. F., Vértes, P. E., Stidd, R., et al. "The Anatomical Distance of Functional Connections Predicts Brain Network Topology in Health and Schizophrenia". *Cerebral Cortex*, **23**, 127–138 (2013).

[Allen 2014] Allen, E. A., Damaraju, E., Plis, S. M., et al. "Tracking Whole-Brain Connectivity Dynamics in the Resting State". *Cerebral Cortex*, **24**, 663–676 (2014).

[Ashburner 2021] Ashburner, J., Barnes, G., Chen, C.-C., et al. "SPM Manual" (2021).

[Aung 2013] Aung, W. Y., Mar, S., & Benzinger, T. L. "Diffusion tensor MRI as a biomarker in axonal and myelin damage". *Imaging in Medicine*, **5**, 427–440 (2013).

[Avants 2011] Avants, B. B., Tustison, N. J., Song, G., et al. "A reproducible evaluation of ANTs similarity metric performance in brain image registration". *NeuroImage*, **54**, 2033–2044 (2011).

[Baldassarre 2012] Baldassarre, A., Lewis, C. M., Committeri, G., et al. "Individual variability in functional connectivity predicts performance of a perceptual task". *Proceedings of the National Academy of Sciences*, **109**, 3516–3521 (2012).

[Bar-Yam 2019] Bar-Yam, Y. "Dynamics Of Complex Systems". CRC Press, Boca Raton (2019).

[Bassett 2006] Bassett, D. S. & Bullmore, E. "Small-World Brain Networks". *The Neuroscientist*, **12**, 512–523 (2006).

[Bassett 2011] Bassett, D. S., Wymbs, N. F., Porter, M. A., et al. "Dynamic reconfiguration of human brain networks during learning". *Proceedings of the National Academy of Sciences of the United States of America*, **108**, 7641–7646 (2011).

[Bernstein 2004] Bernstein, M. A., King, K. F., & Zhou, X. J. "Introduction to Radiofrequency Pulses". In Handbook of MRI Pulse Sequences, 29–34. Academic Press, Burlington (2004).

[Betzel 2013] Betzel, R. F., Griffa, A., Avena-Koenigsberger, A., et al. "Multi-scale community organization of the human structural connectome and its relationship with resting-state functional connectivity". *Network Science*, **1**, 353–373 (2013).

[Betzel 2014] Betzel, R. F., Byrge, L., He, Y., et al. "Changes in structural and functional connectivity among resting-state networks across the human lifespan". *NeuroImage*, **102 Pt 2**, 345–357 (2014).

[Betzel 2015] Betzel, R. F., Mišić, B., He, Y., et al. "Functional brain modules reconfigure at multiple scales across the human lifespan" (2015).

[Betzel 2019] Betzel, R. F., Wood, K. C., Angeloni, C., Neimark Geffen, M., & Bassett, D. S. "Stability of spontaneous, correlated activity in mouse auditory cortex". *PLoS Computational Biology*, **15**, e1007360 (2019).

[Biggs 1986] Biggs, N., Lloyd, E. K., & Wilson, R. J. "Graph Theory, 1736-1936". Clarendon Press (1986).

[Blum 1954] Blum, J. R. "Multidimensional Stochastic Approximation Methods". *The Annals of Mathematical Statistics*, **25**, 737–744 (1954).

[Boccalini 2025] Boccalini, C., Peretti, D. E., Scheffler, M., et al. "Sex differences in the association of Alzheimer's disease biomarkers and cognition in a multicenter memory clinic study". *Alzheimer's Research & Therapy*, **17**, 46 (2025).

[Bokde 2010] Bokde, A. L. W., Karmann, M., Born, C., et al. "Altered brain activation during a verbal working memory task in subjects with amnestic mild cognitive impairment". *Journal of Alzheimer's Disease: JAD*, **21**, 103–118 (2010).

[Borchardt 2016] Borchardt, V., Lord, A. R., Li, M., et al. "Preprocessing strategy influences graph-based exploration of altered functional networks in major depression". *Human Brain Mapping*, **37**, 1422–1442 (2016).

[Borkar 2006] Borkar, V. "Stochastic approximation with controlled Markov noise". *Systems & Control Letters*, **55**, 139–145 (2006).

[Boyd 2013] Boyd, K., Eng, K. H., & Page, C. D. "Area under the Precision-Recall Curve: Point Estimates and Confidence Intervals". In Machine Learning and Knowledge Discovery in Databases, 451–466, Berlin, Heidelberg (2013).

[Brier 2014] Brier, M. R., Thomas, J. B., Fagan, A. M., et al. "Functional connectivity and graph theory in preclinical Alzheimer's disease". *Neurobiology of Aging*, **35**, 757–768 (2014).

[Brinkman 2022] Brinkman, B. A. W., Yan, H., Maffei, A., et al. "Metastable dynamics of neural circuits and networks". *Applied Physics Reviews*, **9**, 011313 (2022).

[Buckland 1994] Buckland, M. & Gey, F. "The relationship between Recall and Precision". *Journal of the American Society for Information Science*, **45**, 12–19 (1994).

[Buckner 2008] Buckner, R. L., Andrews-Hanna, J. R., & Schacter, D. L. "The Brain's Default Network". *Annals of the New York Academy of Sciences*, **1124**, 1–38 (2008).

[Bullmore 2009] Bullmore, E. & Sporns, O. "Complex brain networks: graph theoretical analysis of structural and functional systems". *Nature Reviews Neuroscience*, **10**, 186–198 (2009).

[Bullmore 2012] Bullmore, E. & Sporns, O. "The economy of brain network organization". *Nature Reviews Neuroscience*, **13**, 336–349 (2012).

[Cabeza 2002] Cabeza, R., Anderson, N. D., Locantore, J. K., & McIntosh, A. R. "Aging Gracefully: Compensatory Brain Activity in High-Performing Older Adults". *NeuroImage*, **17**, 1394–1402 (2002).

[Caeyenberghs 2017] Caeyenberghs, K., Verhelst, H., Clemente, A., & Wilson, P. H. "Mapping the functional connectome in traumatic brain injury: What can graph metrics tell us?". *NeuroImage*, **160**, 113–123 (2017).

[Canadian Insitute for Health Information 2018] Canadian Insitute for Health Information. "Dementia in Canada" (2018).

[Carbonell 2011] Carbonell, F., Bellec, P., & Shmuel, A. "Global and system-specific resting-state fMRI fluctuations are uncorrelated: principal component analysis reveals anti-correlated networks". *Brain Connectivity*, **1**, 496–510 (2011).

[Chan 2014] Chan, M. Y., Park, D. C., Savalia, N. K., Petersen, S. E., & Wig, G. S. "Decreased segregation of brain systems across the healthy adult lifespan". *Proceedings of the National Academy of Sciences*, **111**, E4997–E5006 (2014).

[Chen 2024] Chen, W., Zhan, L., & Jia, T. "Sex Differences in Hierarchical and Modular Organization of Functional Brain Networks: Insights from Hierarchical Entropy and Modularity Analysis". *Entropy*, **26**, 864 (2024).

[Chklovskii 2004] Chklovskii, D. B., Mel, B. W., & Svoboda, K. "Cortical rewiring and information storage". *Nature*, **431**, 782–788 (2004).

[Conturo 1999] Conturo, T. E., Lori, N. F., Cull, T. S., et al. "Tracking neuronal fiber pathways in the living human brain". *Proceedings of the National Academy of Sciences of the United States of America*, **96**, 10422–10427 (1999).

[Costa 2007] Costa, L. d. F., Rodrigues, F. A., Travieso, G., & Villas Boas, P. R. "Characterization of complex networks: A survey of measurements". *Advances in Physics*, **56**, 167–242 (2007).

[Dai 2014] Dai, Z. & He, Y. "Disrupted structural and functional brain connectomes in mild cognitive impairment and Alzheimer's disease". *Neuroscience Bulletin*, **30**, 217–232 (2014).

[Damoiseaux 2017] Damoiseaux, J. S. "Effects of aging on functional and structural brain connectivity". *NeuroImage*, **160**, 32–40 (2017).

[Davis 1998] Davis, T. L., Kwong, K. K., Weisskoff, R. M., & Rosen, B. R. "Calibrated functional MRI: Mapping the dynamics of oxidative metabolism". *Proceedings of the National Academy of Sciences*, **95**, 1834–1839 (1998).

[Davis 2008] Davis, S. W., Dennis, N. A., Daselaar, S. M., Fleck, M. S., & Cabeza, R. "Que PASA? The posterior-anterior shift in aging". *Cerebral Cortex*, **18**, 1201–1209 (2008).

[Deco 2009] Deco, G., Rolls, E. T., & Romo, R. "Stochastic dynamics as a principle of brain function". *Progress in Neurobiology*, **88**, 1–16 (2009).

[Deco 2011] Deco, G., Jirsa, V. K., & McIntosh, A. R. "Emerging concepts for the dynamical organization of resting-state activity in the brain". *Nature Reviews Neuroscience*, **12**, 43–56 (2011).

[Deco 2012] Deco, G. & Jirsa, V. K. "Ongoing Cortical Activity at Rest: Criticality, Multistability, and Ghost Attractors". *Journal of Neuroscience*, **32**, 3366–3375 (2012).

[Deery 2023] Deery, H. A., Di Paolo, R., Moran, C., Egan, G. F., & Jamadar, S. D. "The older adult brain is less modular, more integrated, and less efficient at rest: A systematic review of large-scale resting-state functional brain networks in aging". *Psychophysiology*, **60**, e14159 (2023).

[Denck 2022] Denck, J. "Machine Learning-based Workflow Enhancements in Magnetic Resonance Imaging". Friedrich-Alexander-Universitaet Erlangen-Nuernberg (PhD Dissertation) (2022).

[Deschwanden 2025] Deschwanden, P. F., Hotz, I., Mérillat, S., & Jäncke, L. "Functional connectivity-based compensation in the brains of non-demented older adults and the influence of lifestyle: A longitudinal 7-year study". *NeuroImage*, **308**, 121075 (2025).

[Dhollander 2016] Dhollander, T., Raffelt, D., & Connelly, A. "Unsupervised 3-tissue response function estimation from single-shell or multi-shell diffusion MR data without a co-registered T1 image" (2016).

[Duxbury 2023] Duxbury, S. "Longitudinal Network Models". SAGE Publications, Inc (2023).

[Eguíluz 2005] Eguíluz, V. M., Chialvo, D. R., Cecchi, G. A., Baliki, M., & Apkarian, A. V. "Scale-free brain functional networks". *Physical Review Letters*, **94**, 018102 (2005).

[Ercsey-Ravasz 2013] Ercsey-Ravasz, M., Markov, N. T., Lamy, C., et al. "A predictive network model of cerebral cortical connectivity based on a distance rule". *Neuron*, **80**, 184–197 (2013).

[Euler 1741] Euler, L. "Solutio problematis ad geometriam situs pertinentis". *Commentarii academiae scientiarum Petropolitanae*, 128–140 (1741).

[Fair 2008] Fair, D. A., Cohen, A. L., Dosenbach, N. U. F., et al. "The maturing architecture of the brain's default network". *Proceedings of the National Academy of Sciences*, **105**, 4028–4032 (2008).

[Faisal 2008] Faisal, A. A., Selen, L. P. J., & Wolpert, D. M. "Noise in the nervous system". *Nature Reviews Neuroscience*, **9**, 292–303 (2008).

[Feldt 2011] Feldt, S., Bonifazi, P., & Cossart, R. "Dissecting functional connectivity of neuronal microcircuits: experimental and theoretical insights". *Trends in Neurosciences*, **34**, 225–236 (2011).

[Ferreira 2013] Ferreira, L. K. & Busatto, G. F. "Resting-state functional connectivity in normal brain aging". *Neuroscience and Biobehavioral Reviews*, **37**, 384–400 (2013).

[Ficek-Tani 2023] Ficek-Tani, B., Horien, C., Ju, S., et al. "Sex differences in default mode network connectivity in healthy aging adults". *Cerebral Cortex*, **33**, 6139–6151 (2023).

[Fisher 2017] Fisher, D. N., Ilany, A., Silk, M. J., & Tregenza, T. "Analysing animal social network dynamics: the potential of stochastic actor-oriented models". *Journal of Animal Ecology*, **86**, 202–212 (2017).

[Forrester 2020] Forrester, M., Crofts, J. J., Sotiropoulos, S. N., Coombes, S., & O'Dea, R. D. "The role of node dynamics in shaping emergent functional connectivity patterns in the brain". *Network Neuroscience*, **4**, 467–483 (2020).

[Franzke 2015] Franzke, C. L. E., O'Kane, T. J., Berner, J., Williams, P. D., & Lucarini, V. "Stochastic Climate Theory and Modelling". *WIREs Climate Change*, **6**, 63–78 (2015).

[Gardiner 2010] Gardiner, C. "Stochastic Methods: A Handbook for the Natural and Social Sciences". Springer Berlin Heidelberg (2010).

[Garrison 2015] Garrison, K. A., Scheinost, D., Finn, E. S., Shen, X., & Constable, R. T. "The (in)stability of functional brain network measures across thresholds". *NeuroImage*, **118**, 651–661 (2015).

[Gonzalez-Castillo 2021] Gonzalez-Castillo, J., Kam, J. W. Y., Hoy, C. W., & Bandettini, P. A. "How to Interpret Resting-State fMRI: Ask Your Participants". *Journal of Neuroscience*, **41**, 1130–1141 (2021).

[Goutte 2005] Goutte, C. & Gaussier, E. "A Probabilistic Interpretation of Precision, Recall and F-Score, with Implication for Evaluation". In Advances in Information Retrieval, 345–359, Berlin, Heidelberg (2005).

[Grady 2012] Grady, C. "The cognitive neuroscience of ageing". *Nature Reviews Neuroscience*, **13**, 491–505 (2012).

[Gratton 2018] Gratton, C., Laumann, T. O., Nielsen, A. N., et al. "Functional Brain Networks Are Dominated by Stable Group and Individual Factors, Not Cognitive or Daily Variation". *Neuron*, **98**, 439–452.e5 (2018).

[Greicius 2004] Greicius, M. D., Srivastava, G., Reiss, A. L., & Menon, V. "Default-mode network activity distinguishes Alzheimer's disease from healthy aging: evidence from functional MRI". *Proceedings of the National Academy of Sciences of the United States of America*, **101**, 4637–4642 (2004).

[Gross 2005] Gross, J. L. & Yellen, J. "Graph Theory and Its Applications, Second Edition". CRC Press (2005).

[Gu 2014] Gu, L., Kleiber, S., Schmid, L., et al. "Long-Term In Vivo Imaging of Dendritic Spines in the Hippocampus Reveals Structural Plasticity". *Journal of Neuroscience*, **34**, 13948–13953 (2014).

[Hagmann 2007] Hagmann, P., Kurant, M., Gigandet, X., et al. "Mapping Human Whole-Brain Structural Networks with Diffusion MRI". *PLoS ONE*, **2**, e597 (2007).

[Hagmann 2008] Hagmann, P., Cammoun, L., Gigandet, X., et al. "Mapping the Structural Core of Human Cerebral Cortex". *PLoS Biology*, **6**, e159 (2008).

[Hagmann 2010] Hagmann, P., Sporns, O., Madan, N., et al. "White matter maturation reshapes structural connectivity in the late developing human brain". *Proceedings of the National Academy of Sciences*, **107**, 19067–19072 (2010).

[Holovatch 2017] Holovatch, Y., Kenna, R., & Thurner, S. "Complex systems: physics beyond physics". *European Journal of Physics*, **38**, 023002 (2017).

[Honey 2007] Honey, C. J., Kötter, R., Breakspear, M., & Sporns, O. "Network structure of cerebral cortex shapes functional connectivity on multiple time scales". *Proceedings of the National Academy of Sciences*, **104**, 10240–10245 (2007).

[Honey 2009] Honey, C. J., Sporns, O., Cammoun, L., et al. "Predicting human resting-state functional connectivity from structural connectivity". *Proceedings of the National Academy of Sciences*, **106**, 2035–2040 (2009).

[Hutchison 2013] Hutchison, R. M., Womelsdorf, T., Allen, E. A., et al. "Dynamic functional connectivity: Promise, issues, and interpretations". *NeuroImage*, **80**, 360–378 (2013).

[Jafari 2019] Jafari, M. J., Khosrowabadi, R., Khodakarim, S., & Mohammadian, F. "The Effect of Noise Exposure on Cognitive Performance and Brain Activity Patterns". *Open Access Macedonian Journal of Medical Sciences*, **7**, 2924–2931 (2019).

[Jahn 2022] Jahn, A., Levitas, D., Holscher, E., et al. "Andy's Brain Book" (2022).

[Jauny 2024] Jauny, G., Mijalkov, M., Canal-Garcia, A., et al. "Linking structural and functional changes during aging using multilayer brain network analysis". *Communications Biology*, **7**, 239 (2024).

[Jeurissen 2014] Jeurissen, B., Tournier, J.-D., Dhollander, T., Connelly, A., & Sijbers, J. "Multi-tissue constrained spherical deconvolution for improved analysis of multi-shell diffusion MRI data". *NeuroImage*, **103**, 411–426 (2014).

[Jones 2011] Jones, D. T., Machulda, M. M., Vemuri, P., et al. "Age-related changes in the default mode network are more advanced in Alzheimer disease". *Neurology*, **77**, 1524–1531 (2011).

[Ju 2023] Ju, S., Horien, C., Shen, X., et al. "Connectome-based predictive modeling shows sex differences in brain-based predictors of memory performance". *Frontiers in Dementia*, **2** (2023).

[Kaiser 2011] Kaiser, M. & Varier, S. "Evolution and development of brain networks: from Caenorhabditis elegans to Homo sapiens". *Network (Bristol, England)*, **22**, 143–147 (2011).

[Kalpouzos 2025] Kalpouzos, G. & Persson, J. "Structure–function relationships in the human aging brain: An account of cross-sectional and longitudinal multimodal neuroimaging studies". *Cortex*, **183**, 274–289 (2025).

[Kampen 1992] Kampen, N. G. V. "Stochastic Processes in Physics and Chemistry". Elsevier (1992).

[Kim 2004] Kim, D.-S., Ronen, I., Olman, C., et al. "Spatial relationship between neuronal activity and BOLD functional MRI". *NeuroImage*, **21**, 876–885 (2004).

[Kim 2017] Kim, B., Lee, K., Xue, L., & Niu, X. "A Review of Dynamic Network Models with Latent Variables". *Statistics Surveys*, **12** (2017).

[Kimelberg 2004] Kimelberg, H. K. "Water homeostasis in the brain: Basic concepts". *Neuroscience*, **129**, 851–860 (2004).

[Kiviniemi 2008] Kiviniemi, V. "Endogenous brain fluctuations and diagnostic imaging". *Human Brain Mapping*, **29**, 810–817 (2008).

[Koran 2017] Koran, M. E. I., Wagener, M., Hohman, T. J., & for the Alzheimer's Neuroimaging Initiative. "Sex differences in the association between AD biomarkers and cognitive decline". *Brain Imaging and Behavior*, **11**, 205–213 (2017).

[Lanchier 2017] Lanchier, N. "Stochastic Modeling". Springer (2017).

[Lebel 2012] Lebel, C., Gee, M., Camicioli, R., et al. "Diffusion tensor imaging of white matter tract evolution over the lifespan". *NeuroImage*, **60**, 340–352 (2012).

[Leifeld 2015] Leifeld, P. & Cranmer, S. "A Theoretical and Empirical Comparison of the Temporal Exponential Random Graph Model and the Stochastic Actor-Oriented Model". *Network Science*, **7** (2015).

[Levin 2009] Levin, D. A., Peres, Y., & Wilmer, E. L. "Markov Chains and Mixing Times". American Mathematical Soc. (2009).

[Levine 2021] Levine, D. A., Gross, A. L., Briceño, E. M., et al. "Sex Differences in Cognitive Decline Among US Adults". *JAMA network open*, **4**, e210169 (2021).

[Lewis 2012] Lewis, K., Gonzalez, M., & Kaufman, J. "Social selection and peer influence in an online social network". *Proceedings of the National Academy of Sciences of the United States of America*, **109**, 68–72 (2012).

[Lillis 2008] Lillis, K. P., Eng, A., White, J. A., & Mertz, J. "Two-photon imaging of spatially extended neuronal network dynamics with high temporal resolution". *Journal of Neuroscience Methods*, **172**, 178–184 (2008).

[Lin 2015] Lin, K. A., Choudhury, K. R., Rathakrishnan, B. G., et al. "Marked gender differences in progression of mild cognitive impairment over 8 years". *Alzheimer's & Dementia (New York, N Y)*, **1**, 103–110 (2015).

[Litwin-Kumar 2012] Litwin-Kumar, A. & Doiron, B. "Slow dynamics and high variability in balanced cortical networks with clustered connections". *Nature Neuroscience*, **15**, 1498–1505 (2012).

[Litwin-Kumar 2014] Litwin-Kumar, A. & Doiron, B. "Formation and maintenance of neuronal assemblies through synaptic plasticity". *Nature Communications*, **5**, 5319 (2014).

[Liu 2017] Liu, T. T., Nalci, A., & Falahpour, M. "The Global Signal in fMRI: Nuisance or Information?". *NeuroImage*, **150**, 213–229 (2017).

[Lospinoso 2019] Lospinoso, J. & Snijders, T. A. "Goodness of fit for stochastic actor-oriented models". *Methodological Innovations*, **12**, 2059799119884282 (2019).

[Macey 2004] Macey, P. M., Macey, K. E., Kumar, R., & Harper, R. M. "A method for removal of global effects from fMRI time series". *NeuroImage*, **22**, 360–366 (2004).

[Madan 2010] Madan, D. B. "Stochastic Processes in Finance". *Annual Review of Financial Economics*, **2**, 277–314 (2010).

[Madden 2020] Madden, D. J., Jain, S., Monge, Z. A., et al. "Influence of structural and functional brain connectivity on age-related differences in fluid cognition". *Neurobiology of Aging*, **96**, 205–222 (2020).

[Marrec 2023] Marrec, L., Bank, C., & Bertrand, T. "Solving the stochastic dynamics of population growth". *Ecology and Evolution*, **13**, e10295 (2023).

[Mauri 2012] Mauri, M., Sinforiani, E., Zucchella, C., Cuzzoni, M. G., & Bono, G. "Progression to dementia in a population with amnestic mild cognitive impairment: clinical variables associated with conversion". *Functional Neurology*, **27**, 49–54 (2012).

[Mazzucato 2015] Mazzucato, L., Fontanini, A., & Camera, G. L. "Dynamics of Multistable States during Ongoing and Evoked Cortical Activity". *Journal of Neuroscience*, **35**, 8214–8231 (2015).

[Meunier 2009] Meunier, D., Lambiotte, R., Fornito, A., Ersche, K. D., & Bullmore, E. T. "Hierarchical Modularity in Human Brain Functional Networks". *Frontiers in Neuroinformatics*, **3**, 37 (2009).

[Meunier 2010] Meunier, D., Lambiotte, R., & Bullmore, E. T. "Modular and hierarchically modular organization of brain networks". *Frontiers in Neuroscience*, **4**, 200 (2010).

[Mitchell 2009a] Mitchell, A. J. & Shiri-Feshki, M. "Rate of progression of mild cognitive impairment to dementia–meta-analysis of 41 robust inception cohort studies". *Acta Psychiatrica Scandinavica*, **119**, 252–265 (2009).

[Mitchell 2009b] Mitchell, M. "Complexity : a guided tour". Oxford University Press (2009).

[Mohrenberg 2017] Mohrenberg, S. "Studying Policy Diffusion with Stochastic Actor-Oriented Models". In Networked Governance: New Research Perspectives, 163–188. Springer International Publishing, Cham (2017).

[Morcom 2015] Morcom, A. M. & Johnson, W. "Neural reorganization and compensation in aging". *Journal of Cognitive Neuroscience*, **27**, 1275–1285 (2015).

[Murphy 2017] Murphy, K. & Fox, M. D. "Towards a consensus regarding global signal regression for resting state functional connectivity MRI". *NeuroImage*, **154**, 169–173 (2017).

[Muzio 2025] Muzio, M. R., Fakoya, A. O., & Cascella, M. "Histology, Axon". In StatPearls (2025).

[Nel 2023] Nel, M. "MRI Physics" (2023).

[Nieto-Castanon 2020] Nieto-Castanon, A. "Handbook of functional connectivity magnetic resonance imaging methods in CONN". Hilbert Press (2020).

[Niu 2022] Niu, Y., Sun, J., Wang, B., et al. "Trajectories of brain entropy across lifetime estimated by resting state functional magnetic resonance imaging". *Human Brain Mapping*, **43**, 4359–4369 (2022).

[Nyberg 2012] Nyberg, L., Lövdén, M., Riklund, K., Lindenberger, U., & Bäckman, L. "Memory aging and brain maintenance". *Trends in Cognitive Sciences*, **16**, 292–305 (2012).

[O'Bryant 2008] O'Bryant, S. E., Waring, S. C., Cullum, C. M., et al. "Staging Dementia Using Clinical Dementia Rating Scale Sum of Boxes Scores". *Archives of neurology*, **65**, 1091–1095 (2008).

[Oltra 2024] Oltra, J., Habich, A., Schwarz, C. G., et al. "Sex differences in brain atrophy in dementia with Lewy bodies". *Alzheimer's & Dementia: The Journal of the Alzheimer's Association*, **20**, 1815–1826 (2024).

[Onofrj 2026] Onofrj, V., Franciotti, R., Mitterova, K., et al. "MCI-LB brain networks reorganization in relation to specific cognitive domains deficits". *Scientific Reports* (2026).

[Onuchin 2023] Onuchin, A. A., Chernizova, A. V., Lebedev, M. A., & Polovnikov, K. E. "Communities in C elegans connectome through the prism of non-backtracking walks". *Scientific Reports*, **13**, 22923 (2023).

[Parker 2019] Parker, D. B. & Razlighi, Q. R. "The Benefit of Slice Timing Correction in Common fMRI Preprocessing Pipelines". *Frontiers in Neuroscience*, **13** (2019).

[Petersen 2009] Petersen, R. C., Roberts, R. O., Knopman, D. S., et al. "Mild cognitive impairment: ten years later". *Archives of Neurology*, **66**, 1447–1455 (2009).

[Power 2011] Power, J. D., Cohen, A. L., Nelson, S. M., et al. "Functional network organization of the human brain". *Neuron*, **72**, 665–678 (2011).

[Power 2015] Power, J. D., Schlaggar, B. L., & Petersen, S. E. "Recent progress and outstanding issues in motion correction in resting state fMRI". *NeuroImage*, **105**, 536–551 (2015).

[Powers 2008] Powers, D. "Evaluation: From Precision, Recall and F-Factor to ROC, Informedness, Markedness & Correlation". *Mach Learn Technol*, **2** (2008).

[Public Health Agency of Canada 2020] Public Health Agency of Canada. "Aging and chronic diseases: A profile of Canadian seniors - Canadaca" (2020).

[Quintane 2013] Quintane, E., Pattison, P. E., Robins, G. L., & Mol, J. M. "Short- and long-term stability in organizational networks: Temporal structures of project teams". *Social Networks*, **35**, 528–540 (2013).

[Ranasinghe 2024] Ranasinghe, P. V. N. N. & Mapa, M. S. T. "Functional connectivity and cognitive decline: a review of rs-fMRI, EEG, MEG, and graph theory approaches in aging and dementia". *Exploration of Medicine*, **5**, 797–821 (2024).

[Reijneveld 2007] Reijneveld, J. C., Ponten, S. C., Berendse, H. W., & Stam, C. J. "The application of graph theoretical analysis to complex networks in the brain". *Clinical neurophysiology*, **118**, 2317–2331 (2007).

[Reuter-Lorenz 2008] Reuter-Lorenz, P. A. & Cappell, K. A. "Neurocognitive Aging and the Compensation Hypothesis". *Current Directions in Psychological Science*, **17**, 177–182 (2008).

[Richardson 2024] Richardson, E., Trevizani, R., Greenbaum, J. A., et al. "The receiver operating characteristic curve accurately assesses imbalanced datasets". *Patterns*, **5**, 100994 (2024).

[Robbins 1951] Robbins, H. & Monro, S. "A Stochastic Approximation Method". *The Annals of Mathematical Statistics*, **22**, 400–407 (1951).

[Roberts 2013] Roberts, R. & Knopman, D. S. "Classification and epidemiology of MCI". *Clinics in Geriatric Medicine*, **29**, 753–772 (2013).

[Roberts 2016] Roberts, J. A., Perry, A., Lord, A. R., et al. "The contribution of geometry to the human connectome". *NeuroImage*, **124**, 379–393 (2016).

[Rocha 2018] Rocha, R. P., Koçillari, L., Suweis, S., Corbetta, M., & Maritan, A. "Homeostatic plasticity and emergence of functional networks in a whole-brain model at criticality". *Scientific Reports*, **8**, 15682 (2018).

[Saito 2015] Saito, T. & Rehmsmeier, M. "The Precision-Recall Plot Is More Informative than the ROC Plot When Evaluating Binary Classifiers on Imbalanced Datasets". *PLoS ONE*, **10**, e0118432 (2015).

[Sala-Llonch 2015] Sala-Llonch, R., Bartrés-Faz, D., & Junqué, C. "Reorganization of brain networks in aging: a review of functional connectivity studies". *Frontiers in Psychology*, **6** (2015).

[Sangha 2021] Sangha, O., Ma, D., Popuri, K., et al. "Structural volume and cortical thickness differences between males and females in cognitively normal, cognitively impaired and Alzheimer's dementia population". *Neurobiology of Aging*, **106**, 1–11 (2021).

[Saxena 2020] Saxena, A. "A Survey of Evolving Models for Weighted Complex Networks based on their Dynamics and Evolution" (2020).

[Schaefer 2018] Schaefer, A., Kong, R., Gordon, E. M., et al. "Local-Global Parcellation of the Human Cerebral Cortex from Intrinsic Functional Connectivity MRI". *Cerebral Cortex (New York, NY: 1991)*, **28**, 3095–3114 (2018).

[Scheinost 2019] Scheinost, D., Noble, S., Horien, C., et al. "Ten simple rules for predictive modeling of individual differences in neuroimaging". *NeuroImage*, **193**, 35–45 (2019).

[Scholtens 2022] Scholtens, L. H., Pijnenburg, R., de Lange, S. C., et al. "Common Microscale and Macroscale Principles of Connectivity in the Human Brain". *The Journal of Neuroscience: The Official Journal of the Society for Neuroscience*, **42**, 4147–4163 (2022).

[Schulz 2024] Schulz, M., Petersen, M., Cheng, B., & Thomalla, G. "Association of structural connectivity with functional brain network segregation in a middle-aged to elderly population". *Frontiers in Aging Neuroscience*, **16** (2024).

[Seghier 2018] Seghier, M. L. & Price, C. J. "Interpreting and Utilising Intersubject Variability in Brain Function". *Trends in Cognitive Sciences*, **22**, 517–530 (2018).

[Sexton 2014] Sexton, C. E., Walhovd, K. B., Storsve, A. B., et al. "Accelerated Changes in White Matter Microstructure during Aging: A Longitudinal Diffusion Tensor Imaging Study". *Journal of Neuroscience*, **34**, 15425–15436 (2014).

[Shappell 2019] Shappell, H., Tripodis, Y., Killiany, R. J., & Kolaczyk, E. D. "A paradigm for longitudinal complex network analysis over patient cohorts in neuroscience". *Network Science*, **7**, 196–214 (2019).

[Shine 2016] Shine, J. M., Bissett, P. G., Bell, P. T., et al. "The Dynamics of Functional Brain Networks: Integrated Network States during Cognitive Task Performance". *Neuron*, **92**, 544–554 (2016).

[Shirani 2022] Shirani, S. & Mohebbi, M. "Brain functional connectivity analysis in patients with relapsing-remitting multiple sclerosis: A graph theory approach of EEG resting state". *Frontiers in Neuroscience*, **16** (2022).

[Siegenfeld 2020] Siegenfeld, A. F. & Bar-Yam, Y. "An Introduction to Complex Systems Science and Its Applications". *Complexity*, **2020** (2020).

[Sladky 2011] Sladky, R., Friston, K. J., Tröstl, J., et al. "Slice-timing effects and their correction in functional MRI". *NeuroImage*, **58**, 588–594 (2011).

[Smith 2004] Smith, S. M., Jenkinson, M., Woolrich, M. W., et al. "Advances in functional and structural MR image analysis and implementation as FSL". *NeuroImage*, **23 Suppl 1**, S208–219 (2004).

[Smith 2012] Smith, R. E., Tournier, J.-D., Calamante, F., & Connelly, A. "Anatomically-constrained tractography: improved diffusion MRI streamlines tractography through effective use of anatomical information". *NeuroImage*, **62**, 1924–1938 (2012).

[Smith 2013] Smith, S. M., Vidaurre, D., Beckmann, C. F., et al. "Functional connectomics from resting-state fMRI". *Trends in Cognitive Sciences*, **17**, 666–682 (2013).

[Snijders 1996] Snijders, T. A. "Stochastic actor-oriented models for network change". *The Journal of Mathematical Sociology*, **21**, 149–172 (1996).

[Snijders 2010] Snijders, T. A. B., van de Bunt, G. G., & Steglich, C. E. G. "Introduction to stochastic actor-based models for network dynamics". *Social Networks*, **32**, 44–60 (2010).

[Snijders 2024] Snijders, T. A., Ripley, R., Bóda, Z., Vörös, A., & Preciado, P. "Manual for RSiena". University of Groningen (2024,).

[Snijders 2025] Snijders, T. A. B. "RSiena algorithms" (2025).

[Soman 2020] Soman, S. M., Raghavan, S., Rajesh, P. G., et al. "Does resting state functional connectivity differ between mild cognitive impairment and early Alzheimer's dementia?". *Journal of the Neurological Sciences*, **418**, 117093 (2020).

[Sporns 2005] Sporns, O., Tononi, G., & Kötter, R. "The Human Connectome: A Structural Description of the Human Brain". *PLoS Computational Biology*, **1**, e42 (2005).

[Sporns 2016] Sporns, O. & Betzel, R. F. "Modular Brain Networks". *Annual Review of Psychology*, **67**, 613–640 (2016).

[Stadtfeld 2015] Stadtfeld, C. & Pentland, A. S. "Partnership Ties Shape Friendship Networks: A Dynamic Social Network Study". *Social Forces*, **94**, 453–477 (2015).

[Stam 2009] Stam, C. J., de Haan, W., Daffertshofer, A., et al. "Graph theoretical analysis of magnetoencephalographic functional connectivity in Alzheimer's disease". *Brain: A Journal of Neurology*, **132**, 213–224 (2009).

[Stern 2009] Stern, Y. "Cognitive reserve". *Neuropsychologia*, **47**, 2015–2028 (2009).

[Stern 2012] Stern, Y. "Cognitive reserve in ageing and Alzheimer's disease". *The Lancet Neurology*, **11**, 1006–1012 (2012).

[Supekar 2008] Supekar, K., Menon, V., Rubin, D., Musen, M., & Greicius, M. D. "Network Analysis of Intrinsic Functional Brain Connectivity in Alzheimer's Disease". *PLoS Computational Biology*, **4**, e1000100 (2008).

[Tang 2025] Tang, H., Zhao, H., Liu, H., et al. "Structural damage-driven brain compensation among near-centenarians and centenarians without dementia". *NeuroImage*, **308**, 121065 (2025).

[Taylor 2014] Taylor, H. M. & Karlin, S. "An Introduction to Stochastic Modeling". Academic Press (2014).

[The MathWorks, Inc. 2023] The MathWorks, Inc. "Signal Processing Toolbox" (2023).

[Thompson 2018] Thompson, G. J. "Neural and metabolic basis of dynamic resting state fMRI". *NeuroImage*, **180**, 448–462 (2018).

[Tomasi 2012] Tomasi, D. & Volkow, N. D. "Aging and functional brain networks". *Molecular Psychiatry*, **17**, 549–558 (2012).

[Tournier 2019] Tournier, J.-D., Smith, R., Raffelt, D., et al. "MRtrix3: A fast, flexible and open software framework for medical image processing and visualisation". *NeuroImage*, **202**, 116137 (2019).

[Turrigiano 2012] Turrigiano, G. "Homeostatic synaptic plasticity: local and global mechanisms for stabilizing neuronal function". *Cold Spring Harbor Perspectives in Biology*, **4**, a005736 (2012).

[Uğurbil 2003] Uğurbil, K., Toth, L., & Kim, D.-S. "How accurate is magnetic resonance imaging of brain function?". *Trends in Neurosciences*, **26**, 108–114 (2003).

[van Eijk 2021] van Eijk, L., Zhu, D., Couvy-Duchesne, B., et al. "Are Sex Differences in Human Brain Structure Associated With Sex Differences in Behavior?". *Psychological Science*, **32**, 1183–1197 (2021).

[Varier 2011] Varier, S. & Kaiser, M. "Neural Development Features: Spatio-Temporal Development of the Caenorhabditis elegans Neuronal Network". *PLoS Computational Biology*, **7**, e1001044 (2011).

[Veraart 2016] Veraart, J., Novikov, D. S., Christiaens, D., et al. "Denoising of diffusion MRI using random matrix theory". *NeuroImage*, **142**, 394–406 (2016).

[Vidaurre 2017] Vidaurre, D., Smith, S. M., & Woolrich, M. W. "Brain network dynamics are hierarchically organized in time". *Proceedings of the National Academy of Sciences*, **114**, 12827–12832 (2017).

[Wakana 2004] Wakana, S., Jiang, H., Nagae-Poetscher, L. M., van Zijl, P. C. M., & Mori, S. "Fiber tract-based atlas of human white matter anatomy". *Radiology*, **230**, 77–87 (2004).

[Welch 2011] Welch, D., Bansal, S., & Hunter, D. R. "Statistical inference to advance network models in epidemiology". *Epidemics*, **3**, 38–45 (2011).

[Woolrich 2009] Woolrich, M. W., Jbabdi, S., Patenaude, B., et al. "Bayesian analysis of neuroimaging data in FSL". *NeuroImage*, **45**, S173–186 (2009).

[Wu 2011] Wu, C. W., Chen, C.-L., Liu, P.-Y., et al. "Empirical evaluations of slice-timing, smoothing, and normalization effects in seed-based, resting-state functional magnetic resonance imaging analyses". *Brain Connectivity*, **1**, 401–410 (2011).

[Wu 2024] Wu, P., Lv, Z., Bi, Y., et al. "Network-based statistics reveals an enhanced subnetwork in prefrontal cortex in mild cognitive impairment: a functional near-infrared spectroscopy study". *Frontiers in Aging Neuroscience*, **16** (2024).

[Xia 2013] Xia, M., Wang, J., & He, Y. "BrainNet Viewer: A Network Visualization Tool for Human Brain Connectomics". *PLoS ONE*, **8**, e68910 (2013).

[Xie 2021] Xie, X., Cai, C., Damasceno, P. F., Nagarajan, S. S., & Raj, A. "Emergence of canonical functional networks from the structural connectome". *NeuroImage*, **237**, 118190 (2021).

[Xing 2023] Xing, L. & Chen, W. "Structural Characteristics and Evolutionary Drivers of Global Virtual Water Trade Networks: A Stochastic Actor-Oriented Model for 2000–2015". *International Journal of Environmental Research and Public Health*, **20**, 3234 (2023).

[Yang 2023] Yang, X., Wu, H., Song, Y., et al. "Functional MRI-specific alterations in frontoparietal network in mild cognitive impairment: an ALE meta-analysis". *Frontiers in Aging Neuroscience*, **15**, 1165908 (2023).

[Ye 2024] Ye, J., Tejavibulya, L., Dai, W., et al. "Variation in moment-to-moment brain state engagement changes across development and contributes to individual differences in executive function". *bioRxiv*, 2024.09.06.611627 (2024).

[Yeo 2011] Yeo, B. T. T., Krienen, F. M., Sepulcre, J., et al. "The organization of the human cerebral cortex estimated by intrinsic functional connectivity". *Journal of Neurophysiology*, **106**, 1125–1165 (2011).

[Zalesky 2014] Zalesky, A., Fornito, A., Cocchi, L., Gollo, L. L., & Breakspear, M. "Time-resolved resting-state brain networks". *Proceedings of the National Academy of Sciences of the United States of America*, **111**, 10341–10346 (2014).

[Zenke 2013] Zenke, F., Hennequin, G., & Gerstner, W. "Synaptic plasticity in neural networks needs homeostasis with a fast rate detector". *PLoS Computational Biology*, **9**, e1003330 (2013).

[Zhang 2019] Zhang, H. & Vorobeychik, Y. "Empirically Grounded Agent-Based Models of Innovation Diffusion: A Critical Review". *Artificial Intelligence Review*, **52** (2019).

[Zhang 2025] Zhang, S., Li, M., Chen, A., et al. "Sex differences and age-related changes of large-scale brain networks". *BMC Medical Imaging*, **25**, 271 (2025).

[Zhou 2010] Zhou, J., Greicius, M. D., Gennatas, E. D., et al. "Divergent network connectivity changes in behavioural variant frontotemporal dementia and Alzheimer's disease". *Brain: A Journal of Neurology*, **133**, 1352–1367 (2010).

[Zuo 2017] Zuo, X.-N., He, Y., Betzel, R. F., et al. "Human Connectomics across the Life Span". *Trends in Cognitive Sciences*, **21**, 32–45 (2017).

Appendix A

Extra Simulated Data Results

A.1 Factor Analysis

For the simulated data analysis, we created the ROC and precision-recall curves for the individual factors. We only included the F-score graphs for the individual factors in the original discussion of this topic for the selection of a threshold. The full ROC nd precision-recall curves are presented in Figure A.1.

A.2 Subnetwork Analysis

We also conducted the entire evaluation procedure on the subnetworks individually beginning with the long-term density convention for selecting values (Figure A.2. In some ways these values resemble those in the full network; however, they tend to have a longer tail on the negative side (the positive side for Factor Distance 2 ($D2$)). The sizes of the subnetworks are the biggest indicator of the factor range behavior with the largest subnetwork (DMN) most closely resembling the full network factor range behavior.

A set of subnetwork specific models were created based on these long-term densities. In addition, the subnetworks for the full network model sets in the second part of the simulated dataset were run through the hypothesis-building procedure to see if the subnetwork factors could be derived. Then evaluations of these subnetwork model sets contain both these kinds of subnetwork models. These can be evaluated to form the ROC and precision-recall curves for the individual subnetworks (Figure A.3).

The subnetwork precision-recall curves are shown in Figure A.3 with the performance somewhat related to the size of the network with the two smallest networks performing the worst. However, this is not the only influence on performance as the highest performing subnetwork is the visual subnetwork (VN).

The F-scores can be plotted for the subnetworks as well. This was done at $\beta = 0.5$ to reflect the higher

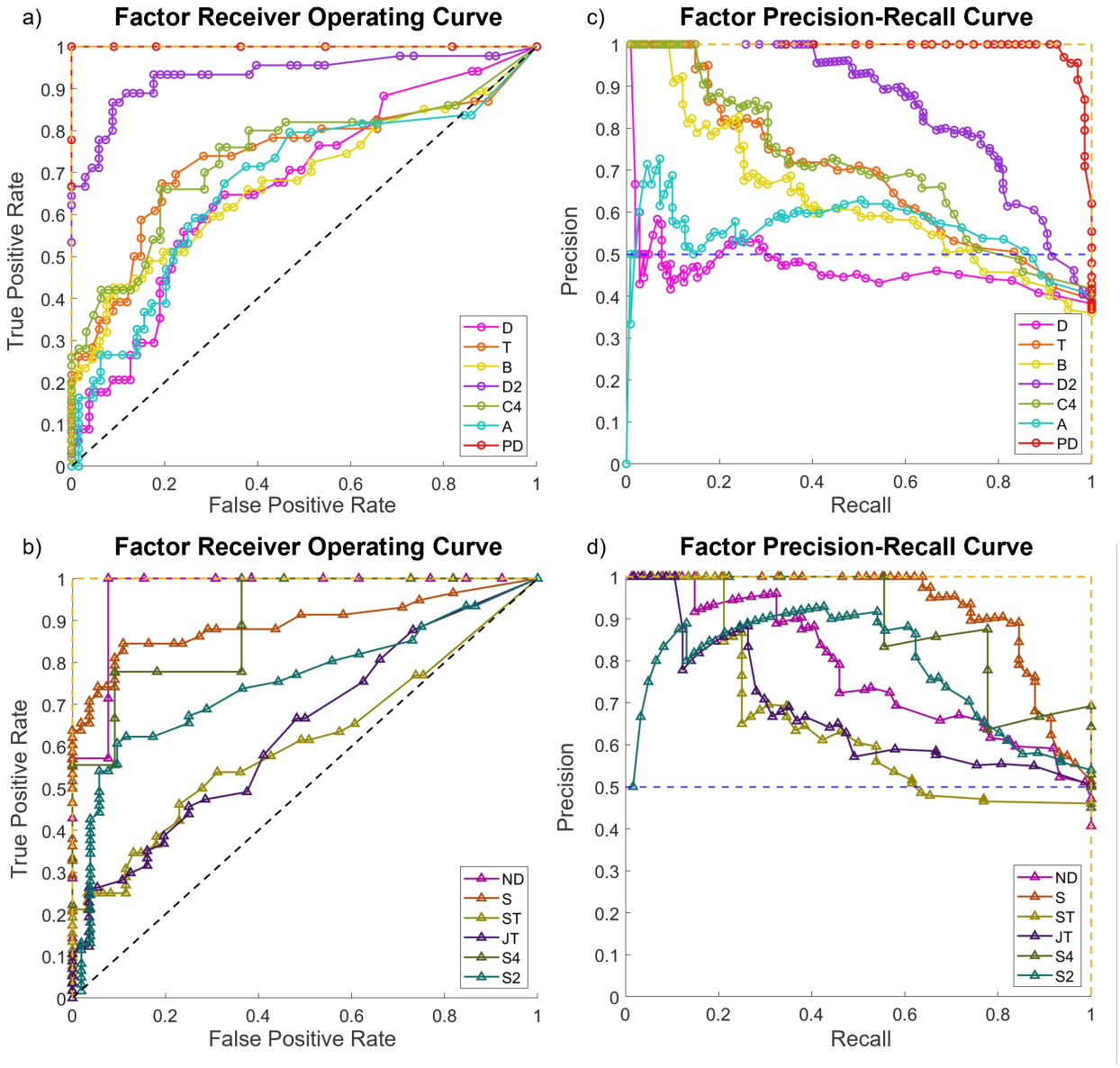

Figure A.1: **ROC and precision-recall curves for individual factors.** Figures (a) and (b) show the ROC curves for the individual factors with half the factors in (a) and half the factors in (b). The factors are split for visual clarity. Figures (c) and (d) show the precision-recall curves for the individual factors with half the factors in (c) and half the factors in (d).

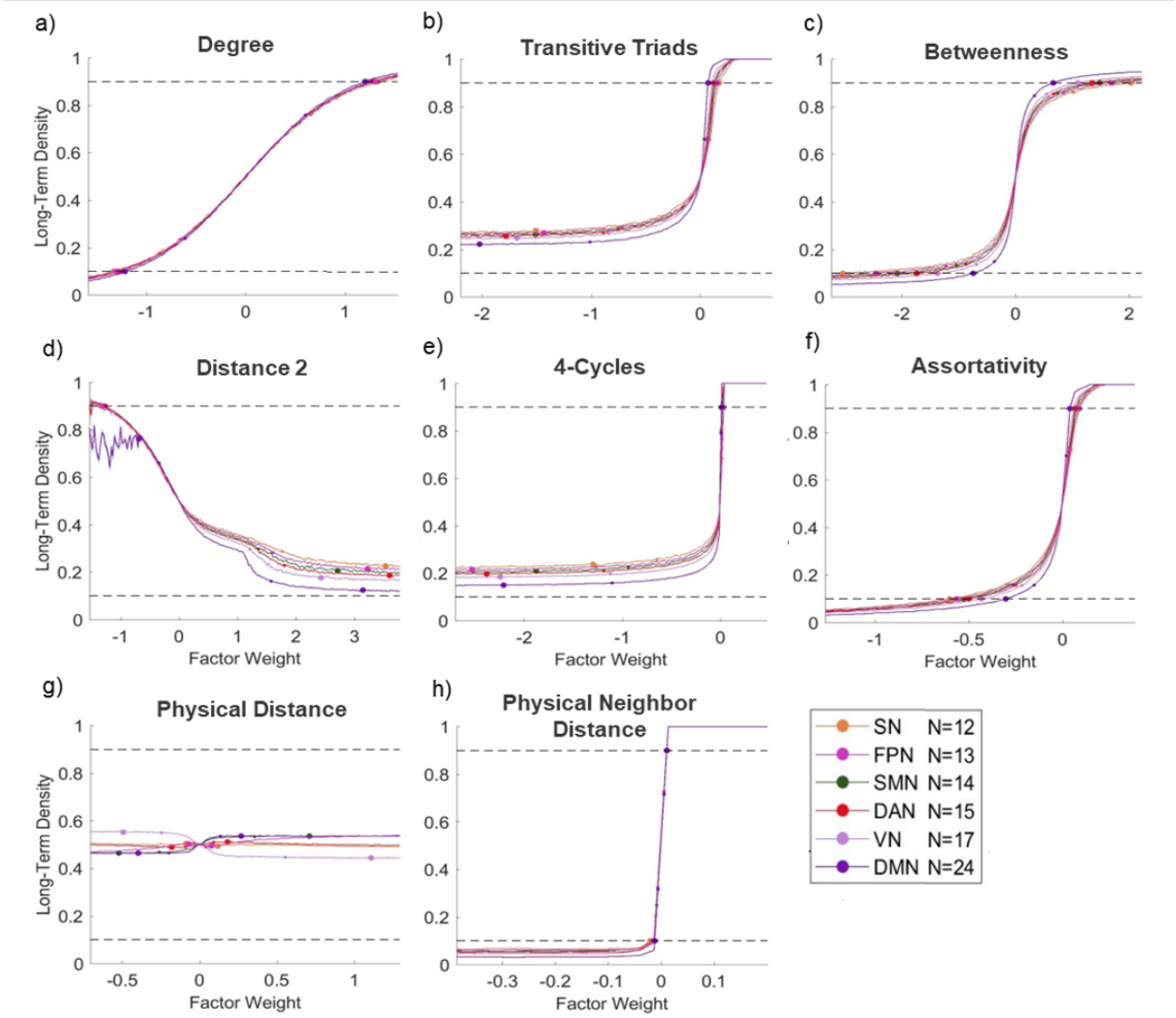

Figure A.2: **Long-term density for subnetwork factors.** These graphs show the density of the network after many iterations of models with a single factor at various factor weights for each of the subnetworks. This was used to determine reasonable simulation ranges for each factor. Each graph represents a different factor. The large marks show the selected large negative and large positive weights, while the smaller marks represent the small negative and small positive weights.

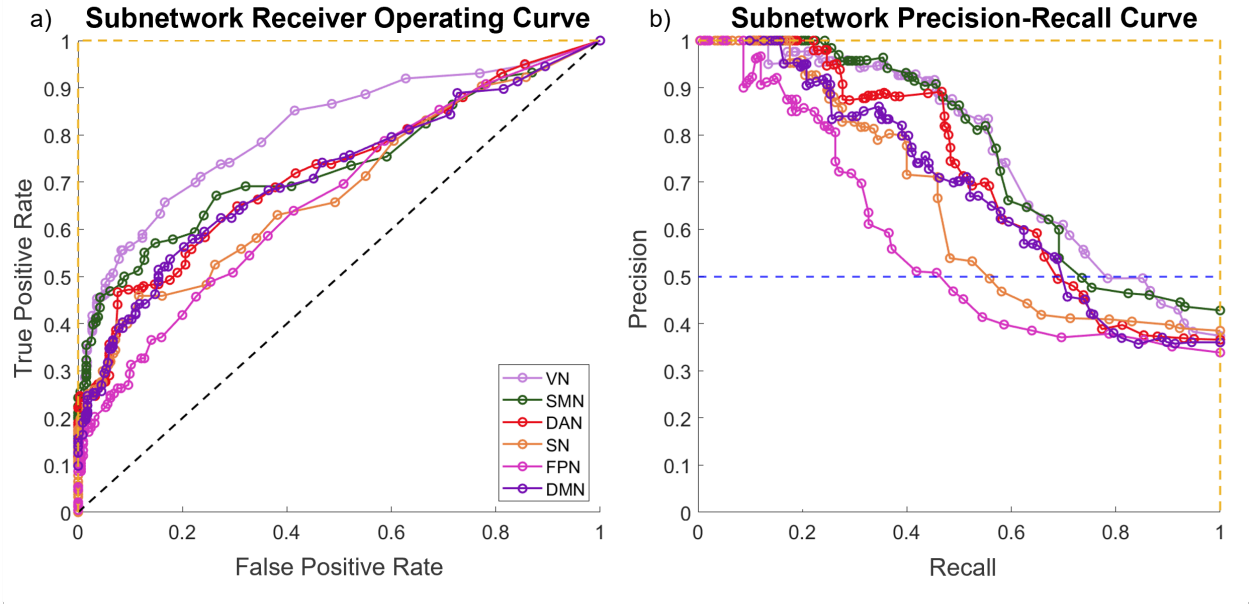

Figure A.3: **Subnetwork ROC and precision-recall curves.** Figure (a) is the ROC curve for the each subnetwork. Figure (b) is the precision-recall curve for each subnetwork. In both graphs, each point on the graph represents a different threshold value. The area under the curve describes the success of the procedure with 0.5 being no skill and 1 being perfect categorization.

priority of precision over recall.

These graphs show how the hypothesis-building procedure performs on the subnetworks specifically. They serve to reinforce the applicability of the procedure for use on the real dataset and suggest caution especially for those subnetworks with very few nodes.

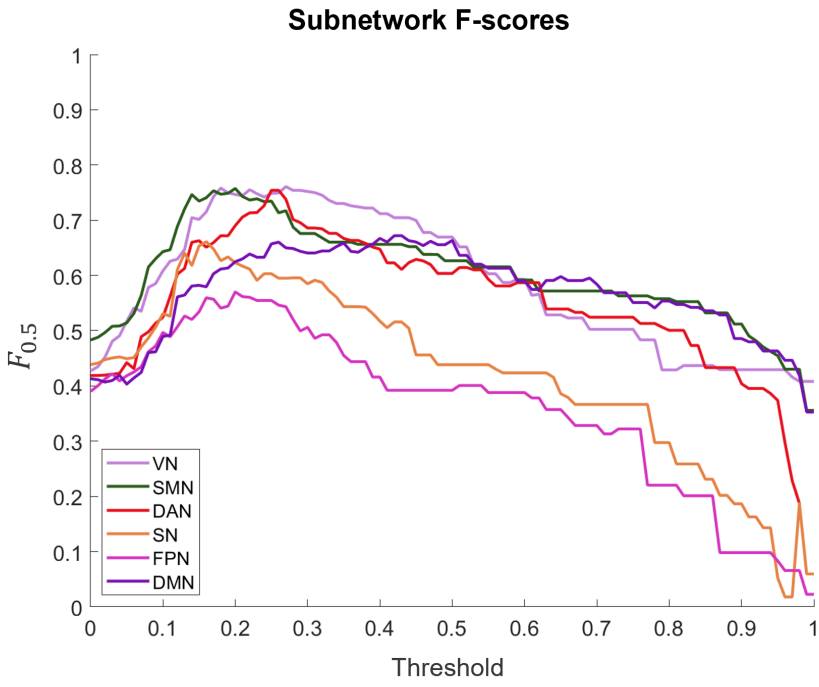

Figure A.4: **F-score for subnetwork results.** The F-score for the overall hypothesis-building procedure at various values of β, demonstrating the superior performance of precision over recall and the differences in overall performance at different thresholds.

Appendix B

Extra Aging Results

A few aging trends that were found in the data are included in this appendix. These trends are interesting and statistically significant, but difficult to parse with the rest of the results. Further investigation in these area could provide greater insight in the future. These aging trend appear exclusively in the subnetworks with the SMN showing a number of aging trends.

A number of factors found a significant quadratic fit with age when all participants were included where the weight of the factor is higher in early aging and late aging. These are found in Figure B.1. This trend may be an artifact of the smaller number of participants at the youngest and oldest age groups or evidence of some non-linear trend in aging. Non-linear trends are seen in aging research though they most often appear when examining a larger time frame (i.e. all of adulthood) [Chan 2014, Sexton 2014, Lebel 2012, Niu 2022].

A few other subnetwork aging trends are presented in Figure B.2. Trends for groups in the SMN were found for all three of the subnetwork factors. It is likely that the lack of differences found between diagnosed and control in the SMN were due to these aging trends. The trends in the SMN and the DMN do not follow the common pattern that we saw in many of the results measures of mild impairment trending towards the control in the later stages of aging.

It is unknown where these aging trends fit in the conception of our models, but they could be an interesting avenue for future research.

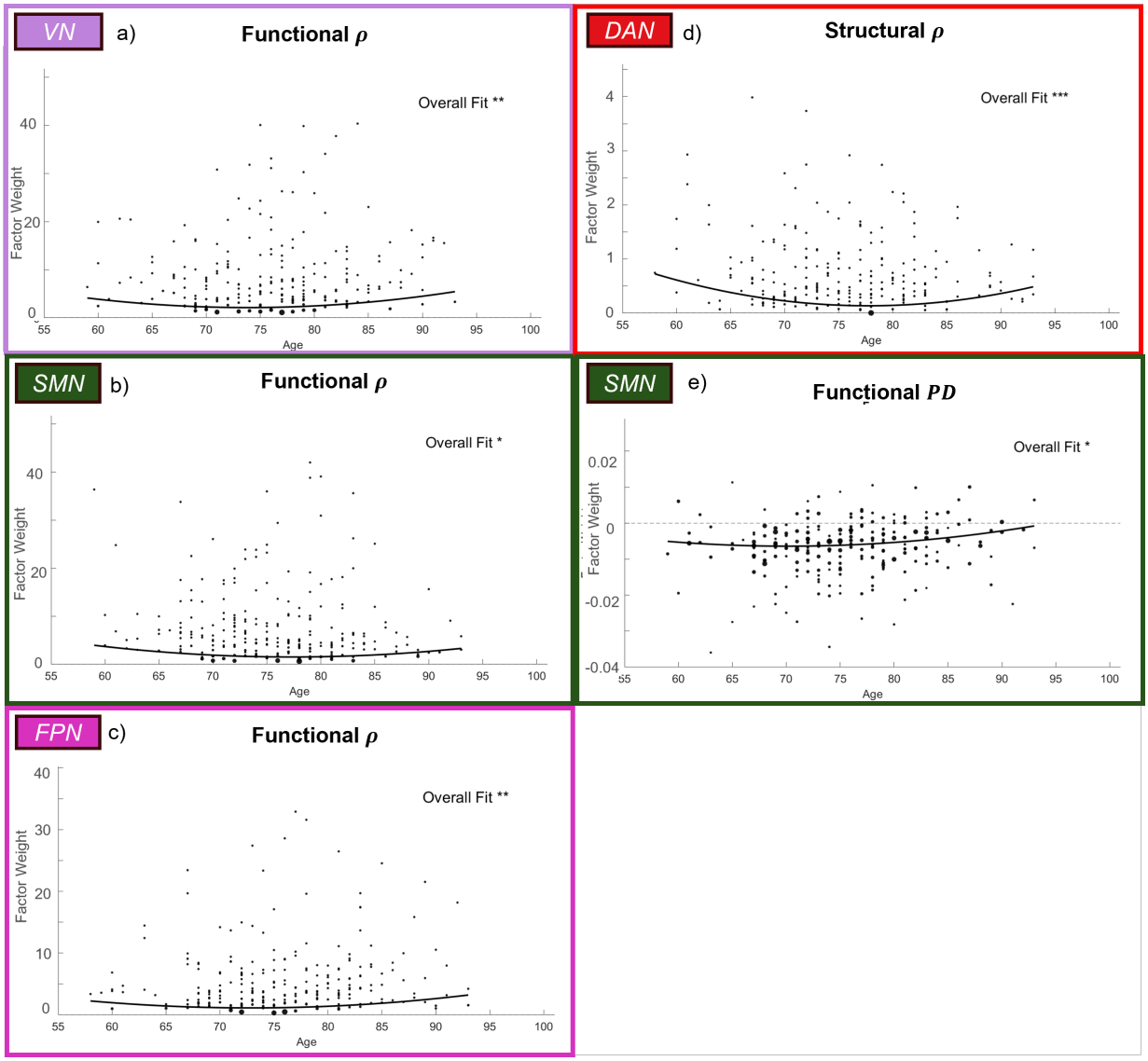

Figure B.1: **Quadratic fits in the subnetworks.** Quadratic fits were found for various subnetwork factors. Figure (a) shows the quadratic fit for rate (ρ) in the functional VN ($p = 0.002$). Figure (b) shows the quadratic fit for the rate (ρ) in the functional SMN ($p = 0.03$). Figure (c) shows the quadratic fit for the rate (ρ) in the functional FPN ($p = 0.008$). Figure (d) shows the quadratic fit for the rate (ρ) in the structural DAN ($p = 1 \times 10^{-}5$). Figure (e) shows the quadratic fit for the Factor Physical Distance (PD^S) in the structural SMN ($p = 0.01$).

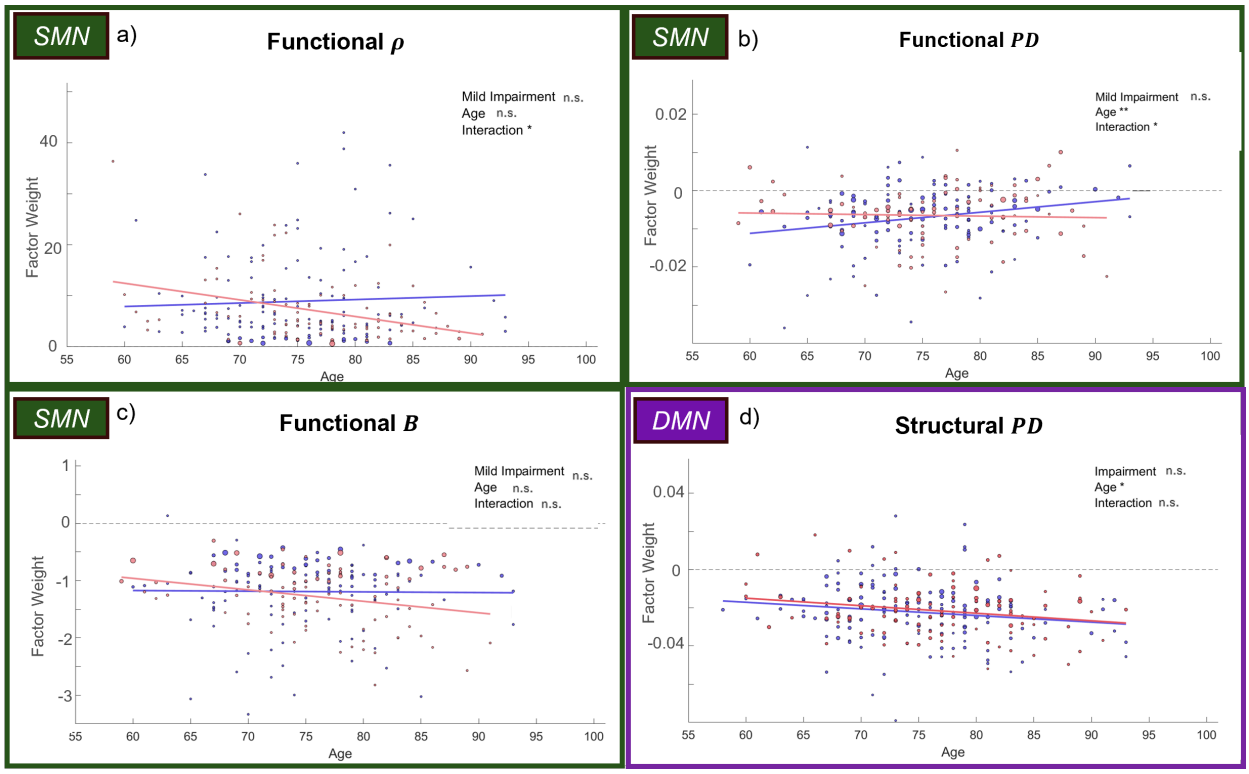

Figure B.2: **Other aging trend in the subnetworks.** This graph shows four aging trends that were found in the subnetworks for various subnetwork factors. Figure (a) shows an mild impairment-age interaction effect on ρ ($p = 0.03$) and a negative correlation with age in the mild impairment group ($p = 0.02$) in the SMN. Figure (b) shows an overall age effect ($p = 0.008$) and a mild impairment-age interaction effect ($p = 0.05$) for PD^S and a positive correlation in the control group with age ($p = 0.008$) in the SMN. Figure (c) shows a negative correlation of Factor Betweenness (B^S) with age in the mild impairment group ($p = 0.02$) in the SMN. Figure (d) shows an overall age effect ($p = 0.02$).